DUSTY RADIATIVE TRANSFER MODELING OF THE ULTRAVIOLET TO INFRARED SPECTRAL ENERGY DISTRIBUTIONS OF NEARBY GALAXIES

by

Ka-Hei Law

A dissertation submitted to The Johns Hopkins University in conformity with the requirements for the degree of Doctor of Philosophy.

Baltimore, Maryland

August, 2015

Abstract

In normal star forming galaxies without active galactic nuclei, stars and dust dominate the energy output in the ultraviolet (UV), optical and infrared (IR). Knowledge of stellar populations and dust is crucial to understanding the evolution of galaxies in the universe. The problems of dust and stars are tightly related because dust absorbs stellar radiation in the UV and optical, and re-radiates it in the IR. To study the properties of interstellar dust and stellar populations, we fit the global spectral energy distributions (SEDs) of nearby galaxies using radiative transfer models. Thanks to various space missions in the last few decades, the data required to construct the full UV to IR SEDs of nearby galaxies is available. To date, systematic studies on interstellar dust and stellar populations rely on simplified connections between the UV and IR such as energy conservation. Based on dust grain physics, radiative transfer models physically couple the UV and IR for consistent radiation fields and dust emission spectra, but is computationally challenging. With the use of supercomputer facilities, we compute a large grid of radiative transfer models spanning the physical range of dust and stellar parameters. Fitting SEDs with the grid is one step towards

ABSTRACT

a better understanding of interstellar dust and stellar populations. By fitting the SEDs of a group of nearby galaxies observed by the SINGS survey, we study the relative importance of young and old stellar populations in heating the dust, derive the ensemble properties of dust, estimate the total mass of dust, and test the robustness of the various star formation rate indicators in the literature.

Primary Reader: Colin A. Norman

Secondary Reader: Karl D. Gordon

Acknowledgments

I would like to express my deep gratitude to my advisors, Dr. Karl Gordon and Prof. Colin Norman, for their guidance, encouragement and continuous support over the years of my Ph.D. They are always available to help me with their immense knowledge on Astrophysics, and without them I could not imagine completing this ambitious project. I would also like to thank my thesis advisory committee members, Prof. David Neufeld and Prof. Timothy Heckman, for their constructive suggestions and assistance in keeping my progress on schedule. My thanks also extend to Heddy Arab, Caroline Bot, Martha Boyer, Jeremy Chastenet, Julia Roman-Duval, Brandon Lawton, Joshua Peek and Kirill Tchernyshyov for the countless insightful discussions on topics of the interstellar medium. I appreciate the work of the staff at the Department of Physics and Astronomy, especially Kelley Key for arranging my thesis defense and answering our many questions on the formal academic procedures. Lastly but very importantly, I thank my family—my parents and my brother in Hong Kong—for their wholehearted support and their patience while I pursue my dream far away from home for years.

Contents

List of Tables

List of Figures

Chapter 1

Introduction

1.1 Interstellar dust

1.1.1 Introduction

The primary constituents of the interstellar medium are gas (mainly hydrogen and helium) and dust (small solid particles). Interstellar dust was originally discovered by Trumpler (1930) from color excess of open star clusters, through the "reddening" property of dust. Dust blocks light, and it preferentially blocks shorter wavelength light. In visible light, blue light is more severely blocked by dust, and therefore stars appear redder than they should be when dust is present between the stars and us.

Dark clouds provide a dramatic example of this blocking effect, known to astronomers as dust extinction. Figure 1.1 shows the appearance of Barnard 68, a

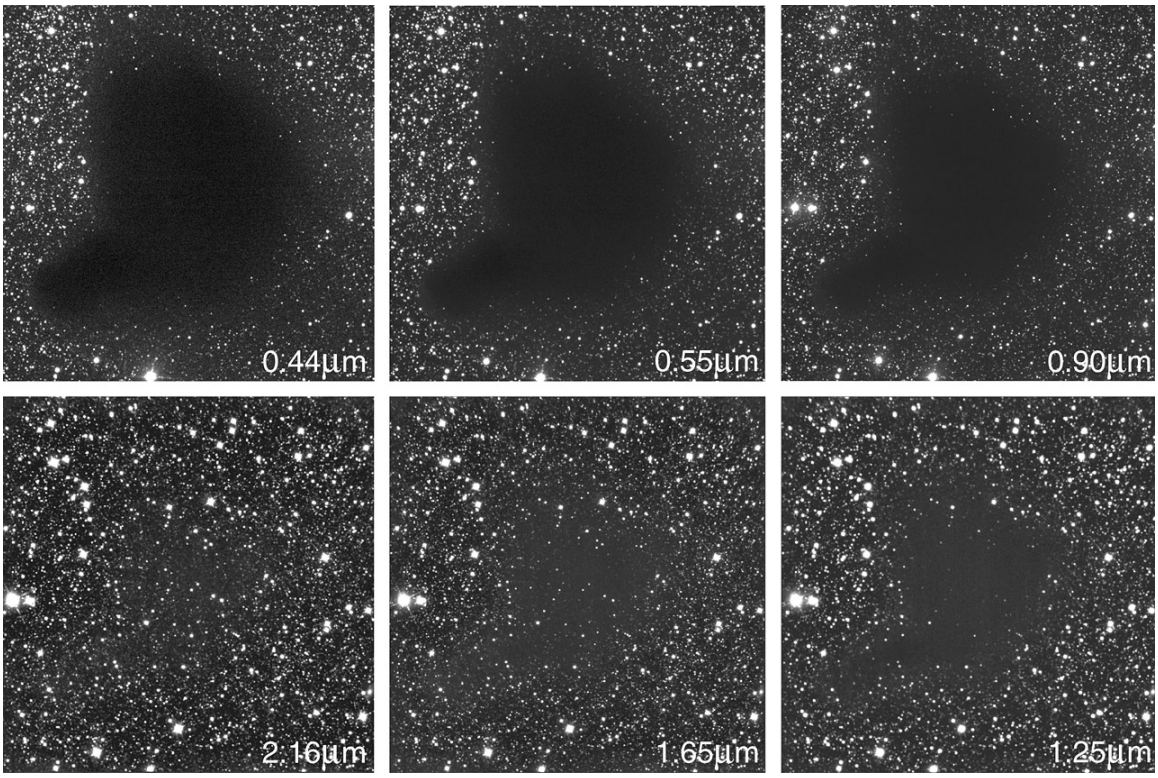

Figure 1.1: Dark cloud Barnard 68 at optical (0.44 and 0.55 μm) and near-IR (> 0.7 μm) wavelengths. Credit: European Southern Observatory.

nearby dark cloud at a distance of 500 light-years, at optical and near-IR wavelengths. Barnard 68 is a self-gravitating dense molecular cloud that is two times as massive as our Sun, and is on the verge of gravitational collapse to form new stars (Burkert & Alves, 2009). It is called a molecular cloud because the gas phase material is mainly molecular hydrogen (as opposed to atomic or ionized hydrogen). It is also called a dark cloud because its dust opacity is so high that it completely blocks the background stars in the optical. This is evident in the 0.44 μm (red) and 0.55 μm (green) images. However, in the near-IR, the light-blocking ability of dust decreases. At 2.16 μm, we can see most of the background stars through the cloud, almost

unaffected by dust.

Interstellar dust grains are small solid particles that are typically smaller than one micron in diameter. In the diffuse interstellar medium, they are typically at a temperature of 10 to 100 K, although they can reach higher temperatures near intense radiation sources. The importance of dust is threefold. Firstly, it participates in the physical processes of star formation and galaxy evolution. It is a formation site of molecular hydrogen and it shields molecular clouds from external radiation, facilitating the gravitational collapse of the gas from which stars form. Secondly, it significantly affects the appearance and energy balance of galaxies. Dust heavily absorbs light in the UV-optical and re-emit this absorbed energy in the IR. A significant amount of the total luminosity of galaxies come from IR dust emission. To accurately measure the properties of galaxies and other astronomical objects, one must correctly account for the effect of dust. Thirdly, dust provides a valuable tracer of the conditions of the environment. Dust mass correlates with the total mass of the interstellar medium, and the type of dust present provides clues to the radiation intensity and past star formation history.

Compared to our knowledge of stars, our knowledge of dust is relatively uncertain. Unlike stars, dust does not generate radiation on its own. Observations on dust rely on an external power source (typically stars), and the properties of dust and its power source may be entangled. Moreover, dust and stars are usually mixed in complex geometries, and the transfer of stellar photons through dust strongly affects

the measurements of both the dust and stellar populations. Correctly accounting for the radiative transfer effects requires the use of a dust radiative transfer model, which is computationally expensive due the strongly scattering nature of interstellar dust. With the help of supercomputers, this thesis improves the understanding of interstellar dust in nearby galaxies through radiative transfer modeling of stellar populations mixed with dust.

1.1.2 Optical depth and extinction efficiency

The strength of dust extinction is quantified by the "optical depth", which describes the combined effects of absorption and scattering to remove flux from a line of sight. Optical depth depends on wavelength, and despite its name, the term is used in other wavelengths (e.g., UV) as well. It is typical to quantify dust extinction with the optical depth at V band (a green optical light filter centered at 0.55 μm) because V band was established in one of the earliest used photometric systems in Astronomy.

At wavelength λ, the specific radiation intensity $I_{\lambda 0}$ exponentially decreases to I_λ after passing through a medium with optical depth τ_λ:

$$I_\lambda = I_{\lambda 0} \exp(-\tau_\lambda) \tag{1.1}$$

An optical depth of unity causes a reduction of radiation intensity by a factor of e. We describe a medium in which the optical depth is much greater (smaller) than unity as optically thick (thin).

It is also common to quantify the amount of extinction by the reduction of brightness in magnitudes. In astronomy, the magnitude scale is defined such that an increase in brightness by 100 times is a decrease of 5 magnitudes. Since both optical depth and magnitude are logarithmic quantities, the conversion between them requires only a multiplicative constant.

$$A_\lambda = -2.5 \log_{10}(I_\lambda / I_{\lambda 0}) \tag{1.2}$$

$$\tau_\lambda = -\log_e(I_\lambda / I_{\lambda 0}) \tag{1.3}$$

$$A_\lambda = \frac{2.5}{\log_e(10)} \tau_\lambda \approx 1.086 \tau_\lambda \tag{1.4}$$

Physically, optical depth is related to:

$$\tau(\lambda) = n_{\text{dust}} C_{\text{ext}}(a, \lambda) l \tag{1.5}$$

where n_{dust} is the number density of dust particles, C_{ext} is the extinction cross section (a measure of interaction probability), and l is the path length. Deviations from the classical cross section of πa^2, where a is the radius of the particle, can be expressed as the extinction efficiency Q_{ext}:

$$Q_{\text{ext}}(a, \lambda) = C_{\text{ext}}(a, \lambda) / (\pi a^2) \tag{1.6}$$

1.1.3 Absorption and Scattering

The physical processes that cause dust extinction are absorption and scattering. Mathematically, extinction cross section C_{ext} is a sum of absorption and scattering

cross sections. The same applies to extinction efficiency.

$$C_{\rm ext} = C_{\rm abs} + C_{\rm sca} \tag{1.7}$$

$$Q_{\rm ext} = Q_{\rm abs} + Q_{\rm sca} \tag{1.8}$$

In absorption, incoming radiation is absorbed by dust particles, resulting in an increase of the internal energy (and therefore temperature) of the dust particles and a reduction in the outgoing radiation intensity. In scattering, incoming radiation interacts with dust particles and changes its direction of propagation such that the radiation intensity is decreased in the original line of sight but increased towards a different direction.

The absorption and scattering efficiencies ($Q_{\rm abs}$ and $Q_{\rm sca}$) can be measured in the laboratory or calculated from Mie theory for spherical grains. Q depends on grain composition, grain size, wavelength, and to a lesser extent, grain temperature. For idealized spherical grains, in the limit of $\lambda \ll a$, both $Q_{\rm abs}$ and $Q_{\rm sca}$ are approximately unity, so the total extinction cross section is twice the physical cross section; In the limit of $\lambda \gg a$, $Q_{\rm abs} \propto \lambda^{-2}$ and $Q_{\rm sca} \propto \lambda^{-4}$, so extinction rapidly decreases towards longer wavelengths (often negligible in the IR) and is dominated by the absorption process. Scattering in the long wavelength limit is known as Rayleigh scattering, and a common example is the blue sky caused by the scattering of sunlight by atmospheric particles.

The scattering angle is defined as the difference between the incoming and outgoing directions of a scattered photon. The scattering phase function characterizes the

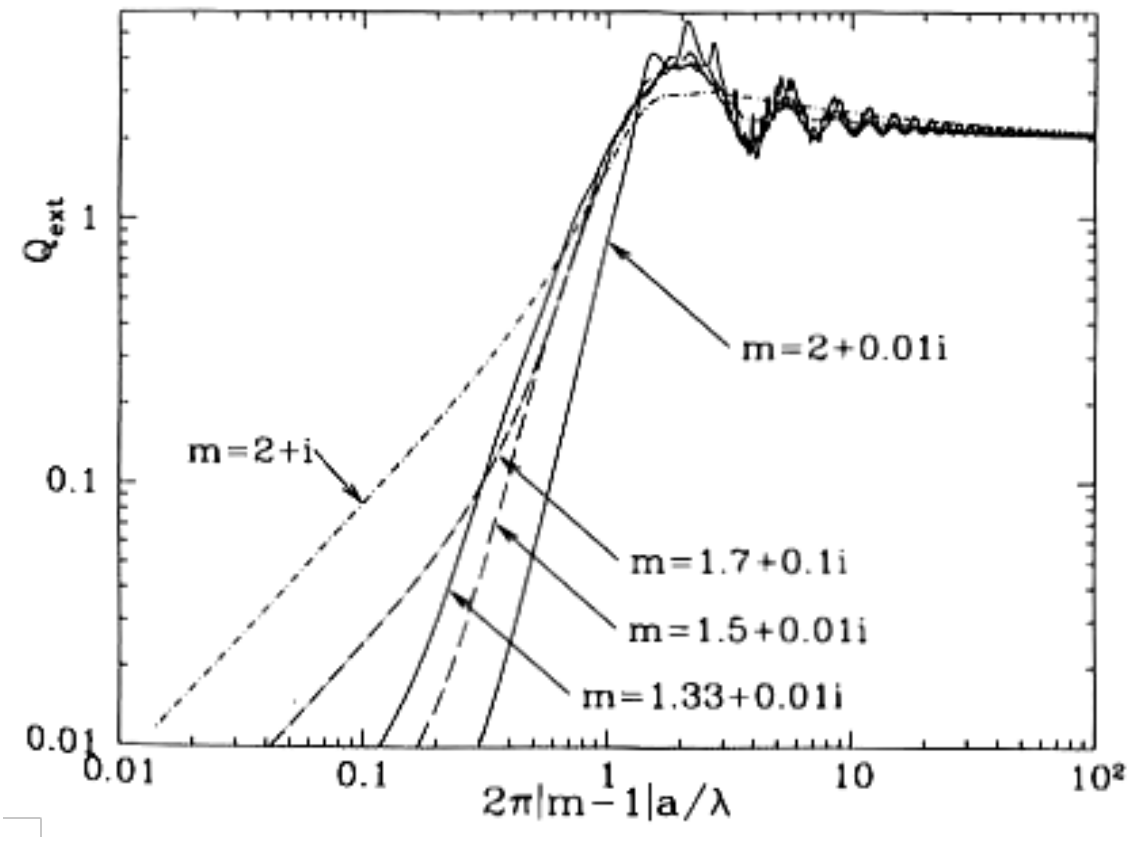

Figure 1.2: Extinction efficiency $Q_{\rm ext}$ for theoretical spheres with refractive indices, m. From Draine (2011).

angular distribution of the scattered light, and the Henyey-Greenstein phase function (Henyey & Greenstein, 1941) is one commonly used analytic form.

$$\Phi(\theta) = \frac{1}{4\pi} \frac{1-g^2}{(1+g^2-2g\cos\theta)^{3/2}} \tag{1.9}$$

$$g = \langle \cos\theta \rangle \tag{1.10}$$

This function is parametrized by the first moment of the phase function, g, which depends on grain properties and wavelength, and is typically close to zero in the IR (isotropic scattering) and positive in the UV (forward-biased scattering).

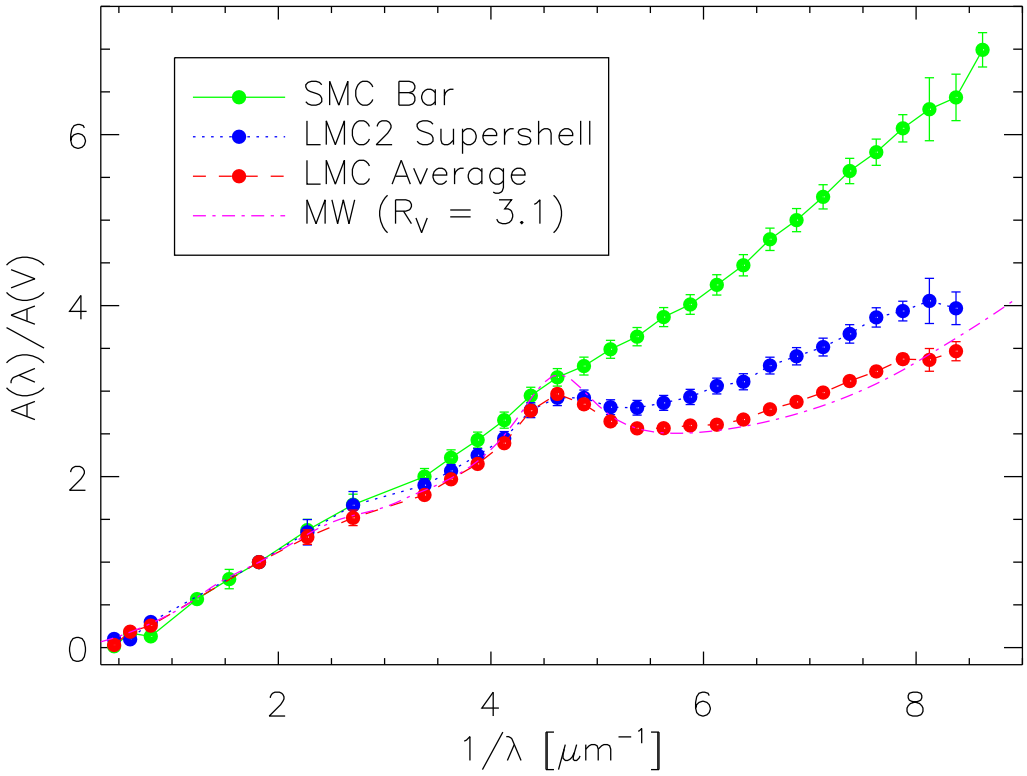

Figure 1.3: Average extinction curves for dust found in the Milky Way and the Magellanic Clouds. From Gordon et al. (2003).

1.1.4 Extinction curve

The wavelength dependence of extinction can be conveniently summarized by an extinction curve. The standard way to measure the extinction curve is the "pair method". Stellar theories allow us to predict the intrinsic, unreddened stellar spectra from its spectral type. By comparing the UV-optical spectra of two stars of the same spectral type, one reddened and one unreddened, we can obtain the amount of extinction at each wavelength of the spectra, resulting in an extinction curve. Cardelli et al. (1989) found that variations of extinction curves in the Milky Way can be

characterized by a single parameter $R_{\rm V} = A(V)/E(B-V)$, which is a ratio between the extinction and reddening (also referred to as the total to selective extinction). The diffuse ISM in the Milky Way has an average $R_{\rm V} \approx 3.1$, while the value is higher in dense clouds.

Figure 1.3 shows the average extinction curves of dust found in the Milky Way and the Magellanic Clouds. For now, we focus on the Milky Way average ISM curve, which uses the Cardelli et al. (1989) parametrization with $R_V = 3.1$. The main feature of the curve is the "2175 Å" bump, which gives enhanced extinction around $1/\lambda \approx 4.5\ \mu\mathrm{m}^{-1}$. The curve includes information about dust composition and size distribution, which we will explore in § 1.1.7 and § 1.1.8.

1.1.5 Equilibrium emission

The energy absorbed by dust has to go somewhere. Given that the temperature of dust grains in the interstellar medium is typically tens of Kelvins, dust grains emit primarily in the IR. According to statistical mechanics, ideal black bodies, or objects that completely absorb all incoming radiation regardless of wavelength, emit radiation with a wavelength distribution described by the Planck function. The changing cross section of dust grains depending on wavelength causes them to emit as a "modified black body" which has a grayer wavelength dependence. The modification is known as emissivity.

One important feature of black body radiation is that the total power radiated

is proportional to the fourth power of the equilibrium temperature of the emitting object. This is known as the Stefan-Boltzmann law. One implication is that as the temperature of dust grains increases, the total luminosity of dust emission increases very rapidly. On the other hand, the total absorbed energy of a dust grain uniquely determines its temperature, if and only if the grain is in equilibrium with the radiation field.

Wien's law states that the peak of the radiation intensity is related to the temperature in a simple relation:

$$\lambda_{\max} T_{\rm dust} \sim 3000 \mu{\rm m\,K} \tag{1.11}$$

As such, the peak of equilibrium dust emission at 30 K is approximately located at 100 μm.

Given the low density of the interstellar medium, dust grains of different compositions and sizes may not have the same temperature. The total dust emission is the sum of the individual modified black body functions of each grain.

1.1.6 Stochastic emission

The temperature of small grains is greatly affected by the absorption of a single photon. Figure 1.4 shows the time dependent temperature profile of four carbonaceous grains of different sizes in the local interstellar radiation field using the grain models of Draine & Li (2001). Typically, for grains with radius $a \ll 100$ Å, the temperature

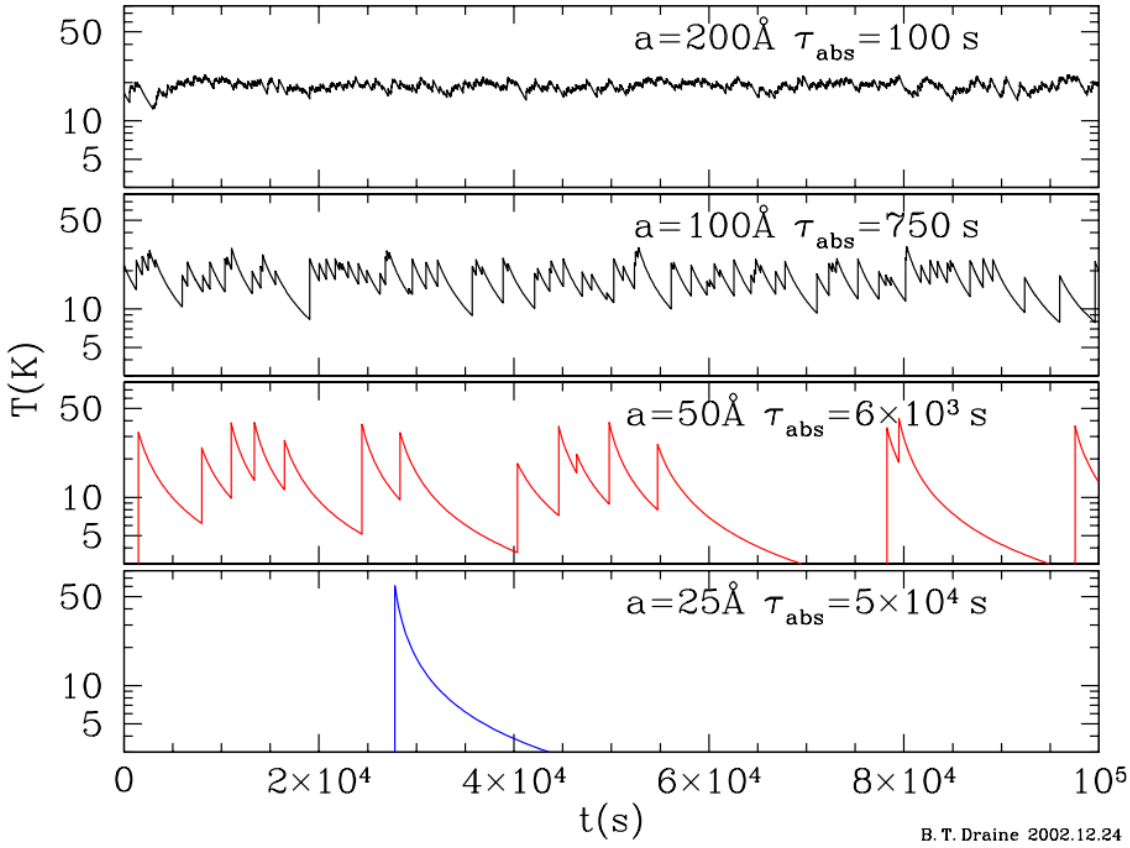

Figure 1.4: Modeled time dependent temperature profile of four carbonaceous grains of different sizes in the local interstellar radiation field. From Draine (2003).

fluctuates significantly between photon absorption events. Given the highly non-linear nature of the temperature dependence of dust emission, the assumption of equilibrium emission with a time averaged temperature is not a good approximation in this regime.

One way to calculate dust emission in this stochastic heating regime is to make use of the temperature profile (or probability distribution of temperature) $P(T)$ of the dust grains. The radiation field, the absorption cross section and the heat capacity of the dust grains jointly determines the heating rates for grains at different

temperature. The cooling rates are determined from the emissivity of dust grains. By solving the transition matrix (potentially with approximation techniques) in which the elements are the heating and cooling rates, we obtain $P(T)$. Integrating $P(T)$ with the emission at each temperature gives us the total dust emission due to stochastic heating. In the limit of large grains, $P(T)$ becomes very narrowly peaked and the result asymptotically reaches equilibrium emission.

1.1.7 Chemical composition

Candidates for the chemical composition of dust grains have been identified from (1) the spectroscopic features of dust extinction and emission and (2) elemental abundance depletion, which provides constraints on what elements could be in dust by comparing the amount of heavy elements produced by stars and the amount observed in the interstellar gas.

The interstellar medium is rich in C, O, Mg, Si, and Fe atoms. The 9.7 and 18 μm broad absorption features have been identified as the Si-O stretching and O-Si-O bending modes of silicate grains (McCarthy et al., 1980a). The lack of detailed features in the 9.7 μm feature in many sightlines, however, suggests these silicate grains are amorphous instead of crystalline. The 2175 Å bump in the extinction curve is likely to be caused by transitions of the π electrons in hexagonal carbon sheets. Such material can be crystalline graphite grains, amorphous carbon grains, or polycyclic aromatic hydrocarbons (PAH) grains/molecules. The variations in the width of the

2175 Å bump combined with the lack of variations in the central wavelength favors PAH grains as the carrier of this absorption feature. Duley & Seahra (1998) attributed the 3.4 μm extinction feature to hydrogenated amorphous carbon (HAC) grains. In the mid-IR, a large number of emission features has been identified as PAH features caused by C-C and C-H stretching/bending modes (Leger & Puget, 1984).

1.1.8 Size distribution

In order to fit the 0.11 to 1 μm extinction curves in the Milky Way, Mathis et al. (1977) found that a distribution of dust grain sizes is required. They used a power law distribution in the form of $n(a) \propto a^{-3.5}$ within the range of 5 nm to 1 μm for graphite grains and 25 to 250 nm for other grain materials.

In general, a steeper extinction curve indicates the presence of more small grains. Recall that according to Mie theory, the extinction cross section is asymptotically constant if the grain size is larger than the wavelength of the photon. Roughly speaking, the slope of the extinction curve at a given wavelength comes from grains that are smaller than that wavelength.

1.2 Variation of dust properties in other galaxies

1.2.1 The Magellanic Clouds

The Large Magellanic Cloud (LMC) and the Small Magellanic Cloud (SMC) are irregular dwarf galaxies orbiting our Milky Way galaxy. As they are nearby, it is possible to resolve individual stars, allowing us to study dust extinction in the Magellanic Clouds in great detail. The average extinction curves in these two galaxies are shown in Fig. 1.3.

The average extinction curve in LMC is similar to the one in the Milky Way. However, in and near the LMC 2 supergiant shell region[1], the extinction curves show a weakened 2175 Å bump compared to Milky Way extinction curves (Misselt et al., 1999). This suggests that dust grain properties may be affected by the environment. In the SMC Bar region, extinction curves appear to lack the 2175 Å feature and have the steepest far-UV rise (Gordon & Clayton, 1998). These extinction curve do not fit the shape of the Cardelli et al. (1989) relation designed for Milky Way sightlines (Gordon et al., 2003), but Weingartner & Draine (2001) successfully reproduced them by adjusting the composition and size distribution of dust grains. In particular, they used models without carbonaceous grains smaller than radius $a < 0.02$ μm to

[1]The LMC 2 supergiant shell region is on the southeast side of the extremely luminous H II region 30 Dor, in which the intense UV radiation from young, massive stars ionize the hydrogen atoms in the interstellar medium

reproduce the SMC Bar extinction curves.

1.2.2 Starburst galaxies

Starburst galaxies are galaxies undergoing intense star forming activities. Precise definition of such a galaxy varies. Two definitions used are: (1) the current star formation rate (SFR) greatly exceeds the past-averaged SFR, or (2) the current SFR exceeds the ratio between the available gas and a characteristic timescale, such as the age of the galaxy. As such, the starbursting phase of a galaxy cannot be sustained. Starbursts are typically triggered by galaxy mergers or gravitational disturbance from close encounters of galaxies.

The high luminosity of starburst galaxies make them easy to detect spectroscopically. The fact that the luminosity is dominated by young stars also makes it easier to interpret results. From the International Ultraviolet Explorer UV and optical spectra of 39 starburst galaxies with different amounts of reddening, Calzetti et al. (1994) derived an average attenuation law for starburst galaxies. The curve is found to be flatter than the Milky Way extinction law and lacks the 2175 Å dust feature. Gordon et al. (1997) found that their radiative transfer models can reproduce the measured starburst attenuation law if they adopt SMC dust properties.

1.2.3 High-redshift galaxies

The expanding universe lengthens the wavelengths of the traveling electromagnetic waves from distant galaxies to us. This effect, termed "redshift", is noticeable beyond a distance of a few million light-years[2]. High-redshift galaxies are difficult to resolve. However, since light takes time to travel such large distances, these galaxies allow us to observe the past universe. Vijh et al. (2003) found that the observed colors of high-redshift galaxies selected using the Lyman-break technique are incompatible with Milky Way type dust and suggested that they are SMC-like. However, Noll et al. (2007) found that one-third of their sample of high-redshift star-forming galaxies has a moderate UV extinction bump, and the bump strength is anti-correlated with the galaxy luminosity. In addition, Elíasdóttir et al. (2009) detected strong bumps in the optical afterglow spectrum of a gamma-ray burst galaxy. These show that dust properties in high-redshift galaxies vary, which may cause severe uncertainties in the inferred galaxy and stellar properties if a single prescription of dust properties is used.

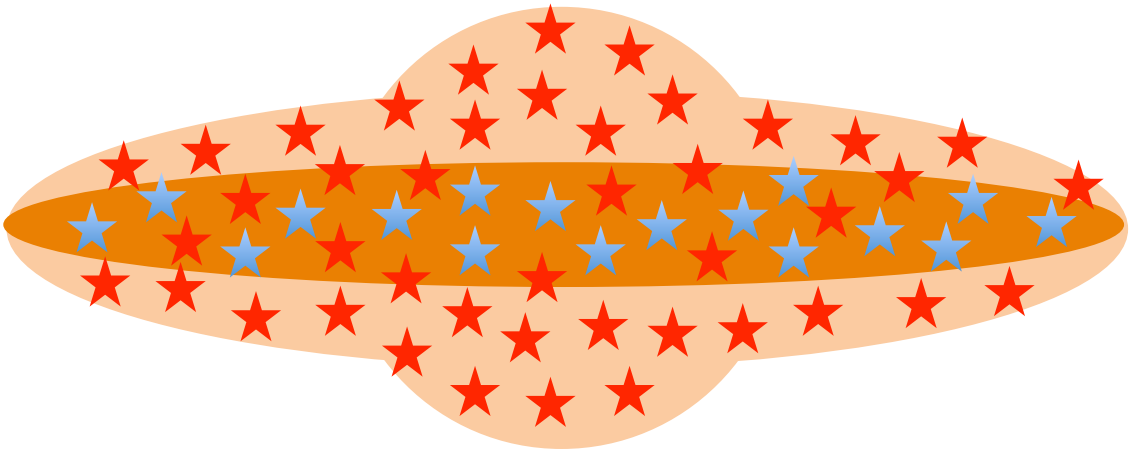

Figure 1.5: Schematic diagram of the location of old stars (red), young stars (blue) and the interstellar medium (shaded region) in an idealized spiral galaxy. From De Looze et al. (2014).

1.3 Modeling dusty galaxy spectral energy distributions

1.3.1 Galaxies as a mixture of stars and dust

Normal star forming galaxies have young stellar populations and old stellar populations that both contribute significantly to the global spectral energy distribution (§ 1.3.3). Stars are formed from the gravitation collapse of molecular clouds, so in their early life they are expected to be heavily embedded in dust. As they age, the stellar wind pushes away the interstellar medium of gas and dust and the optical depth of the stars gradually decreases. In spiral galaxies, the bulge is dominated by old stellar populations with little interstellar medium, while in the disc we can find

[2]This compares to the 91 billion light-years size of the observable universe

young stellar populations with abundant gas and dust. The relative position of dust and stars in a galaxy is therefore complex, and correct modeling of dust in galaxy must take into account (at least approximately) these geometric effects.

Furthermore, the interstellar medium is clumpy instead of homogeneous. Witt & Gordon (1996) found that a minimum of two phases of non-zero density is necessary to model the interstellar dust medium in the Milky Way. The primary effect of clumpiness on dust attenuation is that for the same amount of dust grains, it reduces the effective attenuation and flattens the attenuation curve.

1.3.2 Stellar population model

In the absence of interstellar dust, the spectrum of a galaxy can be modeled as a sum of the spectra of its constituent stars. Stars are formed from the collapse of molecular clouds when gas pressure is no longer sufficient to support the gravitational force. In each star formation event, a distribution of stars with different masses form. In general, the number of high mass stars (which are luminous, hot, UV-bright and short lived) is significantly lower than the number of low mass stars (which are cooler and emits the bulk of radiation in longer wavelengths). The initial mass function (IMF) describes the distribution of stellar masses of newly formed stars. Salpeter (1955) was the first to determine the IMF empirically, and the Salpeter IMF is a power law function with a negative exponent of -2.35.

Most stars are essentially nuclear furnaces that burn hydrogen into helium through

thermonuclear fusion. The theory of stellar physics is well developed. Given the initial mass and the heavy element abundance of a star, we can predict the evolution and the spectrum of the star to high accuracy for most phases of the star. Modeling of stellar evolution results in "evolutionary tracks" that describe the trajectory of stars in terms of parameters such as luminosity and surface temperature as the stars evolve. Given an IMF and stellar evolutionary tracks, stellar population synthesis models integrate over stars of different masses at the same age to produce the spectra of a single stellar population. Given the star formation history of a galaxy, one can then integrate these spectra over stellar age to obtain the total spectrum of the galaxy.

1.3.3 Spectral energy distribution

The spectral energy distribution (SED) describes how the radiation from a body is distributed across the electromagnetic spectrum. For galaxy fitting, the SED used typically extends from UV to IR. Due to the wide range of wavelengths, a single instrument cannot measure the entire UV to IR SED. For the most complete information on the UV to IR SED, it is common to combine individual observations from UV, optical, near-IR, mid-IR and far-IR (and sometimes sub-mm) instruments into a single SED. While the atmosphere is transparent in the optical and part of the near-IR wavelengths, it is opaque in the UV and most of the IR. Observations at other wavelengths require space telescopes (e.g., the Galaxy Evolution Explorer) or airborne observatories (e.g., the Stratospheric Observatory for Infrared Astronomy).

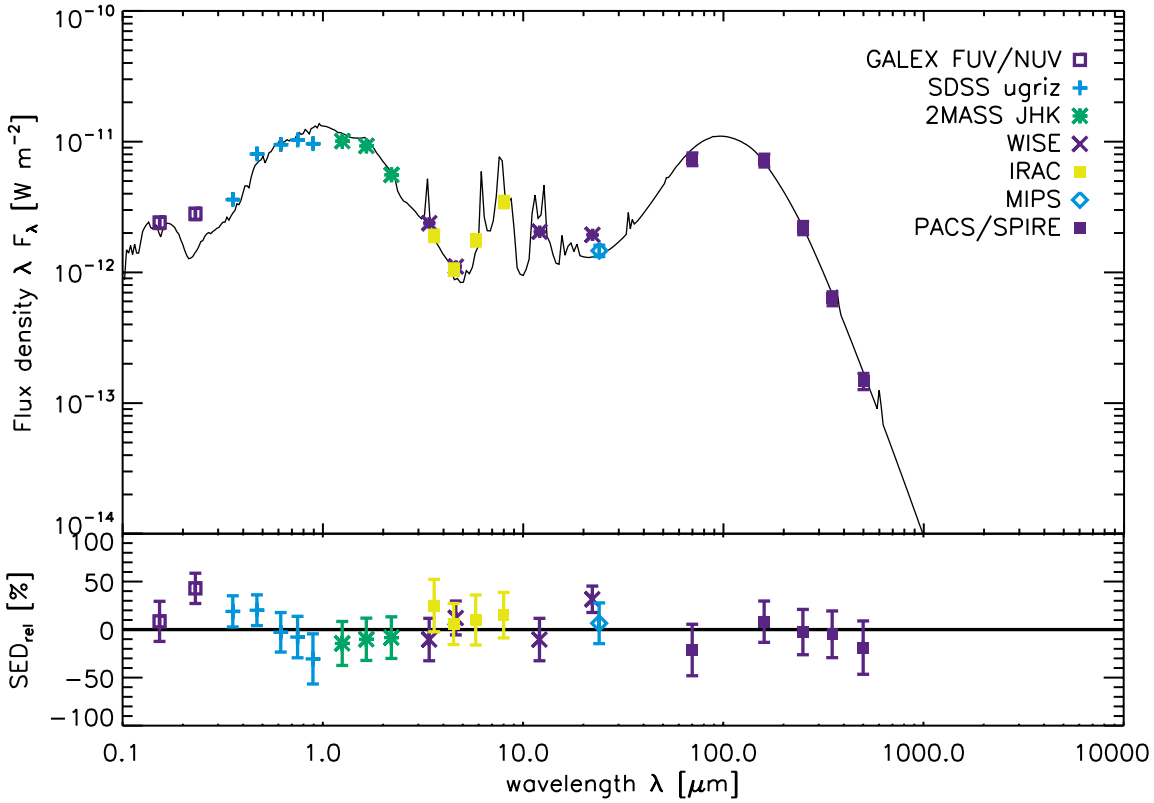

Figure 1.6: UV to IR SED fitting of spiral galaxy M51. In the upper panel, each symbol corresponds to a measurement with a broadband filter (plotted at its central or effective wavelength), and the line is the best fit model. The lower panel shows the residuals of the fit. From De Looze et al. (2014).

Care must be taken in data processing to make sure the apertures used at different wavelengths are the same, and the removal of foreground extinction or emission is consistent.

The SED of a normal star forming galaxy consists of a stellar peak and a dust emission peak. In the near-IR, the luminosity primarily comes from stellar radiation and is least affected by dust. In the UV and optical, stellar photons are attenuated by dust, which means that part of them may be absorbed by dust and removed from the sightline, part of them may be scattered by dust and travel towards a different

direction, and part of them may be scattered by dust from a different direction towards us. The far-IR is dominated by dust emission powered by photons absorbed in the UV-optical. In galaxies hosting an active galactic nucleus (AGN, e.g., a supermassive blackhole), the SED may include emissions from dust heated by the AGN.

Simultaneously fitting all the bands from UV to IR based on a physical model (instead of an empirical model often with separate UV-optical and IR templates) is a challenging task. While challenging, this task is within our capabilities and Figure 1.6 shows an example of the fitting of the global SED of a spiral galaxy using dust radiative transfer techniques.

1.3.4 Star formation rate indicators

Star formation rate (SFR) indicators are simple formulas linking the luminosity (over a limited wavelength range) of a galaxy or a stellar population to its SFR. Since the only stars that are bright in UV are short lived, the far-UV luminosity primarily comes from newly formed stars. In the absence of dust, the far-UV luminosity is a good tracer of star forming activity. The conversion factor between far-UV luminosity and SFR depends on the assumed IMF. Since only these UV-bright stars can ionize the hydrogen atoms in the surrounding interstellar gas, hydrogen recombination emission lines are also used as SFR tracers. The Hα emission line, commonly used because of its brightness and convenient wavelength in the optical range (656 nm, red), results from the electronic transition from the $n = 3$ to the $n = 2$ state of a hydrogen atom.

Estimation of SFR with far-UV or Hα luminosity suffers from systematic error due to dust extinction. In the UV-optical, the presence of dust significantly reduces the observed luminosity. The problem is especially severe because young stars are usually more embedded in dust. An unbiased SFR indicator should therefore compensate for the newly formed stars obscured by dust. Since dust re-emits the energy absorbed in the UV-optical in the IR, a combination of properly weighted UV-optical and IR luminosity could in theory provide a robust estimation of SFR. However, the use of IR luminosity poses a few challenges because not all of the IR luminosity comes from dust heated by young stars. Dust emission powered by absorption of optical photons from old stars does not reflect star forming activities. In low-dust environments, the stellar continuum of old stars may also contribution significantly in the near- to mid-IR.

1.3.5 The radiative transfer equation

The transport of radiation through a dusty medium can be described by the radiative transfer equation, which relates the change in the specific intensity across space with radiation source and sink terms. The radiative transfer equation describes how the radiation field varies as a function of position vector $\boldsymbol{x}$, direction vector $\boldsymbol{n}$, and wavelength λ. $\boldsymbol{x}$ indicates the location in space and $\boldsymbol{n}$ is a unit vector in the direction of the radiation. In vacuum, the frequency ν of electromagnetic radiation is completely determined by the wavelength λ with the relation $c = \nu\lambda$, where c is the

speed of light, so it is also possible to write the radiative transfer equation in terms of ν instead of λ.

The basic radiative transfer equation, with absorption (a sink term) and emission (a source term), is:

$$\boldsymbol{n} \cdot \nabla I(\boldsymbol{x}, \boldsymbol{n}, \lambda) = -\kappa_{\rm ext}(\boldsymbol{x}, \lambda)\rho(\boldsymbol{x})I(\boldsymbol{x}, \boldsymbol{n}, \lambda) + j(\boldsymbol{x}, \boldsymbol{n}, \lambda) \tag{1.12}$$

where the mass extinction coefficient $\kappa_{\rm ext}$ is the extinction cross section $C_{\rm ext}$ (§ 1.1.3) per unit mass, and ρ is the mass density of the opacity medium.

The differential equation has analytical solutions in the simplest cases (e.g., j independent of I). However, it becomes an integral-differential equation once we include scattering:

$$\begin{aligned} \boldsymbol{n} \cdot \nabla I(\boldsymbol{x}, \boldsymbol{n}, \lambda) = &- \kappa_{\rm ext}(\boldsymbol{x}, \lambda)\rho(\boldsymbol{x})I(\boldsymbol{x}, \boldsymbol{n}, \lambda) \\ &+ \kappa_{\rm sca}(\boldsymbol{x}, \lambda)\rho(\boldsymbol{x}) \int_{4\pi} \Phi(\boldsymbol{n}, \boldsymbol{n}', \boldsymbol{x}, \lambda) I(\boldsymbol{x}, \boldsymbol{n}, \lambda) d\Omega \\ &+ j(\boldsymbol{x}, \boldsymbol{n}, \lambda) \end{aligned} \tag{1.13}$$

The phase function Φ describes the distribution of scattering directions and is normalized to unity when integrated over 4π steradian solid angle. It couples the radiation fields from different positions and directions, making it a challenging equation to solve even numerically. In galaxies, both stellar and dust emissions contribute to the source term:

$$j(\boldsymbol{x}, \boldsymbol{n}, \lambda) = j_{\star}(\boldsymbol{x}, \boldsymbol{n}, \lambda) + j_{\rm dust}(\boldsymbol{x}, \lambda) \tag{1.14}$$

$j_\star$ depends on the stellar population and the geometry of stars. For simplicity, let us assume we have only one species of dust, described by a single $\kappa_{\rm abs}$ (for absorption) and Φ. In the limit of equilibrium emissions, $j_{\rm dust}$ is

$$j_{\rm dust}(\boldsymbol{x},\lambda) = \kappa_{\rm abs}(\boldsymbol{x},\lambda)\rho(\boldsymbol{x})B[T(\boldsymbol{x}),\lambda] \tag{1.15}$$

B is the Planck function, which describes the wavelength dependence of radiation of a blackbody at temperature T. T can be easily found by requiring that the total energy absorbed at each position balances the energy emitted:

$$\int_0^\infty \kappa_{\rm abs}(\boldsymbol{x},\lambda)\left[\int_{4\pi} I(\boldsymbol{x},\boldsymbol{n},\lambda)d\Omega\right]d\lambda = 4\pi\int_0^\infty \kappa_{\rm abs}(\boldsymbol{x},\lambda)B[T(\boldsymbol{x}),\lambda]d\lambda \tag{1.16}$$

However, for small grains, an average equilibrium temperature is not a good approximation to the dust emission (see § 1.1.6), and we calculate the contribute to dust emission at different temperatures weighted by the probability $P(T,\boldsymbol{x})$:

$$j_{\rm dust}(\boldsymbol{x},\lambda) = \kappa_{\rm abs}(\boldsymbol{x},\lambda)\rho(\boldsymbol{x})\left[\int_0^\infty P(T,\boldsymbol{x})B(T,\lambda)dT\right] \tag{1.17}$$

$P(T,\boldsymbol{x})$ can be solved from the heating and cooling rate of dust grains. The heating rate depends on the radiation intensity. In general, one can have dust grains with different κ due to different chemical compositions and sizes. The above equations can be easily extended into having multiple species.

1.3.6 Monte Carlo modeling

For radiative transfer in a 3D mixture of stars and dust, directly solving the 6-dimensional integro-differential equation is difficult, if not impossible. The Monte

Carlo (MC) method provides a practical way to solve the radiative transfer (RT) problem. Regardless of the dimensionality, the error in MC RT decreases as the reciprocal square root of the number of samplings. For a full review of MC RT for dust see Steinacker et al. (2013).

The MC method for RT involves tracing the trajectory of photon packets (or photons) and their interaction (absorption and scattering) with dust according to dust physics. Each photon samples the spatial distribution of dust attenuation and the radiation field, which is then used to calculate a self-consistent dust emission spectrum at each location. Since dust emission can be absorbed by dust, a common approach is to iteratively perform MC RT and dust emission calculation until the escaped luminosity converges. For efficient sampling of the radiation field, the spatial distribution of dust is typically divided into a discrete grid such that in each grid cell the radiation field is averaged.

1.3.7 Building a large grid of models

To recover the physical parameters of a galaxy by fitting its SED (see § 1.3.3), one can compute a set of models (with different input parameters) *in advance* and then compare the observed SED with modeled SEDs with statistical techniques such as chi-square minimization or Bayesian inference. Alternatively, one can use Monte Carlo Markov Chains (MCMC) to sample the probability distribution of the physical parameters and compute the model at each sampling point *as needed*. The benefits of

the former "pre-computation" method are that it is trivial to parallelize the computation to reduce the actual run time, and the resultant set of models can be re-used in other studies. The benefits of MCMC is that for models with many input parameters (i.e. a high-dimensional parameter space), the total amount of computation required can be significantly lower. With the pre-computation method, the computation required increases exponentially as the number of input parameters increase (known as the "curse of dimensionality"), whereas with MCMC the computation required increases only linearly, if properly implemented. Although the many dust and stellar parameters in our model qualify the problem as a high-dimensional one, we choose to use the pre-computation method for two reasons: (1) the sequential nature of MCMC makes it impractical for our radiative transfer models because each chain typically requires thousands of serially dependent models, and each model takes ~ 10 hours, and (2) we want to make the set of models available to other researchers to maximize the scientific impact. It is possible to parallelize the individual models to speed up MCMC, but this requires a significant programming effort and the inter-process communication could severely limit the scalability (the performance increase achieved with additional processors). In contrast, by running independent models at the same time, we can easily reach near-perfect scalability with the pre-computation method. In parallel computing, this is known as an "embarrassingly parallel" workload.

The known variations of dust and stellar properties result in a physically possible parameter space that is huge and uniformly sampling it is an inefficient use of

resources. Taking advantage of the varying rate of change in the output SED with respect to the input parameters, it is possible to develop a non-uniform sampling of the parameter space. For example, the output SEDs change as a function of stellar age, and the change is least predictable by interpolation at the youngest ages. Under the requirement that we reach 10% accuracy in the modeled SEDs, we need to sample the parameter space at the youngest ages at a higher density than older ages. The rate of change of the output SEDs has comparable complexity to the output SEDs themselves, and the density required at a certain age depends on other parameters (such as star formation rate) as well.

The actual computation takes place on supercomputers. Nowadays, due to the massive economy of scale, the most powerful general purpose supercomputers are built from processors that are similar to the ones found in consumer computers in terms of the core architecture. The job of a central processing unit (CPU) is to execute a sequence of instructions. Due to physical limitations and cost considerations, CPUs in supercomputers are typically just as fast as the average CPUs found in desktop computers. Modern supercomputers achieve their enormous computational throughput by packing a huge number (hundreds of thousands) of CPUs into coherent, high-density clusters. A single user (like us) typically only uses a tiny fraction of a supercomputer at a time, and the time slicing and CPU allocations are managed by the scheduling software. These CPUs are organized into nodes, which typically have 8-16 CPUs. For technical limitations of the operating system and the hardware,

the only way to make sure jobs would not interfere with the compute performance of each other is to run them on separate nodes. To avoid a single user dominating any nodes for a long period of time, the time slices usually have a limit of 8–24 hours, after which the running job would be forcefully terminated. Each of our model uses only one CPU and it is difficult to predict the run time precisely. To fully utilize every time-limited multi-CPUs slices, we make use of a "checkpointing" software that saves the current state of the running programs into persistent storage for continued execution in subsequent job slices.

1.4 This thesis

The impact of this thesis is twofold: (1) we conduct a large scale computation to model the global SEDs of galaxies based on radiative transfer with interstellar dust physics, and make the grid of models available to the public to improve the state of the art in dusty SED fitting, and (2) we study the dust properties and the accuracy of star formation rate indicators in nearby, normal star-forming galaxies by fitting the SEDs with the grid of models.

Previous research has found a range of interstellar dust properties. It is crucial to understand the physical processes that create these variations, to enhance both our knowledge on dust grains themselves, and the ability to correct for observations of objects affected by dust. As a simplification, there is at least a one-dimensional

variation in dust properties from the Milky way type dust (strong 2175 Å bump, weak far-UV rise) to the SMC type dust (weak 2175 Å bump, strong far-UV rise) that may be due to different size distributions and compositions of dust grains. In this thesis, we try to locate the position of dust properties of normal star forming galaxies on this one dimensional axis, and see if it is correlated with other physical parameters of the galaxies.

The effects of dust on the observables of galaxies are highly entangled with the variations of the stellar populations and the relative geometry of dust and stars. To take advantage of the full information available in the SEDs of the galaxies, we use radiative transfer and dust physics to model the full UV-IR SEDs. Proper handling of the dust absorption, scattering, and emission with dust grain physics in a 3-dimensional radiative transfer model increases the fidelity of the modeled SEDs at the expense of a larger amount of computation compared to simpler models. With the help of massively parallel supercomputers, we compute a large grid of radiative transfer models spanning over the range of possible physical parameters to map out the landscape of the SEDs of dusty galaxies.

The resultant grid of models is a useful tool to determine not only the type of dust present, but also a variety of other quantities. By fitting whole galaxies or pieces of galaxies, we can also simultaneously solve for the amount of dust, stellar age, stellar metallicity (a measure of heavy element abundance), and dust-star geometry. The grid can be explored to calibrate or train empirical relations between observable

quantities and underlying physical parameters. Since our grid spans the full range of know dust properties, the grid also provides constraints for objects of which the full SED is not available, for example, by imposing a prior on the allowed position of a galaxy on the color-color plot (a plot of two luminosity ratios of different wavelengths).

This thesis is organized as follow: In Chapter 2, we study the fraction of dust heated by young stars by simply using the the IR luminosity ratios. In Chapter 3, we present the DirtyGrid, our grid of radiative transfer models. In Chapter 4, we present results from the SED fitting of normal star-forming galaxies with the full DirtyGrid. In addition to recovering the dust properties and analyzing star formation rate indicators in these galaxies, we revisit the question in Chapter 2 with more sophisticated modeling. Lastly, in Chapter 5, we summarize our findings and suggest future directions.

Chapter 2

Young, UV-bright stars dominate dust heating in star forming galaxies

Abstract

In star forming galaxies, dust plays a significant role in shaping the ultraviolet (UV) through infrared (IR) spectrum. Dust attenuates the radiation from stars, and re-radiates the energy through equilibrium and non-equilibrium emission. Polycyclic aromatic hydrocarbons (PAH), graphite, and silicates contribute to different features in the spectral energy distribution; however, they are all highly opaque in the same spectral region—the UV. Compared to old stellar populations, young populations release a higher fraction of their total luminosity in the UV, making them a good source of the energetic UV photons that can power dust emission. However, given their relative abundance, the question of whether young or old stellar populations provide most of these photons that power the infrared emission is an interesting question. Using three samples of galaxies observed with the Spitzer Space Telescope and our dusty radiative transfer model, we find that young stellar populations (on the order of 100 million years old) dominate the dust heating in star forming galaxies, and old stellar populations (13 billion years old) generally contribute less than 20% of the far-IR luminosity.

2.1 Introduction

The infrared radiation from most star-forming galaxies is dominated by emission from dust grains heated by absorbed stellar energy. Dust emission is powered by absorption of radiation from ionizing and non-ionizing stars. Dust is most efficient at absorbing photons in the ultraviolet (UV) as the relative optical depth of dust is the highest in the UV (Gordon et al., 2003). Only early type (O and B) stars produce significant amounts of UV photons; however, these hot massive stars have short lifetimes (less than 100 million years) and are formed in relatively small numbers compared to less massive, less luminous, and cooler stars that produce very few UV photons. Given the initial mass function and evolutionary history, this implies that star-forming galaxies have a small mass fraction of UV bright, young stars as compared to UV faint, old stars. Thus, the question arises: which population of stars dominates the dust heating in star-forming clouds? The less numerous but much brighter in the UV young stars (< 100 Myr) or the numerous but much fainter in the UV old stars? How does this answer change when we consider the emission at specific IR wavelengths?

The majority of the IR energy from star-forming galaxies is emitted at far-IR ($\sim$100 μm) wavelengths. Historically, this far-IR emission has been identified as in-

frared cirrus emission from dust heated by non-ionizing populations (Helou, 1994), which are older than ~10 Myr. Lonsdale Persson & Helou (1987) interpreted the far-IR emission from spiral disks in terms of two thermal components with different temperatures and found that the cirrus component contributes more than half of the total far-IR flux. However, as old stars emit very few of the UV photons that power dust emission, it is possible that UV-bright young stars could dominate cirrus emission. For example, a small number of young stars embedded in a large optically thin cloud can result in a dilute radiation field, cold dust temperature and therefore cold cirrus emission.

Star formation rate (SFR) indicators are important observational probes of the star formation histories of galaxies. They are usually single-band or wavelength-integrated quantities that are presumed to trace a specific regime of recent star formation in a region or galaxy (Kennicutt, 1998). The most common SFR indicators include the Hα flux (tracing unobscured ionizing stars, < 10 Myr), UV (tracing unobscured ionizing and UV-bright, non-ionizing stars, < 100 Myr), and total infrared (TIR, tracing obscured star formation).

The UV and Hα flux are heavily attenuated by dust, with a typical extinction of 0-4 mag and 0-2 mag respectively (Kennicutt et al., 2009). Since the UV and Hα flux only trace the stellar light unabsorbed by dust, an accurate estimation of star formation activity requires a correction factor to account for the effect of dust. For starburst galaxies, emission-line diagnostics and UV colors may be used to such

purpose, but they are often difficult to obtain or highly uncertain (Kennicutt et al., 2009). An alternative way is to look at the IR flux, which accounts for the energy missing in the UV and the optical (Calzetti et al., 2007). Kennicutt et al. (2009) found that the combination of Hα and TIR provides a robust SFR measurement. Leroy et al. (2008a) and Bigiel et al. (2008) used the 24 μm flux combined with the GALEX far-UV to study the SFR in nearby galaxies.

TIR alone as a SFR indicator suffers from a number of problems. It does not trace unobscured star formation, and for the typical amount of dust in galaxies, a non-trivial amount of energy escapes in the UV and optical. Recalling the "cirrus emission" problem, TIR can only work well as an SFR indicator if the total infrared emission correlates well with newly formed stars ($<$ 100 Myr), instead of old stars that formed long ago. Therefore, understanding whether young stars or old stars dominate the TIR dust emission is an important step in interpreting the TIR SFR indicator. In addition, TIR is often integrated over a sparsely sampled wavelength interval in intermediate or high-redshift galaxies, which may introduce many uncertainties (Calzetti et al., 2007). Sauvage & Thuan (1992) found a systematic decrease of the L(far-IR)/L(H-alpha) ratio from early- to late-type spirals, and suggested a systematically varying cirrus fraction as the explanation, accounting for 86 percent of L(far-IR) for Sa galaxies to about 3 percent for Sdm galaxies. Xu & Helou (1996) also found that the heating of the diffuse dust is dominated by optical radiation from stars at least a billion years old in M31. With these results, it is important to subtract the

cirrus emission from the total infrared luminosity in the calculation of star formation rate.

In the simplest model, dust emission can be thought of as modified blackbody radiation at a certain temperature plus emission features. However, equilibrium dust emission is not the only possible emission path. Duley (1973) pointed out that non-equilibrium dust emission should also be important and this has been confirmed observationally (e.g., Sellgren, 1984). Upon the absorption of an energetic photon, a large molecule or small dust grain can attain a very high temperature for a short period of time before it cools. In many situations, if non-equilibrium heating is not considered, the observed mid-IR luminosity implies an unrealistically high equilibrium dust temperature. While older stars can rarely excite dust grains to produce non-equilibrium heating, this type of heating clearly dominates the mid-IR emission from star-forming galaxies.

Recent interesting results from the Herschel observatory have begun exploring the problem of the source of dust heating using the far-IR and sub-mm. Specifically, in a study of M81, Bendo et al. (2010a) found that the far-IR to sub-mm (160-500 μm) emission is dominated by dust heated by evolved stars while the 70 μm emission is caused by the active galactic nucleus and young stars in star forming regions. From a study of 51 nearby galaxies, Boselli et al. (2010) found that the warm dust (f60/f100) correlates with star formation, while cold dust (f350/f500) anti-correlates. Our study does not probe cold dust in the submillimeter range, but we plan to do so in a later

paper.

In this paper, we examine the relationship between IR luminosity and the age of stellar populations. Through the use of a self-consistent radiative transfer and dust emission model, observed dust properties, and stellar and dust geometries designed to represent galactic environments, we compare our results to observed galaxies (the SINGS sample, Kennicutt et al. (2003), the starburst galaxies in Engelbracht et al. (2008), and the LVL sample, Dale et al. (2009)) and attempt to give a quantitative answer on the age of the stellar populations that dominates the IR emission in star forming galaxies.

2.2 Method

2.2.1 Model

DIRTY (DustI Radiative Transfer, Yeah!) is a self-consistent Monte Carlo radiative transfer model (Gordon et al., 2001; Misselt et al., 2001). Due to its Monte Carlo nature, it allows for arbitrary dust and stellar distributions. It computes emission from the three standard dust grain components (Weingartner & Draine, 2001)—carbon grains, silicates, and polycyclic aromatic hydrocarbons (PAH). One of the key strengths of DIRTY is that it is completely self-consistent. It avoids assumptions whenever possible; the radiation field is directly calculated from radiative transfer, instead of the usual method of scaling the standard solar neighborhood radiation

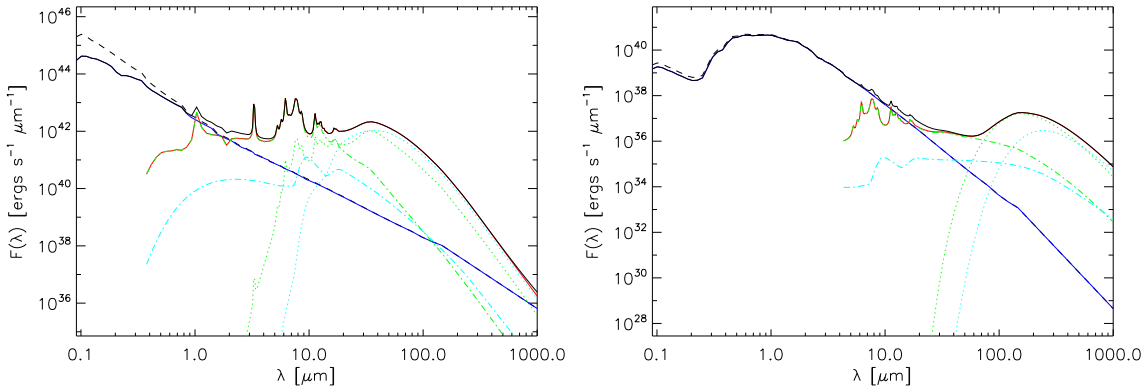

Figure 2.1: Example global SED outputs from DIRTY for a young (10 Myr, left) and an old (13 Gyr, right) stellar populations, each with a mass of 10^{10} $M_{\odot}$, Milky Way type dust, 10 kpc radius, and an optical depth of $\tau_v = 1$. The former has a SHELL geometry and the latter has a CLOUDY geometry. The dashed black line is the input stellar SED. The solid black, blue and red lines are the total output SED, the radiative transfer component (diffuse/extincted plus scattered) and the total dust emission. Among the dust emission components, the green and light blue lines represent carbonaceous and silicate grains; the dotted and dash-dotted lines represent equilibrium and non-equilibrium emission, respectively.

field (Draine, 2009). The initial radiation field is obtained from an external spectral evolutionary synthesis model. Both equilibrium and non-equilibrium emission are calculated from the radiation field and their contributions to the radiation field itself are iteratively taken into account. DIRTY has been used to model a variety of situations, for example, the dusty starburst nucleus of M33 (Gordon et al., 1999) and the general behavior of galaxies (Witt & Gordon, 2000). Figure 2.1 shows examples of global spectral energy distributions (SED) from DIRTY.

Young and old galaxies are best described by different dust geometries, which can lead to different dust absorption efficiencies and effective optical depths (Witt et al., 1992a). Following the notation of Witt & Gordon (2000), we use the CLOUDY and

Table 2.1: Model parameters used in DIRTY.

Parameter	Values
Optical depth at V band (τ_v)	0.2 - 5.0
Stellar age (Myr)	1 - 13000
Radius (pc)	100 - 10000
Dust model	Milky Way dust (with $R_V = 3.1$, $b_C = 6 \times 10^{-5}$) and SMC Bar dust from Weingartner & Draine (2001)
Stellar model	PEGASE 2 (Fioc & Rocca-Volmerange, 1997) with instantaneous bursts
Metallicity	Solar (0.02) and 1/5 Solar (0.004)

SHELL geometries. In the CLOUDY geometry, stars are uniformly distributed in a spherical volume, and a dusty core is located within 0.69 times of the radius of the stellar distribution; whereas in the SHELL geometry, stars extend only to 0.3 times of the outer radius and are surrounded by a concentric shell of dust from 0.3 to 1.0 of the outer radius. See Figure 1 of Witt & Gordon (2000) for a graphical description of the CLOUDY and SHELL geometries.

For both geometries, the stellar density per unit volume is constant. The CLOUDY model reproduces the general characteristics of old stellar populations in galaxies with strong central bulges, where the majority of stars are found outside of the dust. The SHELL model mimics a young star cluster with surrounding clouds. It has been shown that starbursts require a SHELL geometry to explain various color-color plots

(Gordon et al., 1997) and the attenuated-to-intrinsic ratios of hydrogen lines (Calzetti, 2001). In this study, we use SHELL for stars that are 100 Myr old or younger and CLOUDY for older ones. Other model parameters can be found in Table 2.1.

Witt & Gordon (1996) found that it is necessary to model interstellar dust as a multi-phase medium. To achieve this, a small fraction (15 % total filling factor) of clumps of high density dust is randomly placed into a field of low density dust with 100 times lower density in the global dust geometries mentioned previously. Without the clumpiness, the effectiveness of dust absorption would be overestimated. In this study, we exclusively use clumpy dust distributions. The optical depth averaged over all sightlines (from infinity to the center of the geometry) is normalized to the desired value of τ_v.

We use the spectral evolutionary synthesis (SES) model PEGASE 2 (Fioc & Rocca-Volmerange, 1997) as the stellar input to our model. We model starbursts of various ages with solar and 1/5 solar metallicity and the Padova evolutionary tracks. An old galaxy may contain both old stellar populations and young stellar populations, although the latter is expected to be much less abundant considering that the typical timescale for gas depletion is about 3 Gyr (Pflamm-Altenburg & Kroupa, 2009). The time-dependent profile of star formation could be modeled as an exponentially decaying burst (Searle et al., 1973; Conti et al., 2003). However, since we want to model the characteristics (the luminosity ratios) of stellar populations at a certain age, we use instantaneous starbursts. To bracket the possible real world scenarios, we model

the extreme cases of very young (1 Myr) and very old (13 Gyr) starburst populations. Gas continuum and emission of recombination lines, as calculated by PEGASE, are included. See Gordon et al. (1999) for a detailed discussion on how we use spectral evolutionary synthesis models with our dusty radiative transfer model.

The dust extinction curve for stars in the Milky Way (MW), Small and Large Magellanic Clouds (SMC and LMC) are found to have overall similar shapes with significant variation in the UV (Gordon et al., 2003). There are two distinct features that differentiate the different types of dust. The first one is the 2175 Å bump, which is found to vary in strength on average between the MW diffuse ISM/LMC general (strong bump), LMC2 (near 30 Dor)/SMC Wing (weak bump), and SMC Bar (no bump). The second is the far UV rise, which generally varies in strength inversely with the 2175 Å bump. Dust properties can be influenced by star forming activity and metallicity. In particular, Gordon et al. (1997) found that the SMC Bar type dust (lacking a 2175 Å bump) describes the starburst galaxies better than either the LMC or MW type dust. From the GMASS survey, Noll et al. (2009b) found that there is a wide range of UV dust properties, including those that are intermediate between SMC Bar and LMC2 type dusts. Modeling results show that the type of dust can affect the strength of PAH features (Draine et al., 2007), which in turn affects the IR observations. As a result, it is important to choose an appropriate dust type for our study, and to explore the sensitivity of our results to the dust type. To span the whole range of known dust properties, we use SMC Bar type dust and Milky Way

type dust. For a fair comparison, we use the dust models of Weingartner & Draine (2001) for both the SMC and Milky Way type dust.

Radius and stellar mass are not independent dimensions in our model. Since the radiation intensity drops as the square of the radius, an increase in the model radius by a factor of x can be compensated by an increase in the stellar mass by a factor of x^2. The two cases give the same radiation intensity in each grid cell in the model, and therefore the same dust temperature. The resultant SEDs will have the same shape, with the only difference being the lower overall luminosity in the latter case. This has been confirmed by test runs of our model; for example, a stellar population with 10^{11} solar masses and 10 kpc radius gives the same SED as the one with 10^9 solar masses and 1 kpc radius, when the luminosity in the latter is scaled up by a factor of 100 (all the other parameters are unchanged). Since our study is based on the ratios of luminosities, a larger, more luminous galaxy and a smaller, dimmer galaxy with same radiation field intensity give the same result.

Due to the Monte Carlo and iterative nature of our model, the run time varies significantly depending on the parameters. The fastest models take about 4 CPU hours on a 2.33 GHz Intel Xeon processor, while the slowest ones often need about 2 days. The average run time is about 20 hours. Each model uses a single thread and we launch multiple processes in parallel to utilize all the CPU cores in multi-core processors. We iterate the radiative transfer and dust emission processes until the global energy conservation error is within 5%. The resultant uncertainty of flux at

each wavelength is usually within 1%.

2.2.2 Luminosity ratios

To compare the modeled SED with infrared observations, we calculate the luminosities in the IRAC and MIPS bands with calibrated response functions (Hora et al., 2008; Engelbracht et al., 2007; Gordon et al., 2007; Stansberry et al., 2007). Since the galaxies in our sample have a very wide range of total luminosity, we study luminosity ratios instead of raw luminosities. We normalize the mid- and far-IR luminosities by the IRAC1 (3.6 μm) luminosity, and the resulting ratios are the characteristics of the dust and stellar populations that we compare with our model. These luminosity ratios are measures of the efficiency of the stellar and dust distribution at producing radiation in a certain wavelength regime (relative to IRAC1). At 3.6 μm, the IRAC1 band is only mildly contaminated by dust emission (e.g., the 3.3 μm aromatic/PAH feature), and is less affected by dust extinction than the shorter wavelengths. The IRAC1 luminosity can be considered as a proxy of stellar luminosity and an approximate measure of mass, although the mass-to-light ratio depends on their underlying stellar populations and the infrared colors (Bell & de Jong, 2001). The combination of the PEGASE SES and DIRTY models account for stellar age, dust emission, and absorption self-consistently. As we see in later discussions, the luminosity ratios are robust against changes in radius or total stellar luminosity.

2.2.3 Data

From the SINGS (Spitzer Nearby Galaxies Survey) dataset (Kennicutt et al., 2003), we have good measurements of the UV, visible and IR fluxes for a number of nearby galaxies. They range from spiral to elliptical to irregular galaxies, and are a good representation of a wide range of galaxies. We removed 4 galaxies (M81 Dwarf A, NGC 3034, Holmberg IX, and DDO 154) for which the IRAC or MIPS band fluxes are not well measured (either an upper limit or saturated). For the remaining 71 galaxies, we calculate the luminosity from the flux data from Dale et al. (2007) and distance data from Kennicutt et al. (2003). The metallicity is calculated from the average of the “high" and “low" oxygen abundance values from Moustakas et al. (2010); the same method was used in Calzetti et al. (2010). Figure 2.2 shows the wide range of galaxies types in the SINGS sample, where we have used Eq. 22 from Draine & Li (2007) to compute $L_{\rm TIR}$.

To expand the range of galaxies studied, we include the starburst galaxies from Engelbracht et al. (2008) and the Local Volume Legacy (LVL) sample from Dale et al. (2009). The starburst galaxies have a higher fraction of recent star formation and UV-bright young stars. Their data include imaging and spectroscopy from the Spitzer Space Telescope, as well as ground-based near-infrared imaging. The Engelbracht sample consists of 66 local star forming galaxies of which 65 have high quality IRAC and MIPS data available; UM 420 was dropped from our sample because the MIPS data were not available. For this sample we take all flux, distance and metallicity

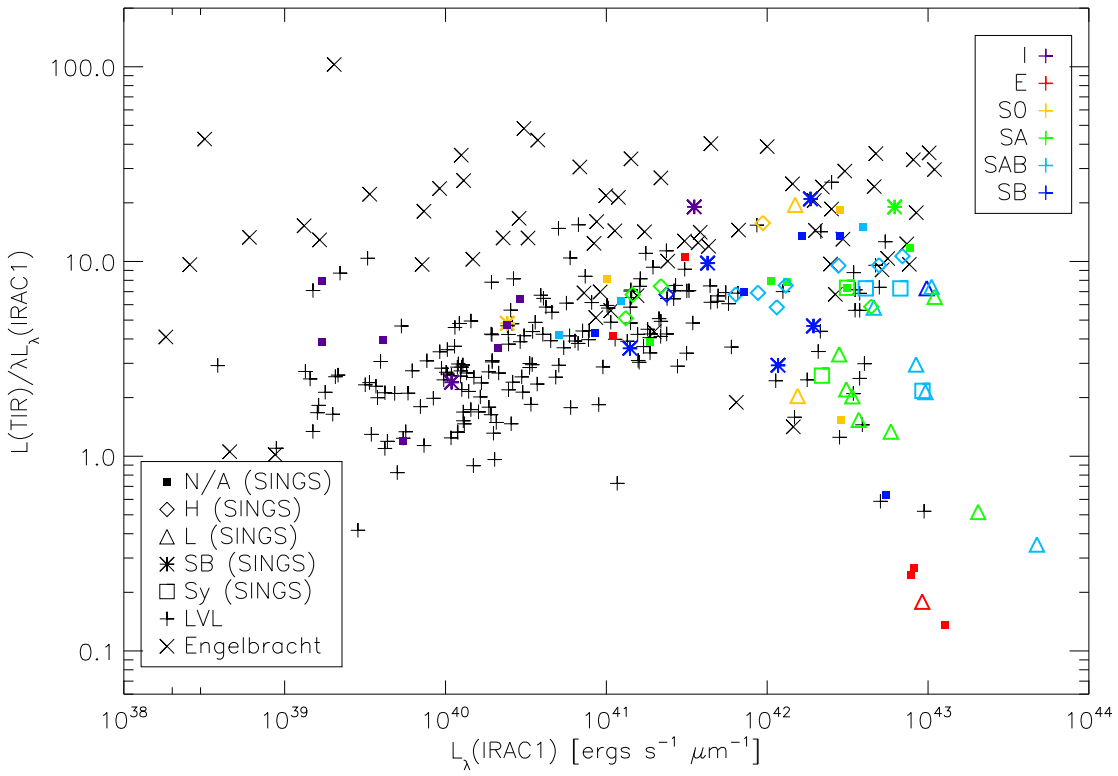

Figure 2.2: TIR to IRAC1 luminosity ratio vs IRAC1 luminosity for our sample. For the SINGS galaxies (Kennicutt et al., 2003), morphological types are shown in different colors and nuclear types are shown in different symbols. The SINGS galaxies span a large range of galaxy types, from spirals (S) to ellipticals (E) and irregulars (I). The nuclear type H, L, SB and Sy stand for H II, LINER, starburst, and Seyfert. The Engelbracht et al. (2008) starburst galaxies and the LVL galaxies (Dale et al., 2009) are shown in black "×" and "+" respectively.

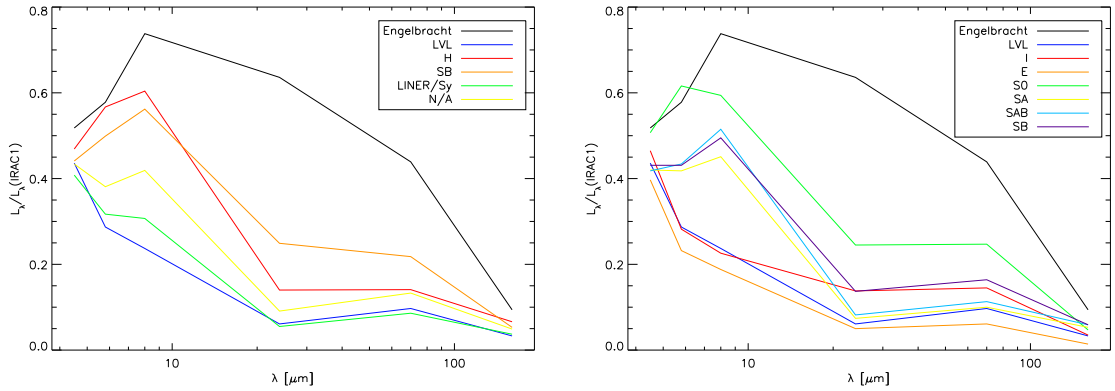

Figure 2.3: The average SEDs (normalized by IRAC1 luminosity) of galaxies with different nuclear types (left) and morphological types (right), using the data in Table 2.2. Note that the Engelbracht et al. (2008) starburst galaxies show a significantly higher ratio in MIPS24 and MIPS70 compared to the other galaxies. On the other hand, elliptical galaxies (orange, right) give the lowest luminosity ratios, as they are the least efficient in producing mid- and far-IR fluxes.

values from Engelbracht et al. (2008). On the other hand, the LVL is a statistically unbiased sample of 258 galaxies in the local universe out to 11 Mpc which consists mainly of dwarf galaxies, and we take flux and distance values from Dale et al. (2009) and metallicity values from Marble et al. (2010). We removed galaxies without good IRAC and/or MIPS measurements (no data or flux available only as an upper bound) and galaxies without metallicity data, and arrived at a sample of 194 galaxies.

In Table 2.2 we list the statistics of the band ratios of our sample. The SINGS galaxies are classified into different nuclei and morphological types according to Kennicutt et al. (2003). We keep the Engelbracht sample (as a group of starburst galaxies) and the LVL sample (representing the dwarf galaxies) separate from the SINGS' categories for a clear statistical comparison. Each number in the table is the average (plus or minus the standard deviation) of the ratio of the given band luminosity to

Table 2.2: Statistics of the luminosity ratios ($L_\lambda(\lambda_1)/L_\lambda(\lambda_2)$).

Dataset	Count	IRAC2/IRAC1	IRAC3/IRAC1	IRAC4/IRAC1	MIPS24/IRAC1	MIPS70/IRAC1	MIPS160/IRAC1
SINGS	71	0.433 ± 0.073	0.411 ± 0.274	0.438 ± 0.362	0.110 ± 0.151	0.131 ± 0.122	0.049 ± 0.031
H II nuclei	13	0.469 ± 0.147	0.567 ± 0.402	0.604 ± 0.329	0.140 ± 0.181	0.141 ± 0.058	0.066 ± 0.017
Starburst nuclei	9	0.441 ± 0.036	0.499 ± 0.314	0.562 ± 0.457	0.249 ± 0.273	0.218 ± 0.181	0.053 ± 0.032
LINER/Seyfert nuclei	21	0.408 ± 0.029	0.317 ± 0.127	0.307 ± 0.211	0.055 ± 0.077	0.086 ± 0.128	0.037 ± 0.028
Others	28	0.434 ± 0.045	0.381 ± 0.244	0.419 ± 0.406	0.091 ± 0.093	0.133 ± 0.105	0.049 ± 0.034
Type I	9	0.465 ± 0.041	0.282 ± 0.186	0.226 ± 0.288	0.138 ± 0.224	0.145 ± 0.121	0.035 ± 0.019
Type E	6	0.397 ± 0.034	0.232 ± 0.163	0.188 ± 0.271	0.050 ± 0.095	0.061 ± 0.104	0.014 ± 0.021
Type S0	7	0.507 ± 0.200	0.616 ± 0.622	0.594 ± 0.630	0.245 ± 0.262	0.247 ± 0.207	0.047 ± 0.036
Type SA	19	0.420 ± 0.035	0.418 ± 0.208	0.451 ± 0.325	0.074 ± 0.116	0.100 ± 0.087	0.053 ± 0.031
Type SAB	18	0.418 ± 0.023	0.434 ± 0.150	0.515 ± 0.294	0.082 ± 0.064	0.113 ± 0.072	0.059 ± 0.026
Type SB	12	0.431 ± 0.041	0.431 ± 0.255	0.495 ± 0.342	0.137 ± 0.143	0.164 ± 0.143	0.059 ± 0.033
Engelbracht	65	0.518 ± 0.184	0.578 ± 0.395	0.738 ± 0.632	0.636 ± 0.612	0.439 ± 0.345	0.094 ± 0.163
LVL	194	0.436 ± 0.037	0.287 ± 0.158	0.237 ± 0.225	0.061 ± 0.104	0.097 ± 0.076	0.033 ± 0.022

the IRAC1 luminosity. Figure 2.3 shows the table entries graphically. Among the SINGS galaxies, the starburst and H II nuclei tend to have higher luminosity ratios while those without active nuclei tend to have lower luminosity ratios. Galaxies with Seyferts (Sy) and LINERS (L) nuclei are in between the two extremes. While our model does not simulate Seyfert (Sy) or LINERS (L) nuclei, the luminosity ratios of these galaxies are within the range of the other galaxies, and we keep them in our study. Focusing on the MIPS160 column, we notice that the luminosity ratio for elliptical galaxies is significantly lower than the other types of galaxies. On the other hand, the Engelbracht et al. (2008) starburst galaxies show a much higher ratio in all the MIPS bands, meaning that they are more efficient in producing far-infrared emission.

2.3 Results

2.3.1 Dust type

In Figure 2.4, we plot the MIPS24 to IRAC1 luminosity ratio for our galaxy sample, together with models with SMC Bar (left) and Milky Way type dust (right). Different models on the same curve have different stellar mass, characterized by their different IRAC1 luminosity on the x-axis. Here we use $\tau_v = 1.0$ and radius $= 10$ kpc, but we see similar trends with other parameters. We note that the curves are relatively flat until they tick up in the regime of very high IRAC1 luminosity. This is

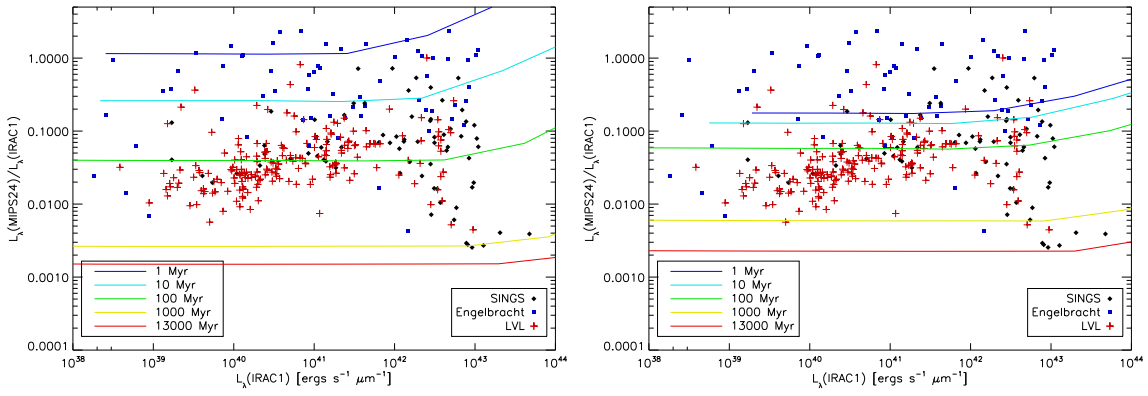

Figure 2.4: Comparison of SMC Bar (left) and Milky Way (right) type dust. Shown in the figures are the MIPS24 (24 μm) to IRAC1 (3.6 μm) luminosity ratios against the IRAC1 luminosity. The curves represent results from the DIRTY radiative transfer models with different stellar ages, while the data points represent our galaxy sample.

because dust emission in the MIPS24 band is dominated by non-equilibrium heating for young stellar populations, or stellar continuum for old stellar populations. In either case, the fraction of MIPS24 to IRAC1 is a constant. Only at very high luminosity, does the dust temperature become high enough for equilibrium heating to make a comparable contribution and the curves start to turn up. We discuss the effects of non-equilibrium emission in section 2.3.4.

From 1 Myr old to 13 Gyr old, the models with SMC Bar type dust roughly span the whole range of luminosity ratios for the galaxies. On the other hand, the models with MW type dust are unable to cover all the galaxies. Even at the youngest age of 1 Myr, the model curve is below some galaxies (including most of the Engelbracht et al. (2008) starburst galaxies). At the other extreme, both types of dust do equally well for low MIPS24 to IRAC1 luminosity ratios. None of the galaxies have luminosity ratios lower than our oldest models (13 Gyr, close to the age of the universe). We see a

similar distinction in the MIPS70 to IRAC1 luminosity ratios. From this perspective, the SMC Bar type dust is a better choice for our study, although this is different from Draine et al. (2007) who found that the SINGS galaxy sample has similar dust-to-gas ratio and similar PAH abundance to MW type dust. It is possible that the different results from the dust types are due to dust processing. If the MW type dust is more susceptible to destruction in a UV radiation field compared to the SMC Bar type dust, the former will produce less far-IR emission per unit IRAC1 luminosity and therefore a lower luminosity ratio. Unless otherwise specified, discussions in the following sections refer to SMC Bar type dust. Despite the differences we discuss here, the conclusion we draw about the age of stellar populations heating the dust (see section 2.3.5) is independent of the type of dust.

2.3.2 Age

To study what stellar age would best reproduce the observed luminosity ratios, we fix the other model parameters and see how the model results change as a function of stellar age. Knowing that τ_v is on the order of unity for normal disk galaxies (Holwerda et al., 2007), we assume an optical depth of $\tau_v = 1.0$. Dale et al. (2006) also found that the average attenuation is $A_v = 1.0$ (which equals $\tau_v = 0.92$) for a large portion of SINGS and some archival sources from ISO and Spitzer. We set the radius to be 10 kpc, a reasonable size of a galaxy. Our results do depend on the choice of optical depth and radius, but we first see what we find with these values.

In section 2.3.3 we examine the effect of varying the optical depth and radius.

In Figure 2.5, we plot the luminosity ratios versus IRAC1 luminosity for IRAC and MIPS bands; the five curves correspond to five different stellar ages. The younger three (1, 10 and 100 Myr) are modeled with the SHELL geometry and the older two (1 and 13 Gyr) are modeled with the CLOUDY geometry. Younger populations are more efficient in producing IR due to being more embedded in the dust and their much higher intrinsic L(UV)/L(IRAC1) ratios, and the difference is most pronounced in the mid-IR. Taking the IRAC4/IRAC1 vs IRAC1 plot as an example, we see that the 10 Myr line matches the data the best (among the models with SMC type dust). The 1 Myr old models produce too much 8 μm flux (per unit 3.6 μm flux, on average), while the older models produce too little. For the MIPS24/IRAC1 plot, a combination of the 10 Myr old and 100 Myr old models match the median of the data, while for the MIPS160/IRAC1 plot, a combination of the 100 Myr old and 1 Gyr old models would do. This shows that the age of the stellar populations that dominates IR emission is on the order of 100 million years. The difference from IRAC4 to MIPS160 shows that the importance of younger stellar populations (less than 100 Myr) is relatively higher at shorter wavelengths.

As we vary the age, the IRAC2-to-IRAC1 plot shows a different trend from the other plots. Both the data and the models fall into a very narrow range (~0.5 dex). This is because this color is dominated by stars only and the colors of populations of stars in the mid-IR are relatively constant; it is much less sensitive to dust compared

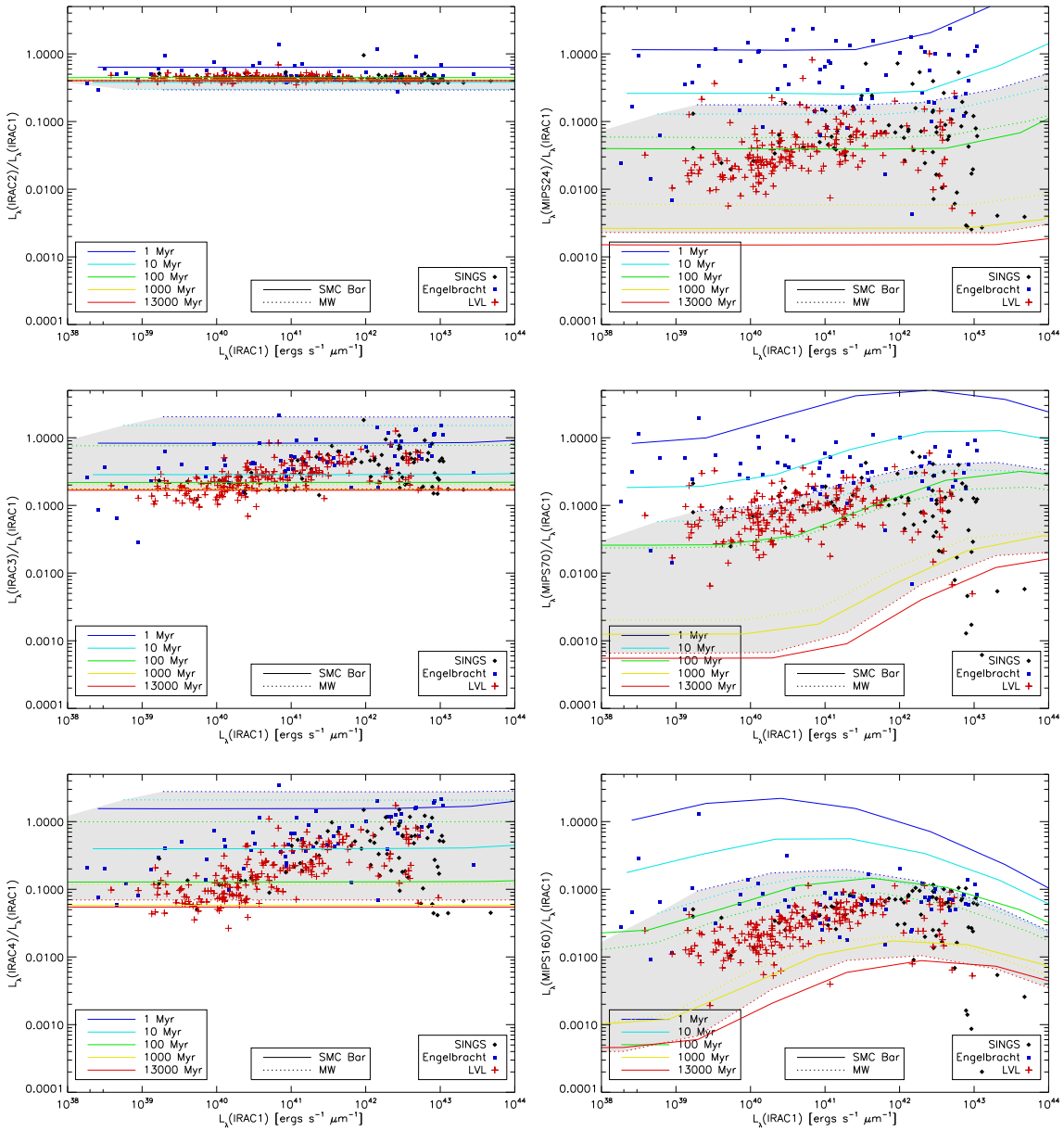

Figure 2.5: Luminosity ratios vs IRAC1 (3.6 μm) luminosity plots for the IRAC (left) and MIPS (right) infrared bands. The models with different stellar ages (1 Myr to 13 Gyr old) are shown as curves with different colors; MW and SMC Bar type dust are in different line styles (dashed and solid respectively). The area covered by models with MW type dust is shaded in light gray, and is noticeably smaller than the range spanned by models with SMC Bar type dust in the far-IR. They are compared to these observed galaxies: the SINGS galaxies (Kennicutt et al., 2003) in black diamonds, the Engelbracht et al. (2008) starburst galaxies in blue squares, and the LVL galaxies (Dale et al., 2009) in red crosses. Here we use solar metallicity, $\tau_v = 1$ and a radius of 10 kpc.

to the longer wavelengths.

Note that the data points that have very low luminosity ratios in the MIPS bands are elliptical galaxies. The elliptical galaxies are shown as red symbols in Figure 2.2, and they show up in the lower right corner in the MIPS70 and MIPS160 plots. From our models, older stellar populations produce less dust emission per unit near-IR luminosity, and therefore should be better at explaining elliptical galaxies. However, the luminosity ratios of these galaxies are so low that even the oldest models (at about the age of the universe) cannot explain them. Noting that we have used $\tau_v = 1.0$ and 10 kpc radius in Figure 2.5, this result suggest that the optical depth of elliptical galaxies could be lower than the average galaxy, or that their radii are larger than our modeled value. The former is the most probable explanation, as the zero-dust case for our oldest model gives a value of ~0.0005 for MIPS160/IRAC1, low enough to explain the elliptical galaxies.

2.3.3 Optical depth and radius

To illustrate the effect of the optical depth and radius of the model region on the results, we fix the stellar age at 100 Myr and vary the optical depth and radius in Figure 2.6. Dust with higher optical depth absorbs more energy and emits more far-IR radiation, and therefore gives a higher ratio in the plots. A larger radius dilutes the radiation field, lowers the dust temperature and shifts the equilibrium dust emission peak to a longer wavelength in the SED. In our luminosity ratio diagrams, it shifts the

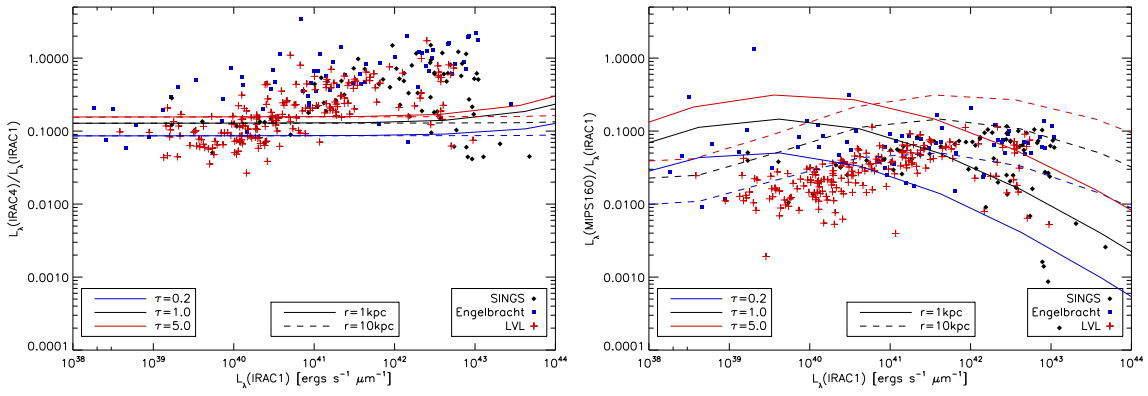

Figure 2.6: IRAC4 (8.0 μm; left) and MIPS160 (160 μm; right) to IRAC1 (3.6 μm) luminosity ratios against IRAC1 luminosity for a fixed stellar age (100 Myr). Here we can study the effect of radius and optical depth in our model.

curves horizontally to the right. Because of the behavior of our model as explained in Section 2.2.1, we may also interpret the effect with mass surface density ($M/\pi r^2$). With the same reasoning, as the mass surface density decreases, the curves shift to the right.

As we study the effects of variations in optical depth and radius, we find a noticeable difference for the IRAC bands and the MIPS bands. For MIPS bands, changing the two parameters can change the curves significantly. This is evident on the plot for MIPS160 (Figure 2.6, right). However, in the IRAC bands, the curves are flatter and span a narrower range. As explained in section 2.3.1, this is because the dust emission in the IRAC bands is dominated by non-equilibrium heating. And since the curves are flat, shifting them horizontally makes no difference in our results; they are not very sensitive to the choice of radius. See section 2.3.4 for a discussion on equilibrium vs non-equilibrium dust emission.

From Figure 2.6 we can see that old stellar populations could possibly reproduce the observed luminosity ratios in Figure 2.5 only if the optical depth is very high, say 5 or 10. This is not realistic, as Holwerda et al. (2007) has shown that for normal disk galaxies τ_v is on the order of unity. In addition, if τ_v has such a high value, the optical depth at shorter wavelengths will be even greater and we wouldn't be able to observe these galaxies in UV.

2.3.4 Equilibrium and non-equilibrium emission

To help interpret our results, we examine the fraction of luminosity due to non-equilibrium heating. The plots in Figure 2.7 shows the different behavior of the fraction in different IR bands.

In the far-IR (MIPS70 to SPIRE500), non-equilibrium emission is negligible compared to equilibrium emission for a wide range of IRAC1 luminosity. Only at very low IRAC1 luminosity and large (> 10 kpc) radii does non-equilibrium emission contribute significantly in the far-IR. When the flux is dominated by equilibrium emission, it depends on the dust temperature and therefore model parameters like the radius, and this can be seen in the MIPS160 curves of Figure 2.6.

On the other hand, the mid-IR bands (e.g., IRAC) exhibit different behavior. When modeled with young stellar populations (1 - 100 Myr old), the flux is dominated by non-equilibrium emission because of the large amount of highly energetic UV photons. When modeled with older stellar populations, the fraction of non-

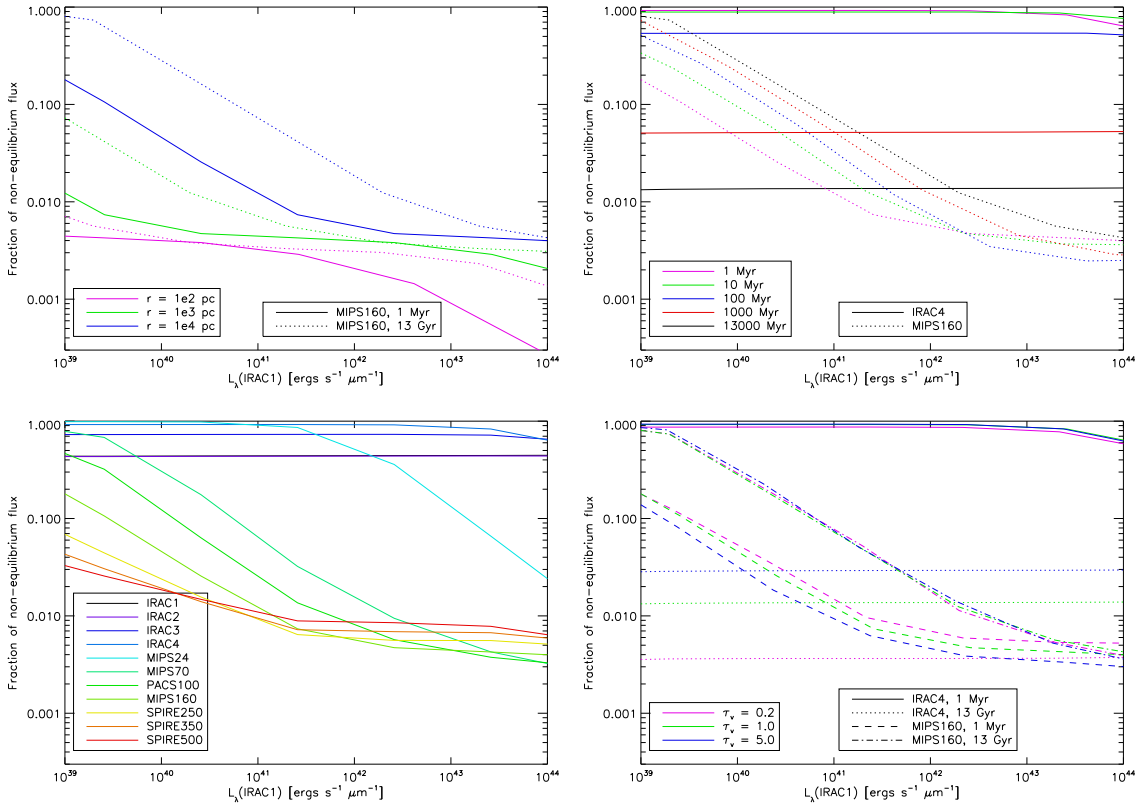

Figure 2.7: The modeled fraction of luminosity due to non-equilibrium heating plotted against the IRAC1 band luminosity for various model parameters. Unless specified in the legend, the model parameters are $\tau_v = 1$, age = 1 Myr, and r = 10 kpc.

equilibrium emission is small, so equilibrium emission is the major source of the IR flux from dust. However, the dust temperature is not high enough to emit significant energy in mid-IR, so the flux is dominated by the stellar continuum. Either way, equilibrium emission does not play a significant role in the mid-IR bands, except at extremely high luminosities. Therefore, the radius parameter (which affects the dust temperature) does not change the result as much as they do for the far-IR bands.

Non-equilibrium emission is dominated by very high energy UV photons. As

opacity goes up with the energy of the photon, most high energy UV photons are likely to be absorbed even in a low τ_v environment. IRAC4 is dominated by non-equilibrium emission, therefore further increases in τ_v do not result in more high energy UV photons being absorbed and so the IRAC4 to IRAC1 luminosity ratio would not change significantly. If we go back to Figure 2.6, we see that the luminosity ratio is less sensitive to the optical depth in IRAC4 then in MIPS160. MIPS24 is the turnover point for the two behaviors. This explains why the curves behave so differently in IRAC plots and MIPS plots as we change the model parameters in the previous sections.

2.3.5 Constraints on the fraction of luminosity from old stars

In this section, we attempt to calculate the fraction of IR luminosity that could be due to old stars using simple assumptions. Assume there are two non-interacting populations of stars, one younger and one older. When we look at models with the same IRAC1 luminosity as an observed galaxy, if the observed luminosity (say in MIPS160) is in between the younger (higher) and older (lower) luminosities, there exists a fraction x of old stars of which the combination of the two model stellar populations reproduces the observed luminosity. We can write the luminosity of the i^{th} galaxy at wavelength λ, $L_i(\lambda)$ as

$$L_i(\lambda) = [1 - x_i(\lambda)]Y_i(\lambda) + x_i(\lambda)O_i(\lambda) \tag{2.1}$$

where x_i is the fraction of old stars, and Y_i and O_i are the luminosities of the young and old models (e.g., 1 Myr and 13 Gyr) that have the same IRAC1 luminosity as the i^{th} galaxy, respectively. The two terms represent the contribution of luminosity from the two populations. Eq. 2.1 can be inverted to solve for x_i to yield

$$x_i(\lambda) = \frac{L_i(\lambda) - Y_i(\lambda)}{O_i(\lambda) - Y_i(\lambda)} \tag{2.2}$$

When we use the formula for galaxies that have a luminosity (per unit IRAC1 luminosity) lower than the one given by the old model, x_i will be greater than 1, which is not physical. This corresponds to the case where the real galaxy is less efficient than the old model in producing dust emission. Such a situation can arise if, for example, the galaxy has a lower average optical depth than that assumed in our model. As a simplification we simply set $x_i = 1$ in these cases. On the other hand, for galaxies with the luminosity per unit IRAC1 luminosity higher than our young model, x_i will be negative and we set $x_i = 0$. After solving for the fraction of old stars x_i, we can calculate the fraction of luminosity due to old stars f_i:

$$f_i(\lambda) = \frac{x_i(\lambda)O_i(\lambda)}{L_i(\lambda)} \tag{2.3}$$

Using 1 Myr (young) models and 13 Gyr (old) models, we calculate the fractions x and f for the 3 samples of galaxies, and tabulate the results for the IRAC4, MIPS24,

Table 2.3: Calculated fractions of old stars - SINGS sample.

Dust Type	Flux band	Fraction of old stars x	Fraction of luminosity from old stars f	Number of galaxies with $x_i = 1$	Number of galaxies with $x_i = 0$
MW	IRAC4	0.854 ± 0.018	0.285 ± 0.078	5	1
MW	MIPS24	0.611 ± 0.102	0.068 ± 0.017	1	9
MW	MIPS70	0.569 ± 0.110	0.145 ± 0.071	3	8
MW	MIPS160	0.572 ± 0.107	0.181 ± 0.062	4	7
SMC Bar	IRAC4	0.736 ± 0.055	0.220 ± 0.061	2	1
SMC Bar	MIPS24	0.942 ± 0.008	0.050 ± 0.007	1	1
SMC Bar	MIPS70	0.964 ± 0.001	0.120 ± 0.053	3	1
SMC Bar	MIPS160	0.931 ± 0.004	0.203 ± 0.055	3	1

Table 2.4: Calculated fractions of old stars - Engelbracht et al. (2008) sample.

Dust Type	Flux band	Fraction of old stars x	Fraction of luminosity from old stars f	Number of galaxies with $x_i = 1$	Number of galaxies with $x_i = 0$
MW	IRAC4	0.758 ± 0.049	0.191 ± 0.058	1	1
MW	MIPS24	0.184 ± 0.101	0.021 ± 0.006	1	40
MW	MIPS70	0.174 ± 0.083	0.022 ± 0.014	1	36
MW	MIPS160	0.516 ± 0.105	0.088 ± 0.016	1	8
SMC Bar	IRAC4	0.590 ± 0.097	0.139 ± 0.040	1	6
SMC Bar	MIPS24	0.630 ± 0.118	0.017 ± 0.003	1	7
SMC Bar	MIPS70	0.830 ± 0.039	0.020 ± 0.005	1	2
SMC Bar	MIPS160	0.913 ± 0.013	0.097 ± 0.009	1	1

Table 2.5: Calculated fractions of old stars - LVL sample.

Dust Type	Flux band	Fraction of old stars x	Fraction of luminosity from old stars f	Number of galaxies with $x_i = 1$	Number of galaxies with $x_i = 0$
MW	IRAC4	0.950 ± 0.006	0.512 ± 0.102	35	1
MW	MIPS24	0.775 ± 0.050	0.081 ± 0.013	2	9
MW	MIPS70	0.512 ± 0.076	0.031 ± 0.012	2	25
MW	MIPS160	0.803 ± 0.029	0.155 ± 0.029	4	1
SMC Bar	IRAC4	0.887 ± 0.021	0.410 ± 0.083	16	1
SMC Bar	MIPS24	0.954 ± 0.005	0.061 ± 0.008	1	1
SMC Bar	MIPS70	0.945 ± 0.008	0.028 ± 0.009	2	1
SMC Bar	MIPS160	0.969 ± 0.003	0.128 ± 0.022	4	1

MIPS70 and MIPS160 bands in Tables 2.3-2.5. Again, τ_v= 1 and 10 kpc radius are used. The fractions are shown here as the average plus or minus the standard deviation. The number of galaxies with out-of-range x_i in each sample is given in columns 4 and 5. They are adjusted to $x_i = 0$ or 1 as explained above.

While the fraction of old stars x can exceed 90% (as in some of the calculation for models with SMC Bar dust), the fraction of the luminosity produced by old stars, f, is much lower; it is generally lower than 20%, with the exception of the IRAC4 band for the LVL galaxies. Although f is high for LVL/IRAC4, the remaining bands in the LVL sample yield lower values of f, consistent with the other two galaxy samples. If we take the LVL/IRAC4 combination out of the picture and restrict our results to SMC Bar dust, the highest value of f is 22.0%. Or, if we use 10 (100) Myr old stars instead of 1 Myr old stars as the younger population, the highest fraction becomes 27.9% (25.2%), again with MW/IRAC4/SINGS. On the other hand, if we keep the 1 Myr old stars but change the older population to 1 Gyr old stars, the highest fraction becomes 42.8%.

The fraction of luminosity f is generally higher for MW type dust, but the choice of dust does not affect our conclusion that dust emission is dominated by young stars. It is remarkable that the values of f computed from the MIPS luminosities are similar for both types of dust even when the fractions of old stars x is consistently higher for SMC Bar type dust (this is generally true for different stellar ages as well). This could be attributed to the steeper far-UV rise in the SMC Bar extinction curve; for

the same value of τ_v, the SMC Bar type dust is more effective in absorbing far-UV photons, and therefore requires fewer young stars to produce the same IR luminosity. The higher number of galaxies with $x_i = 0$ for MW type dust can be understood by looking at Figure 2.5; the MW 1 Myr old line is below a significant number of galaxies.

If we do a more complex study to include more than two stellar ages in this analysis, the fraction f will only be lower. We assume a linear contribution from the 2 stellar populations, which is not necessarily accurate because the effect of dust temperature on dust emission is non-linear. The more well-mixed the young and old stars are, the more non-linear their contribution will be. However, as older stars release many fewer UV photons compared to younger stars, it is almost certain that increasing the fraction of old stars would decrease the far-IR/IRAC1 ratios. Therefore, the far-IR/IRAC1 ratios are monotonically decreasing functions of the fraction of old stars (when all other parameters are fixed). Real stellar populations include a wide range of stellar ages, and with our analysis we can see whether such populations are closer to the “old" population or the “young" population. While this simple analysis cannot tell us what the best stellar age for the observed galaxies is, and the calculated fraction of old stars may suffer from non-linear effects, it is evident that dust emission is dominated by young stars.

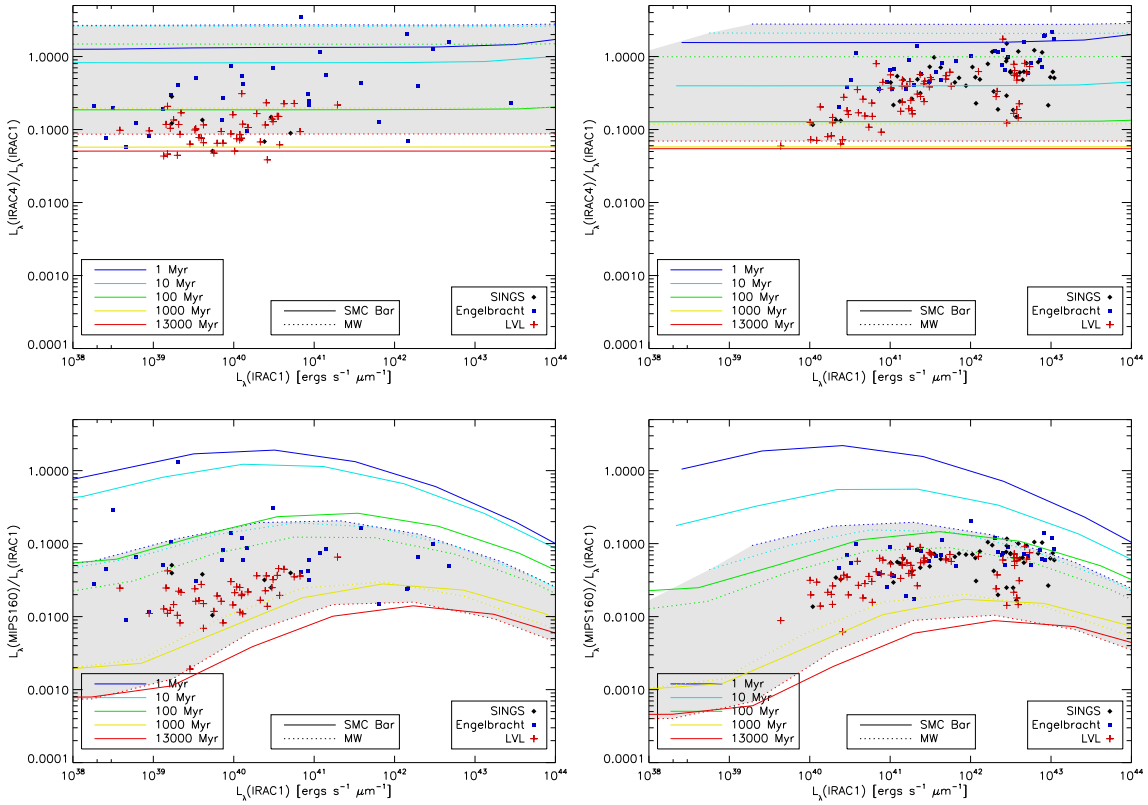

Figure 2.8: Plots to illustrate the effect of metallicity. The top (bottom) two figures are IRAC4/IRAC1 (MIPS160/IRAC1) luminosity ratio vs IRAC1 luminosity plots. Galaxies with metallicity lower than 8.1 are plotted with 1/5 solar metallicity models on the left, while the high metallicity galaxies are plotted with solar metallicity models on the right.

2.3.6 Metallicity

In stars with high metallicity, absorption lines form a continuum that leads to the production of a soft UV radiation field. This stellar atmosphere effect is known as "line blanketing". In contrast, stars with lower metallicity produce a harder radiation field. Empirically, metallicity correlates with the amount of dust (and therefore a low metallicity is often associated with a high gas-to-dust ratio). In the previous sections, we use a fixed (solar) metallicity for our models. However, the combination of a harder radiation field and a lower optical depth may give different results.

Metallicity has a somewhat phase-transition like effect. For the relatively high metallicities observed in the LMC and the Milky Way, observables are qualitatively similar. However, when we go to the low metallicity found in SMC, we find qualitatively different results, such as the lack of aromatic emission. For example, Engelbracht et al. (2005) found an abrupt change in the 8-to-24 μm color at around 1/4 solar metallicity. Calzetti et al. (2010) choose a metallicity of $\log(O/H) = 8.1$ as a rough dividing line for the two behaviors. We use the same value to divide our sample into two groups: the high metallicity galaxies with metallicity higher than 8.1, and the low metallicity galaxies with metallicity lower than 8.1.

In Fig. 2.8, we compare the high metallicity galaxies with the low metallicity ones. We plot the high metallicity galaxies with solar metallicity models (as in Fig. 2.5), but 1/5 solar metallicity models for the low metallicity galaxies. The low metallicity sample has lower luminosity ratios in both IRAC4 and MIPS160 bands, showing

that metallicity does have an effect on dust heating. They also have lower IRAC1 luminosity on average, consistent with the view that the big luminous galaxies are more evolved and have more metals, while the less luminous galaxies have relatively more young stars and lower metallicity. Calculations of the fraction of luminosity from old stars (f) shows that the results for the MIPS bands are qualitatively the same for the two metallicity groups; but for the IRAC4 band, f of the low metallicity group can be as high as two times that of the high metallicity group. For SINGS and LVL, f of the low metallicity group is higher than 0.5 for IRAC4. It suggests that the non-starburst, low metallicity galaxies may have lower PAH abundance than our dust model. Since there is no significant trend in the MIPS bands, metallicity does not affect our main conclusion.

2.3.7 Sub-mm predictions

The Herschel Space Observatory was recently launched in May 2009. The far infrared imaging camera of the Spectral and Photometric Imaging Receiver (SPIRE) has 3 photometric bands centered at 250, 350 and 500 μm. In addition, the Photodetector Array Camera and Spectrometer (PACS) has a photometric band at 100 μm that MIPS does not have. It is interesting to see, from a model point of view, the contribution of luminosity of old stars at these wavelengths.

Table 2.6 shows the fraction of luminosity (f) due to old stars at 100, 250, 350 and 500 μm, calculated with Equation 2.4. For the ith galaxy, we use the fraction of

Table 2.6: Fractions of luminosity due to old stars at 100, 250, 350, and 500 μm.

Data Sample	Dust Type	$f(100\mu\text{m})$	$f(250\mu\text{m})$	$f(350\mu\text{m})$	$f(500\mu\text{m})$
Engelbracht	MW	0.046 ± 0.006	0.136 ± 0.028	0.176 ± 0.036	0.213 ± 0.044
Engelbracht	SMC Bar	0.032 ± 0.001	0.227 ± 0.028	0.349 ± 0.039	0.463 ± 0.044
SINGS	MW	0.129 ± 0.059	0.237 ± 0.067	0.277 ± 0.072	0.308 ± 0.077
SINGS	SMC Bar	0.111 ± 0.052	0.355 ± 0.053	0.477 ± 0.049	0.572 ± 0.045
LVL	MW	0.105 ± 0.025	0.311 ± 0.037	0.397 ± 0.040	0.463 ± 0.042
LVL	SMC Bar	0.068 ± 0.021	0.375 ± 0.029	0.566 ± 0.025	0.706 ± 0.020

old stars (x_i) calculated with Equation 2.2 for MIPS160 and the luminosity from the corresponding old (O_i) and young models (Y_i) to estimate f_i. The denominator is the estimated luminosity at the SPIRE wavelengths, and the numerator is the luminosity due to old stars only.

$$f_i(\lambda) = \frac{x_i(160\mu\text{m})O_i(\lambda)}{x_i(160\mu\text{m})O_i(\lambda) + (1 - x_i(160\mu\text{m}))Y_i(\lambda)} \tag{2.4}$$

We convolve our model SEDs with the relative spectral response functions of the SPIRE bands (SPIRE Observers' Manual, 2010) and the PACS 100 μm band (PACS Observer's Manual, 2010) to compute the band integrated luminosity. We calculate the average and standard deviation for each combination of data sample (SINGS, Engelbracht and LVL) and model dust type (MW, SMC bar). We choose MIPS160 for the estimation of x because it is the longest wavelength in this study. As we go from 100 μm to 500 μm, f increases, showing that old stars are increasing in

importance at longer wavelengths.

Moreover, f in general has an increasing trend from the Engelbracht to the SINGS and the LVL sample. We have similar trends in some of the other bands but the trend in the SPIRE bands is much clearer, especially in the longest wavelength. This shows the order of the importance of the old stars in the 250-500 μm regime for the three catalogs. It is easy to understand the lower f in the starburst sample as it has more recent star formation activity. So for starburst galaxies, young stars still contribute more luminosity in the sub-mm range (up to 500 μm) compared to old stars. The difference between f of LVL and f of SINGS is likely due to a combination of their stellar populations, galaxy type and composition. We will continue to explore this wavelength regime and have a better understanding when Herschel data is available.

2.4 Conclusion

Using our dusty radiative transfer model, together with IRAC and MIPS observations on the SINGS galaxies, the starburst galaxies in Engelbracht et al. (2008) and the LVL galaxies, we have studied the effect of stellar age on infrared luminosity. We found that MW type dust tends to produce too little infrared luminosity for some of the galaxies (especially for the starburst galaxies), and so SMC Bar type dust is a more appropriate choice. However, we also note that we have similar results with both types of dusts when we calculate the luminosity due to old stars.

From an analysis of the IRAC4/IRAC1 and MIPS160/IRAC1 luminosity ratios vs IRAC1 luminosity plots, we found that the observed luminosity cannot be produced by 13 Gyr old stellar populations alone. The stellar age that dominates dust heating is on the order of 100 Myr. However, a small number of galaxies - the elliptical galaxies - did not fit well into our analysis. Their lower far-IR to IRAC1 ratios could be attributed to their deficiency of dust.

We found that the models are more sensitive to changes in parameters (such as stellar age, radius and optical depth) in the far-IR bands compared to the mid-IR bands. This can be explained by the fact that non-equilibrium emission dominates mid-IR, but is mostly negligible in far-IR. When non-equilibrium emission dominates, the luminosity ratio is less dependent on dust temperature and is therefore less affected by changes in the radius and stellar mass; it is also less sensitive to optical depth τ_v because the extinction for highly energetic photons saturates.

With the simplistic assumption that the observed galaxies are composed of two stellar populations of different ages, we found that the fraction of far-IR luminosity from 13 Gyr old stars is generally less than 20%. The result does not depend on the metallicity. Therefore, cold does not necessarily mean old; our study shows that far-IR radiation is dominated by a small number of younger stars.

In the next chapter, we introduce a large grid of dusty radiation models and spectral evolutionary synthesis models. With the model grid we will attempt to further confirm this study by fitting each galaxy individually and derive properties

such as stellar age. We will compare the statistics of the resultant properties to the results in this paper and explain any differences or new features observed.

Chapter 3

DirtyGrid I: 3D dust radiative transfer modeling of spectral energy distributions of dusty stellar populations

Abstract

Understanding the properties of stellar populations and interstellar dust have important implications for galaxy evolution. In normal star forming galaxies, stars and the interstellar medium dominate the radiation from ultraviolet (UV) to infrared (IR). In particular, interstellar dust absorbs and scatters UV and optical light re-emitting the absorbed energy in the IR. This is a strongly non-linear process that makes independent studies of the UV-optical and IR susceptible to large uncertainties and degeneracies. Over the years, UV to IR spectral energy distribution (SED) fitting utilizing varying approximations has revealed important results on the stellar and dust properties of galaxies. Yet the approximations limit the fidelity of the derived properties. There is sufficient computer power now available that it is now possible to remove these approximations and map out of landscape of galaxy SEDs using full dust radiative transfer. This improves upon previous work by directly connecting the UV, optical and IR through dust grain physics. We present the DirtyGrid, a grid of radiative transfer models of SEDs of dusty stellar populations in galactic environments designed to span the full range of physical parameters of galaxies. Us-

ing the stellar and gas radiation input from the stellar population synthesis model PEGASE, our radiative transfer model DIRTY self-consistently computes the UV to far-IR/sub-mm SEDs for each set of parameters in our grid. DIRTY computes the dust absorption, scattering, and emission from the local radiation field and a dust grain model, thereby physically connecting the UV-optical to the IR. We describe the computational method and explain the choices of parameters in DirtyGrid. The computation took millions of CPU hours on supercomputers and the SEDs produced are an invaluable tool for fitting multi-wavelength datasets. We provide the complete set of SEDs in an online table.

3.1 Introduction

The ultraviolet (UV), optical, and infrared (IR) emission of a galaxy reflects the underlying populations and distributions of stars, gas, and dust, excluding any contributions from an active galactic nucleus (AGN). The detailed shape of a galaxy's integrated spectral energy distribution (SED) contains information about both the stellar populations (e.g., total stellar mass, stellar mass-to-light ratio, star formation history, and metallicity) and the interstellar medium (e.g., total dust mass, grain composition, and size distribution). These quantities probe the stars themselves and the fuel for star formation and, thus, are crucial to understanding galaxy formation and evolution. While integrated SEDs do not provide measurements for spectral indices or equivalent widths of absorption and emission features, when compared to high resolution spectra they are much easier to obtain, and hence enable studies on large scale surveys of galaxies both locally and at a range of redshifts.

Modeling of the intrinsic stellar spectra starts from the initial mass function (IMF), which describes the distribution of newly formed stars and is generally based on power laws with adjustments at the very high and low mass limits (e.g., Salpeter, 1955; Kroupa, 2001). Combined with stellar evolutionary tracks and stellar spectra, Tinsley (1968) and many others created stellar population synthesis models to compute the detailed spectra of single stellar populations. Charlot & Bruzual (1991) developed an isochrone synthesis method that solved the problems in modeling fast evolutionary phases caused by sparsely sampled stellar evolutionary tracks. Padova isochrones

(Bertelli et al., 1994) include a wide range of stellar ages and metallicities and they cover most of the important evolutionary phases including the thermally pulsing regime of the asymptotic giant branch.

The composition of interstellar dust grains has been inferred based on their extinction and emission. The three major dust components present in the diffuse interstellar medium (ISM) of the Milky Way include silicate, carbonaceous, and polycyclic aromatic hydrocarbons (PAH) grains. The major dust extinction features are the 2175 Å absorption feature identified as due to small graphite grains (Stecher & Donn, 1965) and the absorption features at 9.7 and 18 μm that are attributed to silicate grains (Willner, 1976; McCarthy et al., 1980b). The mid-infrared aromatic features found between 3 and 18 μm are associated with PAH grains (Leger & Puget, 1984; Allamandola et al., 1985). The bulk of the dust emission is seen in the far-infrared and well modeled by large silicate and carbonaceous grains (Desert et al., 1990; Li & Draine, 2001).

The presence of dust grains significantly alters the UV-optical spectra of galaxies by absorbing and scattering photons. The wavelength dependence of these effects along a single sightline towards a star is characterized by an extinction curve. The major features of the dust extinction curve are a general increase in extinction with decreasing wavelength, the far-UV rise, and the aforementioned 2175 Å bump. Although the strength of these features varies along different sightlines, Cardelli et al. (1989) found that the average extinction curve in both diffuse and dense regions of the

Milky Way can be described by an extinction law that depends on only one parameter, $R(V) = A(V)/E(B-V)$. The standard method to determine extinction curves is the "pair method", which takes advantage of the fact that the intrinsic spectra of a reddened star (one that suffers from dust extinction) and an unreddened star of the same spectral type should be the same (Bless & Savage, 1970). However, extinction curves only apply to the simple geometry of a star observed through a screen of dust. Galaxies have more complex geometries where the effects of mixing the stars, gas, and dust must be taken into account. The inclusion of dust radiative transfer effects (e.g., different stars seeing different dust optical depths and scattered photons included in the measurement) changes the effects of dust from the geometry invariant extinction curve to that of an attenuation curve with a shape that is dependent not only on the properties of the dust grains, but also the relative distributions of stars, gas, and dust.

The energy absorbed by dust grains in the UV-optical is primarily emitted in the IR. In the simplest case, the far-IR dust emission spectrum resembles a modified blackbody with an emissivity β that may vary depending on composition and environment (e.g., Lis et al. 1998). Schlegel et al. (1998) found that the temperature of the far-IR dust emission in the Milky Way is on the order of 20 K, which corresponds to a peak of emission around 150 μm. While the far-IR dust emission can be modeled as modified blackbody emission with a single temperature, the mid-IR emission is more complicated to calculate as the dust emission in this wavelength range is dominated

by stochastically heated dust grains (Leger & Puget, 1984). Stochastic heating is also known as transient or non-equilibrium heating.

SED fitting is a widely used method to recover stellar, gas, and dust properties of star forming regions and galaxies. Thanks to various space missions such as the Galaxy Evolution Explorer (*GALEX*, Martin et al., 2005) in the UV, the Spitzer Space Telescope (*Spitzer*, Werner et al., 2004) in the mid- to far-IR, and the Herschel Space Observatory (*Herschel*, Pilbratt et al., 2010) in the sub-mm, we have high quality photometric data in the wavelength ranges that are crucial to SED fitting but not observable on Earth due to the opaque atmosphere. Combined with ground based optical and near-IR data such as those from the Sloan Digital Sky Survey (SDSS, Gunn et al., 2006) and Two Micron All Sky Survey (2MASS, Skrutskie et al., 2006), respectively, we have an abundance of well sampled UV to IR/sub-mm SEDs of star forming galaxies.

The wealth of UV to far-IR SEDs of galaxies has been used in many studies to investigate the properties of galaxies. Calzetti et al. (2000) fit the far-IR SEDs of 8 local starburst galaxies with two modified blackbody functions and found that cool dust contributes up to 60% of the total far-IR emission and is up to 150 times more massive than warm dust. By fitting the UV-optical SEDs of ~50,000 optically selected local galaxies to a library of dust-attenuated population synthesis models, Salim et al. (2007) obtained dust-corrected SFRs of these galaxies and calibrated a simple prescription to obtain such SFRs with only *GALEX* far-UV and near-UV data.

Erb et al. (2006) fit the observed 0.3–8 μm SEDs of 87 rest-frame UV-selected star-forming galaxies at $z \approx 2$ to Bruzual & Charlot (2003) population synthesis models and the Calzetti et al. (2000) extinction law, and found that metallicity monotonically increases with the derived stellar mass.

Dusty SED fitting in the literature generally falls into 3 categories, (1) UV-optical SED fitting (e.g., Salim et al. 2007, (2) infrared SED fitting (e.g., Draine et al. 2007), and (3) full UV to infrared SED fitting with the UV-optical and infrared connected in simple ways (e.g., Noll et al. 2009a). Fitting UV and optical observations alone results in significant degeneracy between the age of the stellar population and the amount of dust present. Fitting the IR observations alone results in knowledge of the IR properties of dust grains, but very little about the underlying stellar populations or UV dust properties. Due to the non-linear interaction between dust and the radiation field, a complete solution to the full UV to infrared SED requires 3D dust radiative transfer, which is computationally intensive. By requiring that the absorbed energy in the UV-optical equals the energy emitted in the infrared, one can connect the UV-optical to the infrared without doing radiative transfer. While to zeroth order correct, such a simple method does allow models that can violate dust physics in that the detailed IR dust emission SED is not dependent on the wavelength dependence of dust absorption and the dust grain properties, but only on the integrated dust absorption.

A more powerful but historically impractical way is to fit the full UV to infrared

SED with the UV-optical and infrared connected by dust radiative transfer physics. Galaxies have complicated global and local 3D geometries of stars and dust and these geometries strongly influence the dust radiative transfer solution (Witt et al., 1992b; Witt & Gordon, 1996, 2000). Such 3D dust radiative transfer has no analytic solution (Steinacker et al., 2013). With advances in computer performance and the availability of supercomputing clusters dedicated for science, a large scale computation to map out the SED landscape with radiative transfer has become possible. Variations in stellar and dust properties cause simultaneous changes in the UV-optical and infrared SED. Full radiative transfer solutions allow us to use the full information content of the SEDs to constrain the model of a galaxy. Information carried in each part of the SED is complementary with the other part, and by simultaneously solving for both we can break degeneracies in stellar and dust parameters.

We present the DirtyGrid in this paper. DirtyGrid is a grid of UV to IR SEDs built from a combined dust radiative transfer and stellar population synthesis model. To capture to whole SED landscape, the grid spans a large range of eight parameters: stellar age, metallicity, stellar surface density, star formation type, amount of dust, global geometry, dust clumpiness, and grain type. We describe the underlying models used to build DirtyGrid, explain the choice of parameters, and present the resultant SEDs. In a companion paper, we use the DirtyGrid to study dust properties in nearby galaxies and test various star formation rate indicators commonly used in the literature.

3.2 Models

The DirtyGrid is a set of model SEDs of stellar populations with dust and gas, distributed in a 8-dimensional parameter space. For computational purpose, the parameter space is discretized into a grid, and it is customary to call DirtyGrid a grid of models. At each grid point, the SED is either (1) constructed using the DIRTY radiative transfer model (Gordon et al., 2001; Misselt et al., 2001), or (2) interpolated from nearby grid points constructed using DIRTY, in order to conserve computations when the change in the SED is small. Figure 2.1 shows an example DirtyGrid SED. The grid of models is designed to span the possible range of stellar, dust, and geometric parameters of stellar populations in galactic environments. Under the assumption that the UV-IR SEDs of normal star forming galaxies are dominated by one or a few types of characteristic star forming regions unique to each galaxy, we can use combinations of models in the grid to fit whole galaxies. In this section, we describe the DIRTY radiative transfer model and the inputs that define the parameter space covered by the DirtyGrid models.

3.2.1 Radiative transfer

Due to the ability of dust to absorb, scatter, and re-emit radiation, deriving the global SED of a stellar population mixed with interstellar dust is a radiative transfer problem. Analytically, the three-dimensional (3D) radiative transfer problem can be

represented by an integral-differential equation (Steinacker et al., 2013). However, in the general case, this equation has no analytical solution. We use DIRTY, a 3D Monte Carlo model to compute the radiative transfer of stellar, gas, and dust emission through a dusty medium. DIRTYv1 is described in detail in Gordon et al. (2001) and Misselt et al. (2001). The current version of the code (DIRTYv2) is based on the algorithms in DIRTYv1, but with the addition of a full dust grain model, a tighter integration of the dust radiative transfer and emission calculations, improved robustness of the input/output, and the enhancement of continuous photon absorption to accelerate the calculations. Here we provide a summary of DIRTY and detail the new features in the current version. Readers interested in the radiative transfer details should refer to the original DIRTY papers and Steinacker et al. (2013).

A single run of a DIRTY model requires 3 inputs: 1) the energy sources, 2) the physical properties of the absorptive medium (e.g., the dust grain physics), and 3) the relative distribution of both dust and stars: the model geometry. In the context of a DIRTY model, "geometry" refers to both the relative distribution of sources and dust throughout the model space (global geometry) as well as the clumpiness of the dust distribution (local geometry). By construction, in DIRTY all three ingredients may be arbitrarily specified. In general, the inputs are specified based on the physical problem at hand. While the local geometry can be of arbitrary complexity—e.g., independent dust densities at each point in the model space—it is convenient to specify the local distribution of dust ("clumpiness") by a two phase medium characterized by the filling

factor of high density regions embedded in a uniform medium and the density ratio between the high density regions and the uniform medium (Witt & Gordon, 1996).

DIRTY has two main components: a radiative transfer routine and a dust emission routine. Given a distribution of emission sources within an absorptive medium, the purpose of the radiative transfer routine is to calculate the distribution of absorbed and escaped fluxes according to the physics of the interaction between photons and dust grains and the relative distribution between the sources and the dust. The same radiative transfer routine is used for both primary emission (from stars and gas) and secondary emission (from dust). The dust emission routine calculates the emission spectrum from the absorption spectrum according to the physics of dust heating and cooling. The fact that dust emission can be re-absorbed by dust during radiative transfer introduces a circular dependency between the dust absorption and emission spectra, so DIRTY takes an iterative approach to obtain a self-consistent solution. The iterative procedure is illustrated in Figure 3.1. This contrasts with the simpler way of modeling dust heating with a radiation field scaled from observations in the solar neighborhood (e.g., Draine et al. 2007).

The DIRTY radiative transfer algorithm utilizes a weighted Monte Carlo approach with absorption-scattering split, forced first scattering, the peel-off technique, and continuous absorption. We use a Cartesian local mean intensity storage grid to discretize the model geometry into regions of constant optical depth and radiation field. Steinacker et al. (2013) reviewed 3D dust radiative transfer techniques in general (not

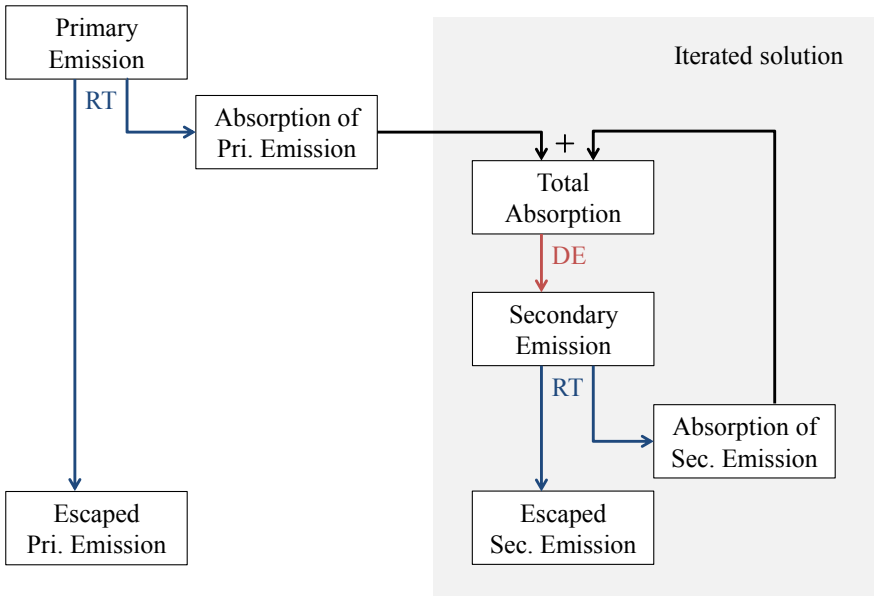

Figure 3.1: Iterative procedure used in DIRTY to achieve a self-consistent radiative transfer solution. Primary emission refers to emission from stars and gas; secondary emission refers to emission from dust. The radiative transfer and dust emission routine are denoted as RT and DE respectively. The procedure in the shaded area is repeated until convergence is achieved, after which we combine escaped primary and secondary emissions to obtain the final SED.

specific to DIRTY) and devoted a section to each of the performance enhancing techniques we list above. For the same level of accuracy achieved, these techniques allow us to reduce the amount of computation required, which is critical for a large scale project like the DirtyGrid. Alternatively, for the same amount of computation, one could use these techniques to enhance the accuracy of the results.

In the weighted Monte Carlo approach, instead of following individual photons as discrete particles, we assign weights to photon packets and keep track of the changes in the weights due to interaction events. We trace the trajectory of a photon packet and determine the distance traveled according a random number sampled from a probability distribution based on the optical depth in the path. At each interaction site, we split the weight of the photon packet into an absorbed portion and a scattered fraction according to the dust albedo (the absorption-scattering split). The direction of scattering is determined from a scattering phase function. Instead of depositing the entire absorbed portion at the interaction site, we distribute the energy along the path. This is known as continuous absorption and is new to DIRTYv2. In addition, we allow the photon packet to contribute to the escaped flux at each interaction site to improve the spatial sampling (the peel-off technique). In low optical depth models, a large number of photon packets may exit the model geometry without any interactions. To avoid "wasting" photon packets, we force the first scattering so that all of them contribute to the absorbed and scattered fluxes, and we correct for the bias in probability by adjusting the weights.

For a fixed number of interaction events, continuous absorption greatly improves the sampling of the radiation field while keeping the sampling of scattering the same. However, this calculation is relatively expensive. Each of the many additional exponential functions required for this technique consumes tens of clock cycles in processors typically found on supercomputers nowadays (i.e. x86-64). As a result, for a fixed amount of computation, this technique improves the determination of the local radiation field but worsens the sampling of scattering. In other words, it shifts the computational balance to focus more on populating the radiation field. For the parameter space covered by the DirtyGrid, this is beneficial because usually the scattered fluxes are better populated than the radiation field, and stochastic heating of dust grains is very sensitive to noise in the radiation field. Conversely, continuous absorption may not be suitable for models of extremely high optical depth or models that only calculates equilibrium emission of dust grains.

We repeat the radiative transfer for a number of photon packets until the Monte Carlo uncertainty in the direct and scattered fluxes is below a desired limit (0.5–1.0% depending on the geometry), or until the maximum limit of 10 million photon packets per wavelength has been reached. We then repeat the process for all the wavelengths in a non-uniform wavelength grid covering the range from 0.0912 to 1000 μm. The non-uniform grid has higher resolution around 10 μm to resolve PAH features, and lower resolution at the longest wavelengths (where the spectrum is smooth) to avoid unnecessary computation.

3.2.2 Stellar populations

Since DIRTYGrid is intended to provide a grid of integrated galactic SEDs over a large range of properties, the sources for the radiative transfer model are stellar population models. Stellar population models calculate the integrated SEDs of stellar populations optionally including the emission due to ionized gas. These SEDs determine the amount and the wavelength dependence of primary emission in the context of radiative transfer. Examples of stellar population models in the literature include PEGASE.2 (Fioc & Rocca-Volmerange, 1997, 1999), Starburst99 (Leitherer et al., 1999), GALAXEV (Bruzual & Charlot, 2003), and FSPS (Conroy et al., 2009). We select PEGASE.2 (hereafter PEGASE) for the DIRTYGrid due to its ability to model both young and old stars well, its flexibility, and our previous experience in using it with DIRTY. For example, Gordon et al. (1999) have used PEGASE with DIRTY to model the dusty starburst nucleus of M33. In the DIRTYGrid, we vary four of the parameters of the stellar population model: the age of the stellar population and its formation history, the metalilicity, and the SED scaling factor. Figure 3.2 shows example of PEGASE SEDs.

PEGASE uses the isochrone synthesis method, which integrates an IMF, evolutionary tracks, and a library of stellar spectra, to produce the integrated SEDs of a stellar population. In a single star formation event, the IMF describes the relative abundance of newly formed stars of different masses. We used the Salpeter (1955) IMF from 0.1 to 120 $M_{\odot}$. Kroupa (2001) has found variation in the initial mass

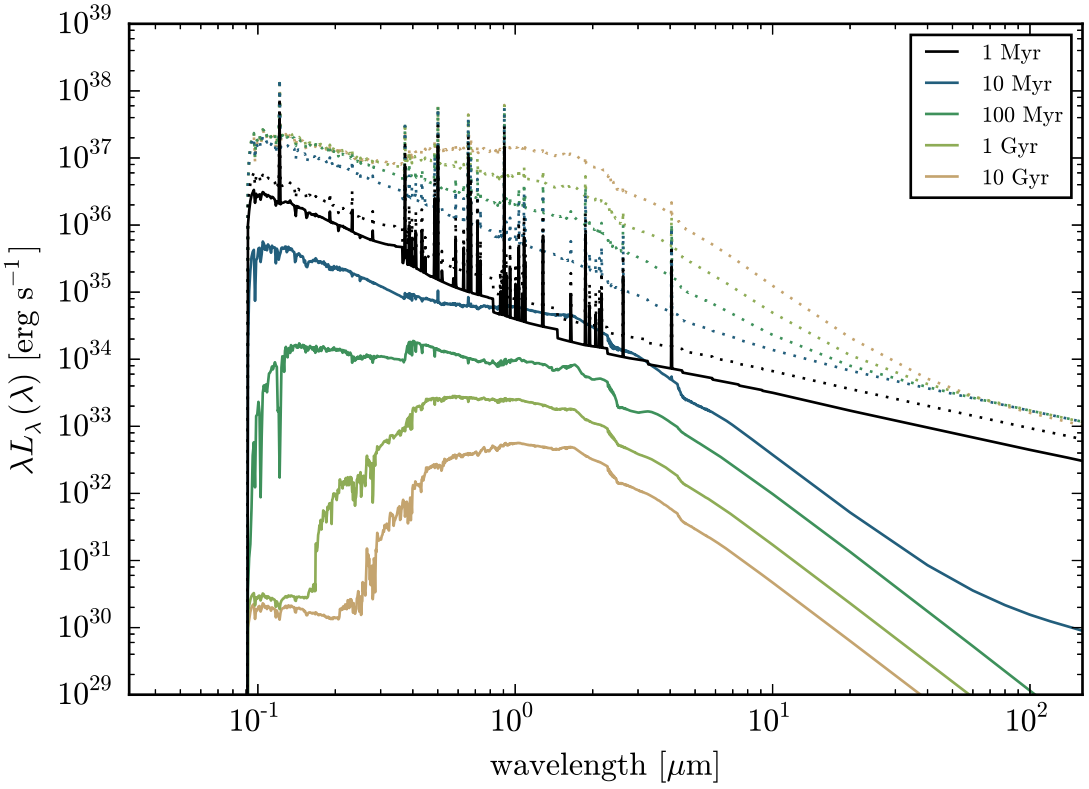

Figure 3.2: Stellar and gas emission spectra generated by stellar population model PEGASE. The solid lines show models with instantaneous star formation (with decreasing luminosity as age increases), while the dotted lines show models with constant star formation (with increasing luminosity as age increases). Here we normalize the instantaneous star formation models to $1M_\odot$ and constant star formation models to $1M_\odot$/Myr. These models use solar metallicity and have nebula emission and emission lines added.

functions between globular clusters and the Galactic-field, but it is uncertain how or whether the IMF change in different environments and redshifts. Adopting a cutoff in the low mass range of the IMF can lead to a factor of ~1.5 change in the star formation rate determined from empirical SFR indicators (Kennicutt & Evans, 2012).

The evolutionary tracks describe the trajectory of stars in the Hertzsprung-Russell diagram. PEGASE mainly uses tracks from the Padova group, but they also supplemented the Padova tracks in a number of special evolutionary phases. Most importantly, they use the equations in Groenewegen & de Jong (1993) to create pseudo-tracks for the thermally pulsing asymptotic giant branch (TP-AGB) stars, which are short-lived but luminous.

In general, the star formation rate of a galaxy is a function of time. The typical timescale for gas depletion is about 3 Gyr (Pflamm-Altenburg & Kroupa, 2009), so it is reasonable to expect the star formation rate to decrease over time. The time-dependent profile of star formation can be modeled as an exponentially decaying burst (Searle et al., 1973; Conti et al., 2003). However, given limited computational resources, we choose to model only the following two extreme cases: instantaneous burst and constant star formation, which correspond to time constants of infinity and zero, respectively. These two cases bracket the possible real world scenarios. For example, the fraction of young stars in an exponentially decaying star formation model is lower than that of a constant star formation model, and higher than an instantaneous burst model, for any finite decaying time constants. Our choice reduces

the "star formation history" dimension of our parameter grid to only two points. With further increase in the capability of supercomputers and more data to constrain the parameter space, we may include exponentially decaying star formation into a future version of DirtyGrid, potentially increasing the number of points in the "star formation history" dimension by an order of magnitude.

Closely related to the star formation history is the age of the stellar population. The age of the stellar population reflects the time elapsed since the "instantaneous" burst of start formation in the case of a burst model, or the time over which the model has been forming stars at a constant rate. To cover a range of plausible ages for the stellar populations, the DirtyGrid includes both burst and constant stellar populations with ages between 1 Myr and 13 Gyr.

The integrated SED of a stellar population depends on the initial metallicity of the stellar population. Populations with different metallicity trace different evolutionary tracks and populate different isochrones. Hence population synthesis models, including PEGASE, also specify the metallicity of the stellar population. To cover a realistic range of integrated galactic metallicities, in DirtyGrid we compute SEDs for stellar populations spanning a range of metallicities between Z of 0.0001 and 0.1.

To control the intensity of stellar emission, we scale the input SED by the stellar surface density. For instantaneous star formation (ISR) models, the scaling factor is the stellar mass surface density σ_M. For constant star formation (CSR) models, the scaling factor is the star formation rate surface density $\sigma_{\rm SFR}$. The total mass of stars

formed in CSR models is the product of $\sigma_{\rm SFR}$ and the age of the stellar population. In both cases, the final stellar mass depends on the evolution of the stellar population, which is an output of PEGASE, and due to the finite life time of stars, is always smaller than the total mass of stars formed. We choose the range of stellar mass or SFR by comparing the model outputs to SINGS (Kennicutt et al., 2003) and LVL galaxies (Dale et al., 2009) and star formation regions in very nearby galaxies. The range we use covers the range derived empirically from these observations.

DIRTY does not calculate the radiative transfer through gas, which would add significant complexity to the code. The effect of gas, which is particular important for young stellar populations due to the significant UV radiation, is approximated by a gaseous nebula that is local to the stars and optically thick in the Lyman lines. Under extremely intense UV radiation, the absorption rate of Lyman continuum photons by gas is limited by the number of neutral hydrogen atoms, so some of these photons should be absorbed by dust instead. In contrast, in our models these photons are always absorbed by gas. The difference is negligible in typical H II regions (Walcher et al., 2011). We add the gas continuum and recombination lines emission, as calculated by PEGASE, to the stellar emission.

The combined spectrum at a given age, star formation history, metallicity, and intensity defines the radiation sources used as input for the DIRTY radiative transfer model.

3.2.3 Dust

The dusty medium through which source photons propagate in a radiative transfer simulation has a profound effect on the output spectrum of the simulation. The optical depth, albedo, and scattering phase function of the dust determines the probability that a photon will interact, as well as the amount of the source energy that is absorbed or scattered. Once absorbed, the radiation is thermalized and re-emitted according to the emission cross sections of the dust population, producing a dust emission spectrum.

To integrate the dust population into the radiative transfer simulation, a dust grain model is required. A dust model specifies the composition, size distribution, and micro-physics (e.g., the optical properties) of the dust grain population. Since the DirtyGrid is designed to provide a grid of SEDs representative of the integrated SED of galaxies over a wide range of galactic parameters, the dust inputs must reflect the range of dust characteristics observed in galaxies. Therefore, with DirtyGrid, we adopt the dust grain models described in Weingartner & Draine (2001), who used an analytical expression to parametrize the size distributions of "astronomical" carbonaceous and silicate grains. They fit the extinction curves of sightlines in Milky Way (MW), Large Magellanic Cloud (LMC), and Small Magellanic Cloud (SMC) to produce sets of best-fit parameters of the size distributions. For the MW, we pick the $R_V = 3.1$, $b_C = 6.0 \times 10^5$ model; for LMC, we choose the $b_C = 1.0 \times 10^5$ model of the "LMC 2" environment (Meaburn 1980; Misselt et al. 1999, the supergiant shell on the

southeast side of 30 Dor); for SMC we take the model of the "SMC bar" environment (Gordon & Clayton, 1998), which is the only model presented for the SMC. The grains are spherical and their radii range from 3.5 Å to 2.5 μm. The spherical grain approximation enables the use of Mie theory to compute the optical scattering and absorption cross sections. At the smallest (largest) size, the carbonaceous grains are PAH grains (graphite grains), and at intermediate sizes the optical properties are intermediate between the two. By including MW, LMC, and SMC dust grain models in the DirtyGrid, our SEDs represent the full range of dust properties that have been observed in galaxies. Figure 3.3 gives the extinction curves for the three different models of dust grains used in the DirtyGrid.

The radiative transfer routine in DIRTY calculates the total energy absorbed by dust in each of the grid cells in our local mean intensity storage grid. DIRTY then launches the dust emission routine to calculate the emission spectrum in each grid cell independently (and sequentially). For each species of dust grain (carbonaceous and silicate), starting at the smallest grain size, we calculate the stochastic heating of dust grains. The calculation of stochastic heating is computationally expensive, but various authors (e.g., Leger & Puget 1984) have shown that stochastic heating is needed to explain the near/mid-IR emission in excess of that expected from dust in pure thermal equilibrium in many astronomical systems. Using the method of Guhathakurta & Draine (1989), we populate a matrix with the probabilities of transitions between different internal energy states, each of which has an associated temperature. The

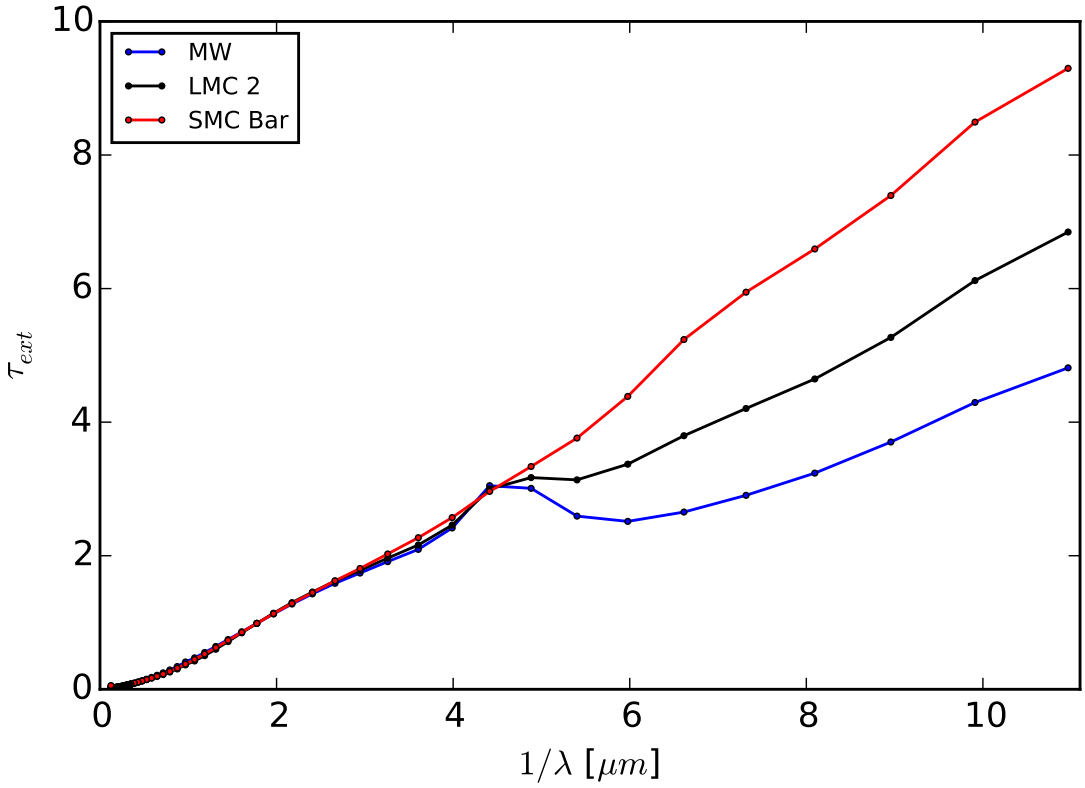

Figure 3.3: DIRTYGrid extinction curves for the MW, LMC 2 and SMC Bar dust models with $\tau_V = 1$. The primary differences between these curves are the strength of the 2175 Å feature and the far-UV rise. Our choice of dust types is intended to cover the range of dust properties observed in galaxies.

solution of the transition matrix gives us the probability of finding the dust grain in each of the states, $P(T)$. The emission at this particular grain size is an integration of the modified blackbody function (taking into account the effects of the changing emissivity across wavelengths) weighted by $P(T)$. As the calculation moves to grains of increasing sizes, we reach a regime in which the grains are in equilibrium with the radiation field and $P(T)$ becomes strongly peaked. At this point we switch over to the simpler equilibrium heating calculation, in which grains emit in a modified blackbody function with a single temperature. We find the equilibrium temperature, and therefore the equilibrium emission as a function of wavelengths, by simply balancing the energy absorbed and emitted by dust grains of this particular size. In the end, we sum over the emission from all grain sizes and species to obtain the total dust emission spectrum in the current grid cell. A rigorous discussion on dust modeling in DIRTY is available in Misselt et al. (2001). Recently, Camps et al. (2015) compared the dust emission algorithms of six radiative transfer codes including our latest code and found the all six codes consistent within 10%.

In addition to the physics that describes how photons will interact with dust and how the dust will respond to the input of energy, the total amount of dust in the model must be specified. Rather than directly specifying the mass of dust, in the DirtyGrid, the optical depth at V band (τ_v) is specified as an input parameter to DIRTY. τ_v is measured from the center of the model to the edge, averaged over all 4π steradians of solid angle. For normal disk galaxies, Holwerda et al. (2007) has

found that τ_v is on the order of unity. Dale et al. (2006) also found that the average attenuation is $A_{\rm V} \approx 1.0$, i.e. $\tau_{\rm V} \approx 0.92$, for a large portion of SINGS galaxies. In the DirtyGrid, the τ_v dimension in the parameter space span over two dex of optical depths from 0.1 to 10, which we believe is sufficient to cover the majority of observed galaxies.

3.2.4 Geometry

In the DIRTY model, the global geometry describes the relative distributions of dust and stars, while the local geometry determines the clumpiness of dust. Geometry has a profound effect on radiative transfer, both on the attenuation (e.g., by providing paths of different optical depths) and the emission (e.g., through the non-trivial spatial and temperature distribution of dust). While an extinction curve can be accurately measured by comparing the spectrum of a reddened and an unreddened star of the same spectral type (and has been done for sightlines in MW, LMC and SMC), in the complex geometries generally associated with galactic environments, only "attenuation" curves can be measured. A dust attenuation curve is defined as the wavelength dependence of attenuation by dust, including the effects of absorption, scattering out of the beam, and scattering into the beam, and is usually measured for regions of galaxies or whole galaxies. In contrast to the traditional extinction curve, determination of attenuation curves is more challenging because it is difficult to independently constrain the underlying stellar populations and radiative transfer

effects (anisotropic scattering, differential extinction between sources, dust exposed to different radiation field intensities, and dust clumpiness). Baes & Dejonghe (2001) found that scattering approximations such as isotropic scattering can be a major source of error in radiative transfer. Even in the absence of scattering, Disney et al. (1989) found that the choice of model geometry significantly affects attenuation.

Commonly used global geometries for radiative transfer modeling of galactic environments include plane-parallel slabs, spheres, double-exponentials, and arbitrary distributions (see Calzetti 2001 and references therein). Plane-parallel slabs are simplest to model, but Calzetti et al. (1994) found that such model does not agree with the UV-optical spectra of starburst galaxies, and they empirically calibrated a single attenuation curve of starburst galaxies as a third-degree polynomial in $1/\lambda$. To account for that fact that young stars are likely to be embedded in their birth cloud and therefore more attenuated then old stars, Silva et al. (1998) and Charlot & Fall (2000) created models that provide additional opacity around the young stars.

In the DIRTYGrid, we use the Cloudy, Dusty and Shell global geometries as defined by Witt & Gordon (2000). These geometries are spherically symmetric and efficient for radiative transfer. DIRTY supports arbitrary stellar and dust geometries, and we implement the dust geometries as spatially resolved blocks in our local mean intensity storage grid, which has a resolution of $30 \times 30 \times 30$. A visualization of the cross section of the geometries is shown in Figure 3.4. In the Cloudy geometry, stars are uniformly distributed in the sphere, and a dusty core is located within 0.69 times of the system

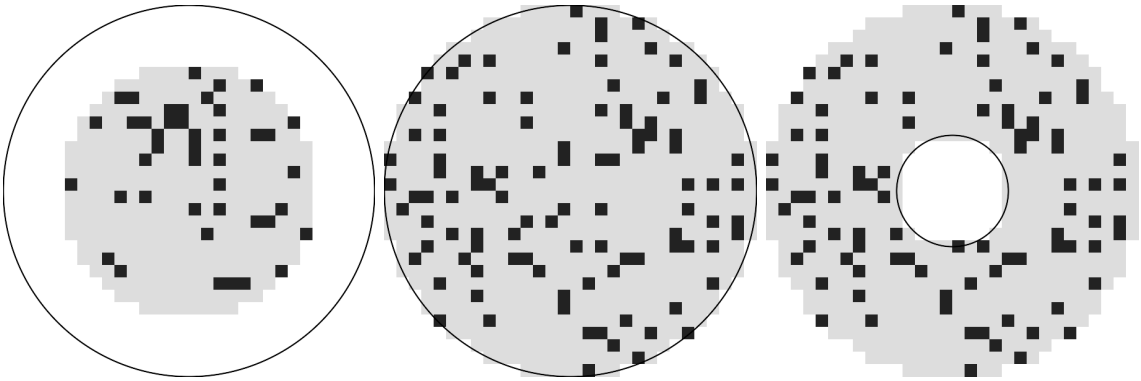

Figure 3.4: 2D cross sections of the Cloudy, Dusty, and Shell geometries. The darkness of the squares schematically indicates the density of dust in that area. For clumpy models, the density ratio is 100 (i.e. clumps have 100 times the density of the diffuse medium), while for homogeneous models, the density ratio is 1 (i.e. same density for gray and black squares). The stellar population is uniformly distributed inside the smooth circle.

radius. In the Dusty geometry, stars and dust are uniformly distributed in the sphere. In the Shell geometry, stars extend only to 0.3 times of the system radius and are surrounded by a shell of dust from 0.3 to 1.0 times of the system radius. Witt & Gordon (2000) found that a Shell geometry (with clumpiness) with $\tau_V \approx 1.5$ can reproduce the Calzetti Attenuation Law (Calzetti et al., 1994; Calzetti, 1997).

In addition to global geometry effects, clumpiness is also important. For a given mass of dust, clumpiness reduces the overall opacity and therefore the efficiency of dust in converting UV-optical radiation into IR. Popescu et al. (2000) found that while a single exponential diffuse dust disk can reproduce the optical and NIR emission, a clumpy distribution of dust that is spatially correlated with stars is needed to account for the FIR and sub-mm emission. Duval et al. (2014) found that a clumpy and dusty ISM appears more transparent to radiation (both line and continuum)

compared to an equivalent homogeneous ISM of equal dust optical depth. Witt & Gordon (1996) found that a minimum of two phases of non-zero density is necessary to model the interstellar dust medium in the Milky Way. In our clumpy models, we use a two-phase medium with a filling factor of 15% and a density ratio of 100 to implement clumpiness; Witt & Gordon (1996) found that these values reproduce the cloud mass spectrum and fractal dimension of the diffuse clouds in the Milky Way. For comparison, we also run homogeneous models which is equivalent to setting the density ratio to unity.

While spherical geometries are efficient for computation, they may not represent the realistic geometries of whole galaxies. For example, Baes et al. (2003) modeled spiral galaxies with double exponential disks, which more closely resembles spiral galaxies than our spherical models. Realistic geometries are suitable for studying individual objects, as they can provide spatial images and in principal reproduce detailed features better. However, they are not suitable for DirtyGrid because the radiative transfer in such geometries would take many orders of magnitude longer to compute, and the broadband SED may not contain sufficient information to constrain the additional parameters. Instead, we use simplified geometries to span the possible range in galactic environments. For the same amount of dust, the Shell geometry provides the highest efficiency in attenuation and is similar to the birth cloud of young stars, while the Cloudy geometry gives the lowest attenuation and is similar to the environments in elliptical galaxies or the bulge of spiral galaxies. In essence,

we model pieces of galaxies, and in the approximate limit where the global UV-IR SEDs of galaxies are dominated by a few representative types of non-interacting pieces, we can use a combination of models to fit the global SEDs. Within a single stellar population, we do not segregate the stars by age and place young stars in more embedded dust. However, we can approximate the segregation by combining the outputs of two models of different stellar ages, with the younger model having a higher optical depth than the older model.

In the DirtyGrid, stellar mass and the radius of the spherical geometry (the model size) are degenerate parameters. We use the same ratio of the clump size to the model size for all models. In each grid cell, the dust emission spectrum is calculated from the dust absorption spectrum. At each wavelength, the amount of energy absorbed depends on the radiation intensity. As we increase the model size (and therefore the grid cell size) by a factor of x, the radiation intensity in each cell drops by a factor of x^2. A corresponding increase in the stellar mass by a factor of x^2 restores the radiation intensity to the original level. The output SED will have the same shape but scaled up by a factor of x^2. Effectively, stellar mass per radius squared, essentially the mass surface density, determines the SED shape. Ivezic & Elitzur (1997) have a rigorous derivation of the scaling behavior in radiation transfer. In practice, we run all models with a 10 kpc radius and scale the output as needed.

3.3 Populating the parameter space

The parameter space of the DirtyGrid has 8 dimensions: global geometry, stellar age, metallicity, stellar scaling factor, star formation type (burst/constant), amount of dust, dust clumpiness, and dust grain type. The range of input parameters is discussed in in §3.2 and summarized in Table 3.1. Given the large parameter space, care in the sampling strategy can significantly reduce the resources needed to generate the grid. Among these 8 dimensions, we treat stellar age, stellar mass (through the stellar mass or SFR surface density; see § 3.2.2) and amount of dust as continuous variables because we are interested in deriving accurate values of these variables from SED fitting. We attempt to fully resolve the dependence of the broadband SEDs on the continuous variables while being conservative on the number of samples required. We designate the other 5 dimensions as discrete variables and bracket the possible range with a small number of samples, reducing the computation needed at the expense of the ability to derive accurate intermediate values.

Among the discrete dimensions, we have 3 grain types (MW, LMC and SMC), based on the Weingartner & Draine (2001) models (§ 3.2.3); 3 global geometries, Cloudy, Dusty and Shell, based on the Witt & Gordon (2000) geometries (§ 3.2.4); 2 local geometries, homogeneous and clumpy, later of which is based on the filling factor and density ratios in Witt & Gordon (1996) (§ 3.2.4); 2 types of star formation history, burst and constant (§ 3.2.2); and 5 values of metallicities. Each of these could be easily expanded into a full continuous dimension (e.g., one could define different

Table 3.1: Dimensions and ranges of the parameter grid and the number of first stage samples. The number of models in the first and second stages are 365K and 225K respectively. With an average run time of ~10 hours, the grid used ~5M CPU hours. The first 3 parameters are continuous variables and subject to non-uniform sampling and interpolation.

Parameter	Range	#samples
Continuous Variables		
Stellar Age	1 Myr – 13 Gyr	14–28
Stellar Mass	(depends on SF Type)	15
Amount of Dust	$\tau_{\mathrm{V,ext}} = 0.1 - 10$	7
Discrete Variables		
SF Type	burst/constant	2
Metallicity	Z = 0.0001 – 0.1	5
Global Geometry	Cloudy/Dusty/Shell	3
Local Geometry	homogeneous/clumpy	2
Grain Type	MW/LMC/SMC	3

levels of clumpiness), but this would greatly increase the amount of computation needed. Among the 5 discrete variables, metallicity could be the most interesting one to expand into a continuous dimension, but our preliminary results show that UV-IR SED fitting typically cannot constrain metalliticity to high accuracy, so we only selected the discrete metallicity values of Z = 0.0001, 0.0004, 0.004, 0.02, and 0.1, where the Padova evolutionary tracks are available, thereby removing the need to interpolate the tracks.

For the 3 continuous variables, we adopt a 2-stage sampling strategy. Because of the high number of samples in these 3 dimensions, running all combinations of samples that are required to fully resolve each of these 3 dimensions independently is computationally expensive. Since the rate of change of broadband fluxes may depend on which part of the parameter space we are in, a non-uniform sampling of these 3 dimensions can greatly reduce the number of models needed. We can then interpolate the broadband fluxes over the missing samples, where the rate of change with respect to the interpolating variables is slow or constant. The first stage sampling involves a mostly uniform grid (except in the stellar age dimension), and the selection is guided by a high resolution study of the dimensions in a limited parameter space. Table 3.1 provides a summary of the first stage sampling. Based upon the observed behavior in the first stage, the second stage sampling involves filling in more models around grid points where the SED changes rapidly, and is non-uniform.

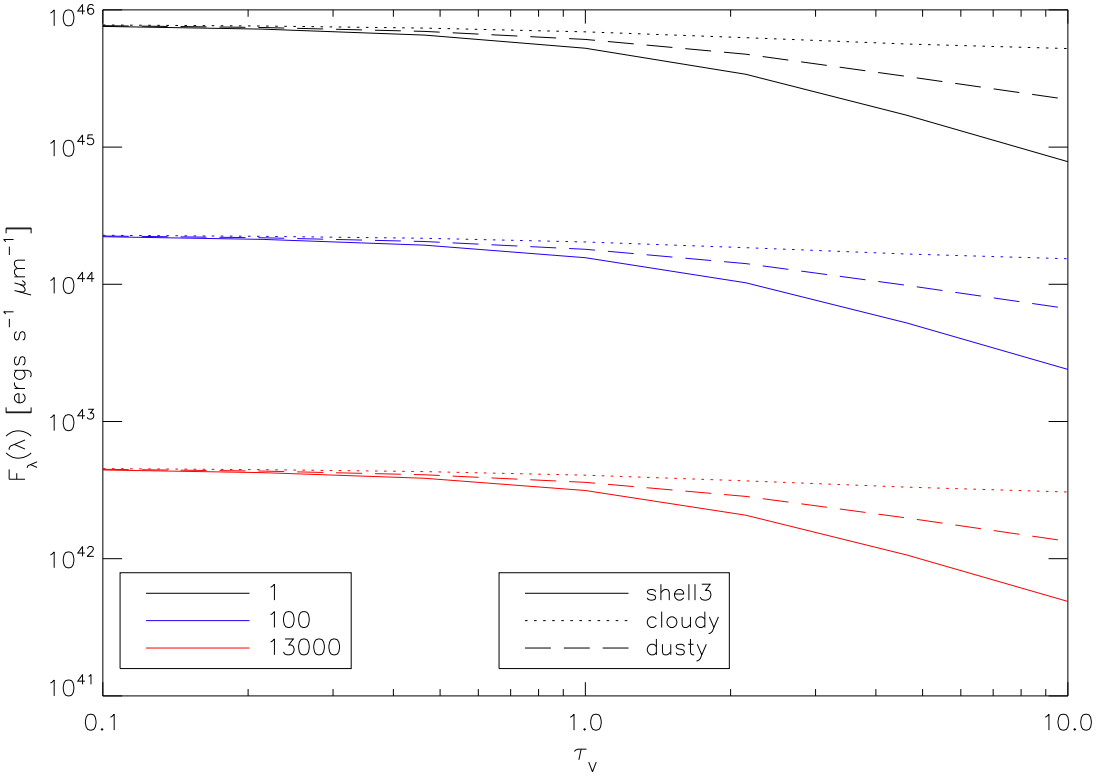

Figure 3.5: Optical V band flux vs optical depth for 3 stellar ages (1, 100 and 13000 Myr) and 3 clumpy geometries (Shell, Dusty and Cloudy). In general, band integrated fluxes vary smoothly with optical depth. The smoothness enables the use of interpolation to greatly reduce the number of optical depths needed.

3.3.1 First-stage sampling

Prior to running the first stage sampling, we ran pilot models with high resolution in each of the 3 continuous dimensions to study the behavior in these dimensions individually. We found that the band fluxes vary smoothly as a function of optical depth. While the precise details of the output spectrum are sensitive to the parameters, the band integrated fluxes (e.g., using the Johnson UBVRI band pass filters) are much less sensitive. This allows us to sample optical depths sparsely and then interpolate

over intermediate optical depths to get band fluxes at the intermediate values. Note that the first stage sampling does not have to be precise, because the second stage sampling fills in where the sampling is insufficient in the first stage.

Figure 3.5 shows that the optical V band fluxes vary smoothly over two dex of optical depth (from τ_v= 0.1 to 10.0). To quantitatively measure the error interpolation introduces, we ran the model with 25 different optical depths and selected stellar ages and geometries with all other parameters fixed (solar metallicity, instantaneous star formation and clumpy MW dust). The 25 different values are logarithmically evenly spaced between $\tau_v = 0.1$ and 10. Then we take 1 model from every 4 models, resulting in 7 (including the ones on the edge) models sparsely sampling the optical depth. From these 7 models we calculate the band fluxes, and use linear interpolation (in log space) to predict the band fluxes at the intermediate optical depths, and finally compare the interpolated fluxes and actual fluxes. For the limited parameter space we looked at, they generally agree within 1%. The behavior for stellar mass is also smooth, and we choose to use only 15 samples to span over 7 dex of stellar mass values, including the edge points.

The behavior of stellar ages, however, requires many more samples to resolve. For the purpose of the first stage sampling in stellar age, we study the band integrated fluxes of the unreddened spectra of stellar populations, which do not require radiative transfer. In Figure 3.6, we plot the V band fluxes against the full range of stellar ages, sampled at 47 points. Between 10 Myr and 13 Gyr, the age samples are roughly

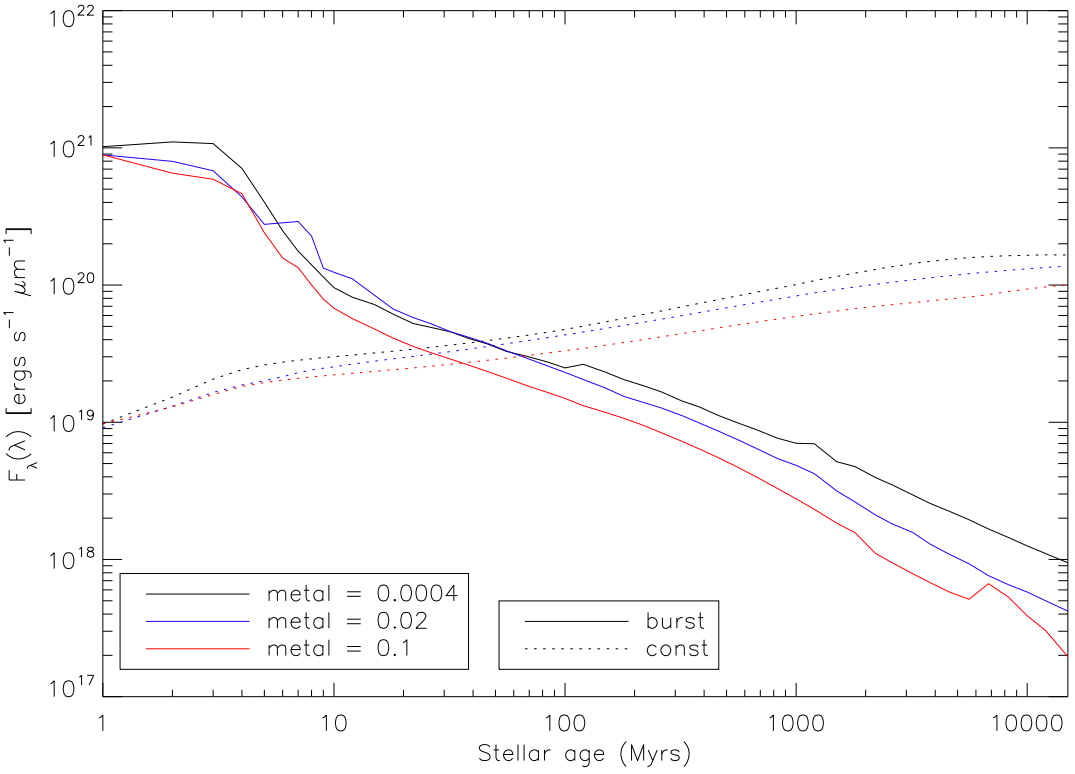

Figure 3.6: Unreddened optical V band flux vs stellar age. While the behavior is smooth for constant star formation models (const), the changes are quite abrupt for instantaneous star formation models (burst), especially between 1 Myr and 10 Myr. As such, we spent more computational resources for the burst models. Note that the burst models shows different features for different metallicities.

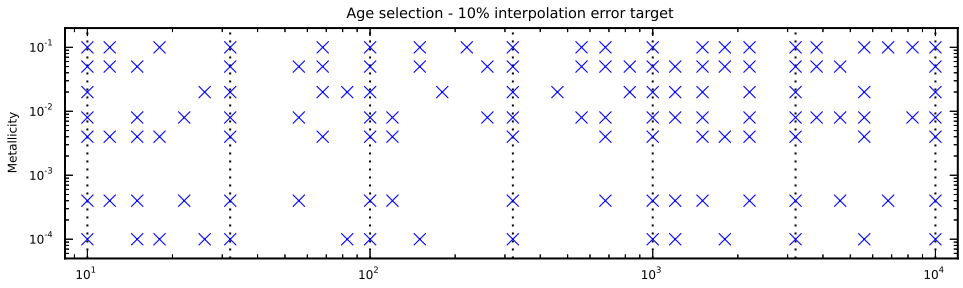

Figure 3.7: Non-uniform age selection for models with instantaneous star formation. The blue points indicate our age samples (horizontal axis), which depend on the metallicity. The vertical dotted lines indicate age values that we always samples (2 per dex). We choose them using an algorithm that picks the minimum number of points to achieve <10% interpolation error in all bands. Note that while this figure shows the results for 7 metallicities available in the Padova tracks for completeness, we only use 5 of them in the DirtyGrid.

evenly spaced in log space (12 per dex), but below 10 Myr we included all integer multiples of Myr because PEGASE does not output results at fractional Myr ages. Having a constant amount of young stars and a steadily increasing amount of old stars, the constant star formation models give a much smoother curve. On the other hand, instantaneous star formation models exhibits relatively sharp changes in V band fluxes as they evolve. This is due to evolved stars entering rapidly changing phases or the death of luminous stars. In order to achieve <10% accuracy in band fluxes, we find that we need 14 samples of ages for constant star formation models, but the number for instantaneous star formation models is much higher and depends on the metallicity.

To pick the minimum number of samples needed to reach 10% error due to age interpolation in burst models, we did an exhaustive search for the optimal set under constraints. From 10 Myr to 10 Gyr, we divided the range of age into 6 equal segments

(in log space). For example, the first segment goes from 10 Myr to 32 Myr. In each segment, we have 5 possible sample locations that are uniformly distributed. At each location, the sample is either present or absent. For each of the $2^5 = 32$ combinations, we compute the band integrated fluxes and interpolate the fluxes at the missing samples. We compare the interpolated fluxes with the correct fluxes to get the fractional error. With a error target of $<10\%$, we pick the minimum number of samples needed in each segment and arrive at a list of selected ages. We run the age selection algorithm for different star formation type and metallicity separately. Figure 3.7 shows our age selection for models with instantaneous star formation from 10 Myr to 10 Gyr. The number of age samples for burst models ranges from 22 to 28, with an average of 24.6.

3.3.2 Second-stage sampling

We improve upon the first stage sampling by filling in models at locations with insufficient interpolation accuracy. Because of possible non-linearity in the SED landscape, we cannot determine the error in the interpolated fluxes at locations of the parameter space at which we have not sampled. Even in rapidly changing areas, the interpolated fluxes could be accurate if the changes are smooth. As an estimate of the interpolation accuracy, we again compared the actual band fluxes of each models with the interpolated band fluxes using the nearby points. Above a threshold of error (15%), we fill in more samples around such models. To choose the second stage

samples, we apply the following procedure for each of the 3 continuous dimensions (denoted as x):

1. Loop over each samples in the grid, except the ones with the maximum or minimum allowed values of x.

2. While ignoring the current sample, interpolate the broadband fluxes between the model that has a higher value of x and the model that has a lower value of x

3. Compare the broadband fluxes of the current sample with the interpolated fluxes

4. If the error in any of the bands is greater than 15%, include the two neighboring grid points of the current sample (in the x dimension) in the second stage sampling

We calculate the error of the interpolated fluxes assuming that the actual model has the true values. The procedure identified 225K locations to fill in second stage samples. In the final DirtyGrid, we interpolate over the parameter space using the combined set of first and second stage samples.

3.4 Results

The panel of plots in Figure 3.8 illustrates the dependence of the model output spectra on the model input parameters. The scale of each plot is the same to show how

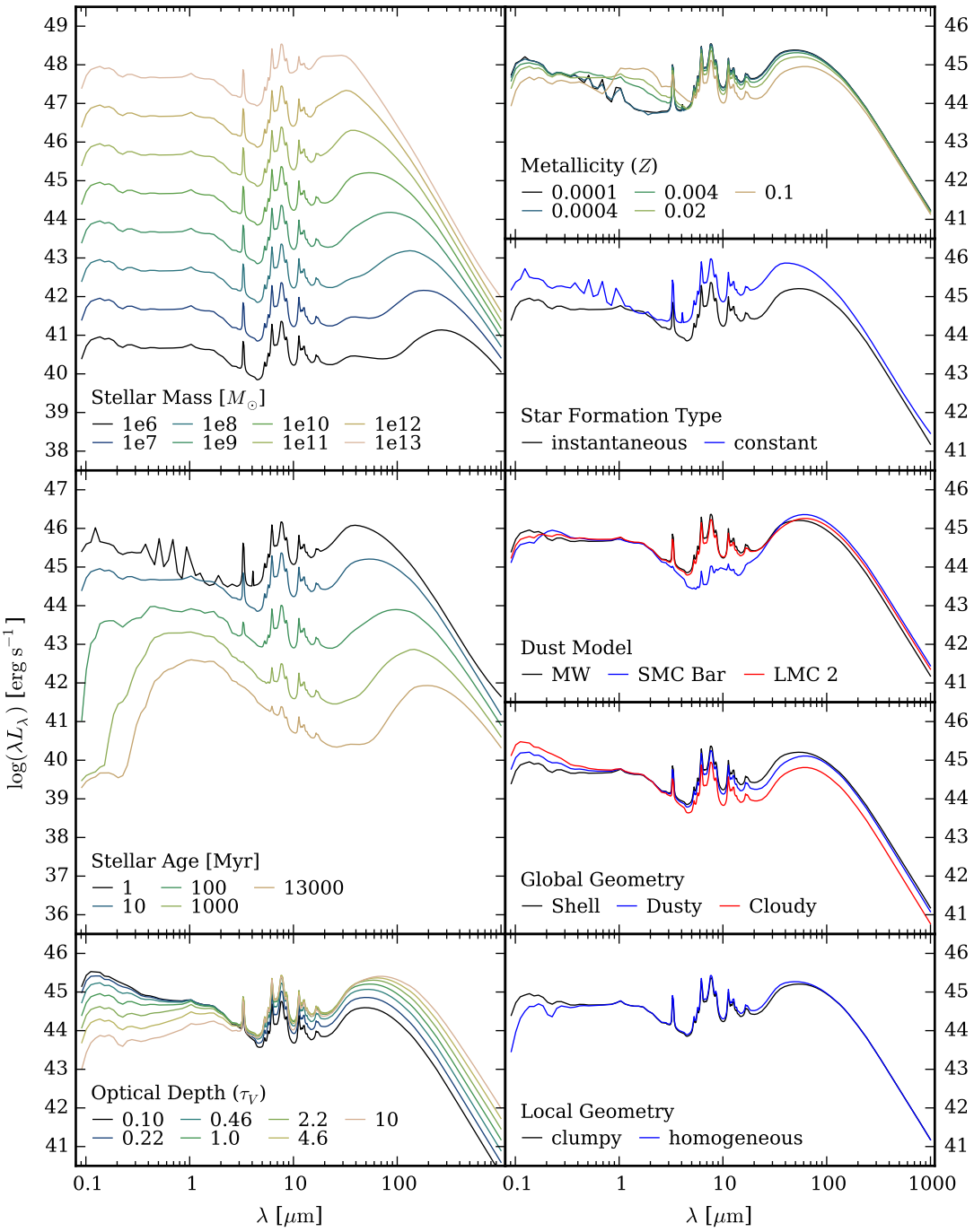

Figure 3.8: Example DIRTY model output spectra showing the variations in each dimension of the parameter grid. In each plot, we vary one parameter and fix all the others. The fixed parameter values are: 10 Myr old stellar age, 10^{10} solar masses, solar metallicity, instantaneous star formation, $\tau_{\rm V,ext} = 1$, Milky Way type dust, shell geometry, 10 kpc radius, and clumpy dust, except when shown in the legend of each plot.

the amplitude of change of the parameters compares to each other. When all other parameters are held constant, an increase in the stellar age reddens the UV-optical spectra and decreases the total stellar luminosity, due to the death of luminous and UV-bright stars. Both of these effects decrease the average dust temperature and shift the peak of the dust emission in the far-IR to a longer wavelength. The oscillations at optical wavelengths for the 1 Myr model is due to the existence of strong nebular emission lines and our relatively low resolution wavelength grid that does not resolve the lines. This is acceptable because the change in the broadband fluxes due to the dust radiative transfer does not depend sensitively on the precise wavelength of the gas emission lines. Since the total amount of input radiation scales with stellar mass, the stellar mass plot shows the greatest change in the level of output flux. A higher stellar mass also results in higher dust temperature. Stellar metallicity correlates with the UV radiation field hardness and therefore the total amount of dust emission. Its effect on the intrinsic near-IR colors are prominent in the output spectra. In the star formation type plot, we compare an instantaneous star formation model to a continuous star formation model with the same total stellar mass formed. While both models have a 10 Myr stellar population age, the latter spectra resembles a 1 Myr instantaneous star formation model but with a lower fraction of energy in the emission lines. Optical depth determines how much energy is absorbed in the UV-optical and re-emitted into the IR, so it is the primary driver behind changes in the IR to UV ratio. The values shown in the legend in the dust extinction optical depth

at V band ($\tau_{V,\mathrm{ext}}$). The attenuation optical depth at V band ($\tau_{V,\mathrm{att}}$), which includes the radiative transfer effects, also depends on the geometry. The Shell geometry gives the highest attenuation, followed by Dusty and Cloudy. The effect of changing the geometry from Cloudy to Shell is similar to increasing $\tau_{V,\mathrm{ext}}$, except that in the former case the dust temperature increases, while in the latter it decreases. Dust clumpiness has a lesser effect on the overall attenuation, but the change in attenuation at extreme UV wavelength is significant. Finally, the choice of dust grain model also affects the attenuation curve, but the most prominent effect is the strength of the PAH emissions around 8 μm. The MW dust grain model has the highest PAH fraction, followed by LMC and SMC, and this is reflected in the fraction of energy emitted at around 8 μm.

In order to fit these model spectra to broadband SEDs of real galaxies, we need to compute the fluxes that various instruments would measure if they were to observe the hypothetical models as an object on the sky. The conversion from model spectra to broadband luminosities require the use of band pass filters of each instrument, also known as filter response functions. We integrate the DirtyGrid spectra multiplied by the band pass filters of GALEX FUV/NUV, Johnson UBVRI, SDSS *ugriz*, 2MASS $\mathrm{JHK_S}$, Spitzer IRAC/MIPS, and Herschel PACS/SPIRE (Hora et al., 2008; Engelbracht et al., 2007; Gordon et al., 2007; Stansberry et al., 2007). We then interpolate the broadband luminosities in the stellar age, stellar mass and optical depth parameter to arrive at a regular 8-dimensional cube of luminosities in each band, using linear

Table 3.2: Band integrated luminosities of DIRTY models in the GALEX, SDSS, Johnson optical/near-IR, Spitzer IRAC/MIPS and Herschel SPIRE bands. All luminosities are in erg s^{-1} μm^{-1}, stellar age is in Myr and stellar mass is in $M_{\odot}$. The lines are wrapped for display purpose. The full table is available online.

Model ID	Geometry	Dust type	Stellar age	Metallicity	SF type	τ_V	Stellar mass
	GALEX/FUV	GALEX/NUV	SDSS/u	SDSS/g	SDSS/r	SDSS/i	SDSS/z
	U	B	V	R	I		
	J	H	K	IRAC1	IRAC2	IRAC3	IRAC4
	MIPS24	MIPS70	MIPS160	SPIRE250	SPIRE350	SPIRE500	
AB2820	homo/cloudy	SMC	1	0.004	burst	10	1.0E+8
	4.59E+44	1.71E+44	9.64E+43	6.05E+43	2.95E+43	2.75E+43	1.60E+43
	9.56E+43	5.27E+43	5.15E+43	3.26E+43	1.13E+43		
	3.35E+42	1.18E+42	8.23E+41	2.80E+41	2.55E+41	1.92E+41	2.37E+41
	1.66E+41	2.68E+41	5.51E+41	1.93E+41	5.47E+40	1.16E+40	
AB2823	homo/cloudy	SMC	100	0.0004	burst	0.464159	1.0E+8
	1.27E+43	6.94E+42	3.70E+42	3.44E+42	1.78E+42	1.09E+42	7.19E+41
	3.76E+42	3.87E+42	2.37E+42	1.56E+42	9.17E+41		
	3.19E+41	1.46E+41	5.43E+40	1.00E+40	4.15E+39	2.33E+39	
	2.44E+39	1.44E+39	1.11E+39	2.98E+39	2.03E+39	8.11E+38	2.19E+38
AB2883	homo/cloudy	SMC	100	0.02	burst	10	1.0E+8
	5.07E+42	3.01E+42	1.93E+42	1.96E+42	1.17E+42	8.20E+41	6.92E+41
	1.96E+42	2.15E+42	1.45E+42	1.05E+42	7.49E+41		
	5.04E+41	3.52E+41	1.63E+41	3.68E+40	1.67E+40	8.07E+39	
	3.89E+39	1.02E+39	8.10E+38	2.18E+39	3.48E+39	2.57E+39	1.12E+39
AB2887	homo/cloudy	SMC	13000	0.02	burst	1	1.0E+8
	7.31E+38	7.88E+38	9.67E+39	3.27E+40	4.44E+40	4.42E+40	4.53E+40
	1.03E+40	2.73E+40	4.15E+40	4.43E+40	4.48E+40		
	3.34E+40	2.33E+40	9.93E+39	1.96E+39	7.88E+38	3.29E+38	1.08E+38
	3.10E+36	1.17E+36	1.29E+36	3.85E+36	6.26E+36	6.03E+36	

interpolation in log space. We present the resultant broadband SEDs in an online table and a few of them in Table 3.2 as an example.

After the completion of the grid, we run 30,000 models at randomly selected locations in the parameter grid. We then compare their integrated band fluxes to the interpolated fluxes obtained from the grid without these additional 30,000 models. The typical error introduced by interpolation is ~3%. The largest interpolation error (~10%) comes from the FUV band of evolved stellar populations. In instantaneous star formation models, the FUV rapidly decreases as the stellar population ages, and our sampling of stellar age in the DirtyGrid is not sufficient to resolve the detailed behavior in FUV. The same issue affects the NUV to a lesser extent. This is usually not a problem because the FUV flux in normal star forming galaxies is dominated by young populations, but it could result in reduced constraining power of the FUV band in fitting elliptical galaxies or galaxies that primarily contain evolved stellar populations.

3.5 Summary

In this chapter, we described how we construct the DirtyGrid, a grid of models of UV to IR/sub-mm SEDs of dusty stellar populations. This serves as the foundation of the next chapter, where we use combinations of these models to study the dust properties and the accuracy of star formation rate indicators in nearby galaxies.

Beginning with intrinsic stellar and gas spectra from the stellar population model PEGASE, the radiative transfer model DIRTY self-consistently compute the absorption, scattering, and re-emission of dust grains. We use the MW, LMC, and SMC dust grain models in Weingartner & Draine (2001) with simplified geometries that simulate galactic environments. We explained how we choose the parameters—wide enough to cover the possible physical range, and dense enough to achieve the desired accuracy while keeping the computation manageable. The landscape of the output SED is not uniform, with more rapid changes in some part of the parameter space and less in others, which inspired our use of a two-stage sampling strategy. We present a few example SEDs in this paper and the full set is available in an online table. By adding more realistic dust grain physics and physically connecting the UV-optical to the IR/sub-mm, these SEDs represent a clear step forward in the current state-of-the-art modeling of dust and stellar populations.

This project is supported by the NASA ADAP grant 11-ADAP11-0112, "Dusty Spectral Energy Distributions of Star Formation in Nearby Galaxies". We would like to thank the Extreme Science and Engineering Discovery Environment (XSEDE), the NASA Advanced Supercomputing (NAS) facility, and the NASA Center for Climate Simulation (NCCS) for providing their computational resources. Without these resources, this project would not be possible.

Chapter 4

DirtyGrid II: Dust properties and star formation indicators in SINGS galaxies

Abstract

We study the dust and star formation properties of the SINGS galaxies by fitting the ultraviolet to sub-millimeter spectral energy distributions using our grid of radiative transfer models, the DirtyGrid. We find that we need a minimum of two components of different stellar ages, representing a young and an old stellar population, in order to obtain good fits for most of the galaxies. Our total dust masses agree with literature dust masses to within a factor of 2, and the residuals correlate most strongly with the stellar mass surface density of the old component. The LMC 2 dust grain model best describes the dust found in these normal star forming galaxies. The attenuation curves are steeper than those found previously for starburst galaxies, and we observe a weak 2175 Å feature. We find that the DirtyGrid SFRs are consistent with a number of literature SFR indicators within a factor of two. We do find differences that are primarily due to contamination from the old stellar population that the DirtyGrid SFRs account for on a galaxy-by-galaxy basis using the information present in the full UV-IR SED.

4.1 Introduction

Interstellar dust is an important component of the interstellar medium and of galaxy evolution. Dust is one of the controlling factors in the formation of stars as dust grain surfaces are the formation site of molecular hydrogen. Conversely, star formation is critical to dust as it is stars that synthesize the heavy elements (metals) that constitute the basic elements of dust grains. Thus, the formation and destruction of interstellar dust is an important process in the evolution of the interstellar medium in galaxies. In addition, dust absorption and scattering alter the appearance of stars and galaxies in the ultraviolet (UV) and optical, and dust emission dominates infrared (IR) emissions in normal star forming galaxies.

Observations in the Milky Way (MW), Large Magellanic Cloud (LMC), and Small Magellanic Cloud (SMC) revealed that the wavelength dependence of dust extinction varies significantly in different environments (Gordon et al., 2003). The average extinction curve in the MW has a 2175 Å bump that is commonly attributed to carbonaceous materials (e.g. Draine, 2003). Cardelli et al. (1989) proposed that the average MW extinction can be parametrized as a family of extinction curves that depends on the single parameter R_V. However, this family of extinction curves does not include the average extinction curve in the SMC, which is characterized by the lack of the 2175 Å bump and a strong far-UV rise. The average extinction curve in LMC 2 supergiant shell region is intermediate between the MW and SMC curves. It is possible to reproduce the differences between MW, LMC, and SMC under a

unified framework by adjusting the size distribution and composition of dust grains (Weingartner & Draine, 2001).

Energy absorbed by dust in the UV-optical is re-radiated in the IR. Dust emission in the far-IR comes from equilibrium heating of dust grains and can be approximately described as a featureless modified blackbody function. However, rich spectral features that are commonly attributed to polycyclic aromatic hydrocarbons (PAH) exist in mid-IR emissions (Leger & Puget, 1984). In local starburst galaxies, Engelbracht et al. (2008) found that the equivalent width of the 8 μm aromatic emission complex negatively correlates with the radiation field hardness and positively correlates with metallicity. Gordon et al. (2008) further found that the former correlation is stronger than the latter in M101, suggesting that the variation in the strength of aromatic emissions is due to dust processing, instead of differences in dust formation.

The TIR-to-FUV ratio correlates with the UV spectral slope (β) both across galaxies (Meurer et al., 1995) and within galaxies (Calzetti et al., 2005). While the relation is tight for starburst galaxies (Meurer et al., 1999), significant scatter exists for normal star forming galaxies (Bell, 2002). Kong et al. (2004) found that the higher β at a given TIR-to-FUV ratio in more quiescent star formation galaxies can be explained in terms of the ratio of present to past averaged star formation rate. Given that β is commonly measured from the GALEX far-UV (FUV) and near-UV (NUV) bands and that the NUV band captures the 2175 Å extinction feature, variation in the 2175 Å feature strength can have a profound impact on β, but is challenging to

determine from empirical methods.

In galaxies, attenuation curves summarize the combined effects of dust absorption and scattering, both out of the beam and into the beam, in a complex geometry where the stars, gas, and dust are mixed. Such curves are harder to model from first principles than extinction curves of single stars because of the highly non-linear radiative transfer effects. If the attenuation curve of a galaxy is known, we can accurately remove the effects of dust from the UV to near-IR spectral energy distribution (SED) of the galaxy (Fitzpatrick, 1999). However, both theory and observations suggest that there are significant variations in the attenuation curves between galaxies as well as within a single galaxy. Such variations can reflect differences in the underlying physical conditions of a galaxy's ISM; for example, radiative transfer models have shown that the attenuation curve flattens as the amount of dust increases (Witt & Gordon, 2000). Noll et al. (2007) modeled the observed SEDs of high redshift galaxies and found that the 2175 Å bump strength is anti-correlated with the luminosity of the galaxies.

It is possible to empirically derive attenuation curves of galaxies using a method similar to the "pair method" commonly used to derive extinction curves towards stars. Calzetti et al. (1994) found that in starburst galaxies, the difference in optical depth between the nebular emission lines Hα and Hβ (τ_B^l) linearly correlates with the UV spectral slope β, and that allowed them to derive an attenuation law from the ratios of the average spectra in 5 τ_B^l bins. Wild et al. (2011) derived attenuation curves by

comparing pairs of galaxies with similar intrinsic properties in a much larger sample. This method allows them to study variations in the attenuation curve, but matching galaxies may suffer from uncertainties due to imperfect understanding on the intrinsic unreddened spectra.

Measurement of star formation rate (SFR) in galaxies is a problem that is tightly coupled with dust. Examples of commonly used SFR indicators include the FUV, Hα, and total infrared (TIR) luminosities (Kennicutt et al., 2009; Hao et al., 2011). The FUV and Hα luminosities suffers from dust attenuation, while TIR originates from dust emission that is powered by the absorbed energy in the UV-optical. More accurate modeling of dust provides insight on the accuracy and applicability of these SFR indicators individually and in combination.

Galaxy surveys such as the Spitzer Infrared Nearby Galaxies Survey (SINGS, Kennicutt et al., 2003), the Local Volume Legacy Survey (LVL, Dale et al., 2009) and the Great Observatories All-sky LIRG Survey (GOALS, Armus et al., 2009) have resulted in a large number of well measured multi-wavelength SEDs of galaxies. The full UV-IR SED contains information about both the dust and the stars. A self-consistent model of the full UV-IR SED allows us to make use of the full information to simultaneously solve for dust and stars.

There have been successful attempts at building simplified UV-IR SED models that work for a large set of galaxies. For example, using the Charlot & Fall (2000) prescription for dust attenuation and multiple components of dust emissions linked

by energy conversation, da Cunha et al. (2008) constructed a full UV-IR SED model to fit the SINGS galaxies. They applied a power-law attenuation curve ($\propto \lambda^{-0.7}$) to stellar spectra calculated by the Bruzual & Charlot (2003) stellar population model. Stars younger than the birth cloud dissipation time scale ($\sim$ 10 Myr) are subject to additional dust opacity with a different power-law ($\propto \lambda^{-1.3}$). They model dust emissions with (1) a PAH emission template with fixed spectral shape measured in the MW, (2) 3 fixed temperature modified blackbodies at 850, 250 and 130 K intended to emulate stochastic emissions, (3) and a low temperature modified blackbody with variable temperature intended to match equilibrium emissions.

With the DirtyGrid, we improve upon previous studies by including more realistic dust physics and radiative transfer effects to model the UV-IR SEDs of galaxies. The DirtyGrid is a grid of radiative transfer models spanning the full observed range of stellar and dust properties seen in local star forming galaxies. Beginning with the dust-free stellar spectra calculated from the stellar population model Fioc & Rocca-Volmerange (1997), we use Monte Carlo techniques and the Weingartner & Draine (2001) dust grain models to calculate the global SED of dusty stellar populations. We include important physical processes such as anisotropic scattering and stochastic heating. For a full description of DirtyGrid, please refer to Chapter 3.

Compared to using assumed attenuation curve shapes, empirical IR templates, and energy conservation to model SEDs, our method has a number of advantages: (1) we connect the UV-optical to the IR with dust physics, thereby providing a physical

constraint on the allowed combinations of UV-optical and IR SEDs, (2) we calculate the stochastic heating of dust grains from a self-consistent radiation field and the heat capacity of small grains, allowing for variations of the mid-IR emission strength which may depend on radiation hardness and other parameters, (3) while empirical models are powerful tools to find trends and correlations, a physical model allow us to identify the underlying physical quantities and processes that govern these trends. We can, for example, determine the attenuation curve for each galaxy without binning nor matching galaxies, and recover the star formation rate by separating the young and old star populations for each galaxy.

In this work, we study the global integrated SEDs of whole, nearby galaxies in the SINGS sample. In the following sections, we describe the data and model we use, our fitting technique, and the derived dust and start formation properties of the SINGS galaxies.

4.2 Data

In this paper, we fit the global SEDs of a subsample of the SINGS (Kennicutt et al., 2003) galaxies. The original SINGS sample of 75 galaxies was chosen to span the range of star forming galaxies in the local universe, including a wide range of optical morphologies, luminosities, and infrared to optical ratios. Consistent aperture matched photometry exists for these galaxies from GALEX UV, SDSS optical,

2MASS near-IR, Spitzer mid and far-IR, and Herschel sub-mm images. This provides a homogeneous set of full UV to sub-mm global SEDs for these galaxies. A number of studies related to our work have been carried out on this set of data including deriving dust properties from fitting the IR SEDs (Draine et al., 2007), investigating the star formation efficiency (Leroy et al., 2008b), studying the radial distribution of stars, gas and dust (Muñoz-Mateos et al., 2009a,b, 2011), estimating the metallicity content, and as a prerequisite, the AGN signatures (Moustakas et al., 2010), calibrating star formation rate indicators (Calzetti et al., 2010; Kennicutt et al., 2009; Hao et al., 2011), and developing semi-analytic models to fit the full UV to IR/sub-mm SEDs (Noll et al., 2009a; da Cunha et al., 2008).

We have built the dataset for this paper by assembling the SEDs with GALEX UV and Spitzer IRAC/MIPS IR data from Dale et al. (2007), optical data from Muñoz-Mateos et al. (2009a), and Herschel sub-mm data from Dale et al. (2012). We use the UV fluxes from Muñoz-Mateos et al. (2009a) for IC 4710, NGC 3184, and NGC 5033 as the UV fluxes for these galaxies were not given by Dale et al. (2007). The optical *BVRI* data in Dale et al. (2007) suffered from zero-point calibration problems, so we use the SDSS data and recalibrated *BVRI* data in Muñoz-Mateos et al. (2009a) instead. While Dale et al. (2007) used matched aperture photometry for all bands, Muñoz-Mateos et al. (2009a) provided asymptotic magnitudes of the radial profiles of the fluxes, and since both of them capture the whole galaxy, combining data from the two results in consistent SEDs. Noll et al. (2009b) employed the same strategy

to assemble the SEDs for SINGS galaxies.

In their study of dust properties of SINGS galaxies, Draine et al. (2007) removed 9 sources (NGC 0584, NGC 1404, NGC 3034, NGC 4552, M81 Dwarf A, M81 Dwarf B, Holmberg IX, DDO 154 and DDO 165) due to background contamination, detector saturation or poor detection. Since these issues would also affect our work, we also remove them from the present study. GALEX FUV data is crucial in constraining the stellar age, dust opacity, and dust type. We remove the 8 galaxies for which GALEX FUV fluxes are not available. Finally we remove 14 sources for which neither SDSS optical fluxes nor recalibrated *BVRI* fluxes are available and arrive at a final sample of 44 galaxies. Each galaxy in this sample has complete data in the UV, near-IR and IRAC/MIPS bands, and at least 2 bands in the optical. Twenty four of these galaxies have SDSS optical data, while the other 20 have recalibrated *BRVI* data. In addition, 35 galaxies have sub-mm measurements.

In general, we use the uncertainties quoted in the various sources of global photometry. In addition, we adopt an absolute flux calibration uncertainty of 2.5% for SDSS and 12.5% for recalibrated *BVRI* fluxes as recommended by Muñoz-Mateos et al. (2009a). These uncertainties are added in quadrature to the reported statistical uncertainties. We adopt a total uncertainty value of 10% for the *JHK* bands, following the advice in Dale et al. (2007). None of the published data include correlations between uncertainties in different bands, so we conservatively assume the measurements are independent and thus do not use covariance matrices in our fitting.

Some of the SINGS galaxies contain Seyfert/LINER nuclei (Kennicutt et al., 2003). Moustakas et al. (2010) classified some nuclear, circum-nuclear, and radial strip regions of the SINGS galaxies as AGN using optical line diagnostics. They found that as the fraction of light inside the aperture increases, the regions are less likely to pass the AGN diagnostic test. These AGN cores have low luminosities and do not contribute significantly to the broadband SEDs. Noll et al. (2009a) and Law et al. (2011) modeled the SINGS galaxies without adding in an AGN component.

In Figure 4.1, we show the distribution of our sample of 44 galaxies in terms of optical morphological types. Our data driven selection procedure preferentially eliminated elliptical and irregular galaxies, limiting our ability to study the dust and stars in such galaxies. The rich range of late to early types of spiral galaxies in our sample does allow us to study how the dust and stellar properties depend on spiral galaxy structure.

4.3 Models

To model the global SEDs of galaxies, we use the DirtyGrid. The full details of the DirtyGrid are given in Chapter 3 and here we provide a summary of this model grid. The DIRTY radiative transfer model (Gordon et al., 2001; Misselt et al., 2001) computes the SEDs of stellar populations mixed with dust. As an input to DIRTY, we use stellar and gas SEDs generated by PEGASE.2 (Fioc & Rocca-Volmerange,

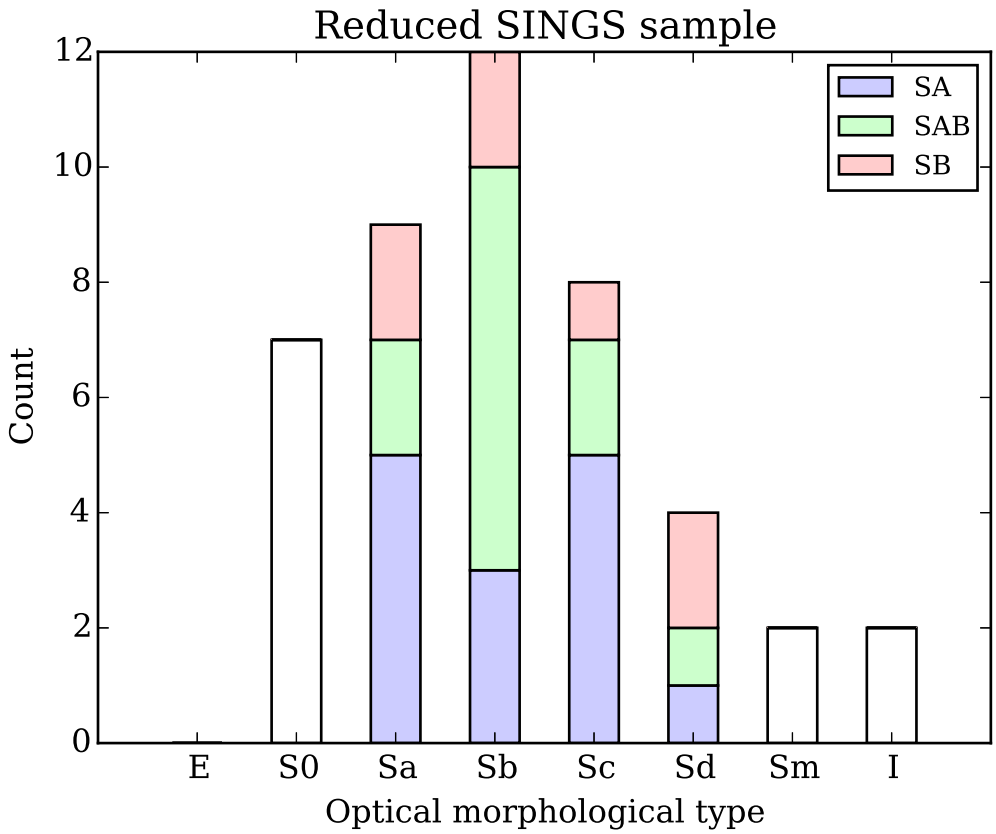

Figure 4.1: Histogram of optical morphological types of our reduced SINGS sample. After removing galaxies with detector saturation, non-detection or missing FUV/optical fluxes, we reduced the SINGS sample from 75 galaxies to 44. This procedure removed all elliptical and all but two irregular galaxies, but preserved a wide range of spiral galaxies.

1997) and the dust grain models of Weingartner & Draine (2001). We iteratively compute dust absorption and emission, resulting in a self-consistent radiation field. The DirtyGrid spans a wide range of parameters in stellar age, metallicity, star formation rate, star formation history, amount of dust, global geometry, dust clumpiness, and dust grain type. We resolve the behaviors of stellar age, star formation rate, and amount of dust via an adaptive sampling of these parameters. The grid of models is designed to span the possible range of stellar, dust, and geometric parameters of stellar populations in galactic environments. Under the assumption that the UV-IR SEDs of normal star forming galaxies are dominated by one or a few types of characteristic star forming regions unique to each galaxy, we can use combinations of models in the grid to fit the global SED of a galaxy.

To illustrate that the DirtyGrid spans the full range of stellar and dust properties, we compare the SINGS galaxies to our models on the IRX–UV diagram in Figure 4.2. Using a sample of 50 nearby starburst galaxies, Kong et al. (2004) calibrated the IRX–UV relation of $L_{\rm dust}/L_{\rm FUV}$ and $\beta_{\rm GLX}$ (the UV slope calculated from GALEX FUV and NUV broadband fluxes), shown as a black curve in our figure. Normal star forming galaxies, which are quiescent compared to starburst galaxies, deviate from the trend in that they have lower $L_{\rm dust}/L_{\rm FUV}$ values for a given $\beta_{\rm GLX}$. Their modeling results suggest that an increase in β along the trend corresponds to an increase in attenuation, and deviations from the trend is related to star forming history, in terms of the ratio of present to past-average star formation rate. Noll et al. (2009a) studied the SINGS

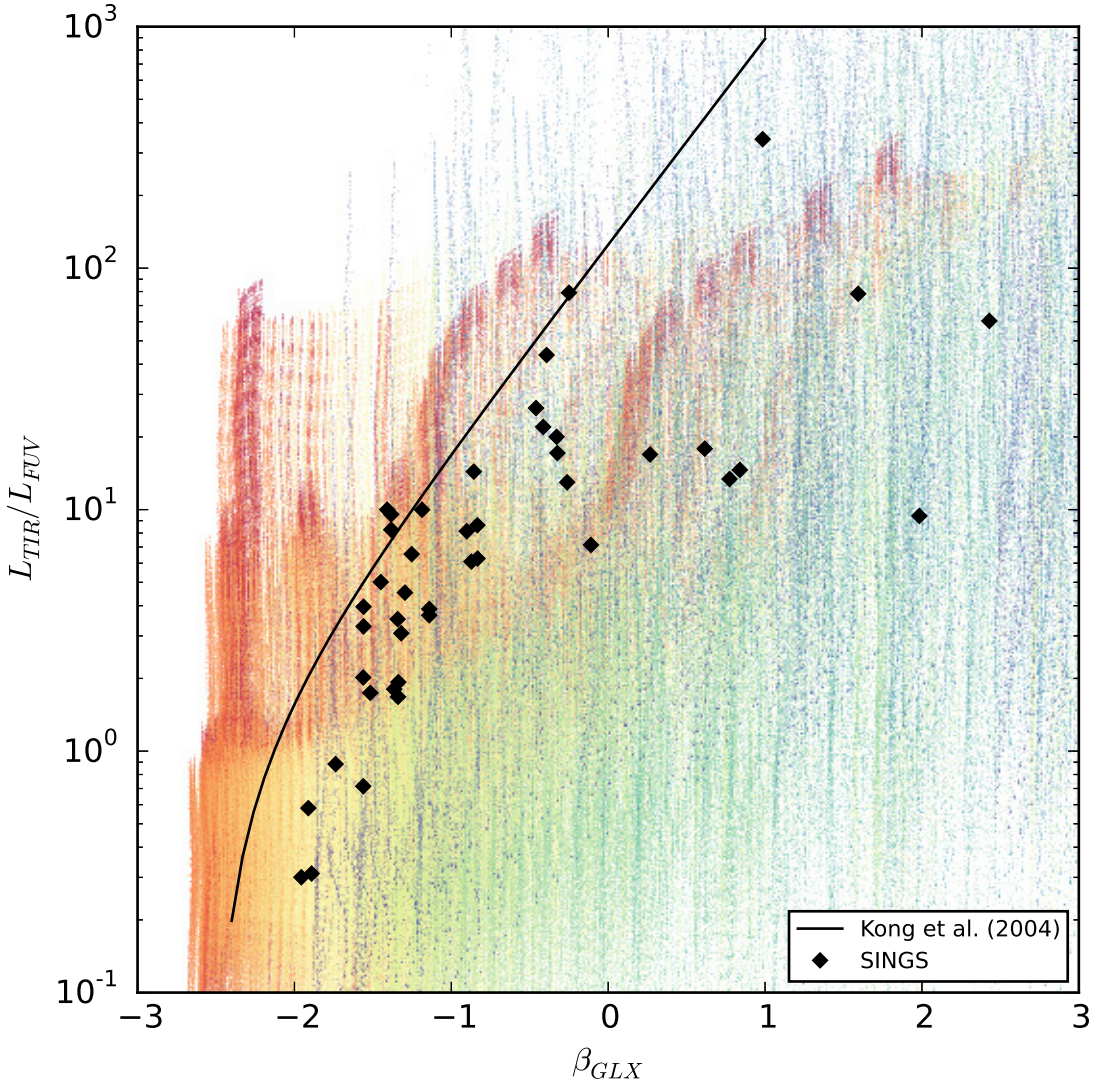

Figure 4.2: IRX-β relation for the DirtyGrid models with instantaneous star formation (background pixels), SINGS galaxies in our reduced sample (black diamonds), and the Kong et al. (2004) IRX-UV relation for starburst galaxies. The rainbow colors presents the age of the DirtyGrid models from red (youngest, 1 Myr) to blue (oldest, 13 Gyr). The three red arms of higher density are due to the three discrete dust type in the DirtyGrid—MW, LMC and SMC—which have different slopes in their UV extinction curves. This figure shows that our models cover the full range of our galaxy sample.

sample with CIGALE models, which are constructed from Maraston (2005) stellar population models, Salpeter IMF, two populations of exponentially decaying star formation, Calzetti et al. (2000) attenuation law with modifications, and Dale & Helou (2002) IR templates. In their models, they found that it is necessary to use different amounts of attenuation for young and old stellar populations to reproduce the deviation of quiescent SINGS galaxies from the starburst IRX–UV relation. They suggested that these galaxies have a high obscuration of a young stellar component of very low mass and nearly unattenuated old stellar populations.

In the DirtyGrid, we find that instantaneous star formation models with old stellar ages can reproduce the deviations alone. Continuous star formation models (not shown), on the other hand, follow the starburst IRX–UV relation much more closely. This is due to the continued existence of young stars in a constant star formation population. Figure 4.2 shows that our models cover a wider range than observed galaxies, supporting our claim that the DirtyGrid is suitable for studying these galaxies.

Among the parameters in the DirtyGrid, geometry, optical depth, dust type, and stellar age (for burst models) have large effects on the position of the model on the figure. The first two parameters exert their effects though the change in effective attenuation, while the last two determine the ultraviolet slope. Stellar mass, metallicity, and stellar age (for constant star formation models) have smaller effects on the position (less than 1 dex in β). An increase in stellar mass mildly increases

the IR to FUV ratio (due to the specific formulation of the Dale & Helou 2002 TIR formula). Increasing metallicity increases β, due to line bracketing effects. Increasing stellar age (for constant star formation models) increases β due to the increase in the number of old stars (which has redder colors), but the effect is small because of the existence of young stars.

4.4 SED fitting

In Bayesian statistics, the posterior probability $p(\theta|\boldsymbol{L})$ of the true values of the model parameters θ given the observations $\boldsymbol{L}$ is proportional to the product of the prior $p(\theta)$ and the likelihood function $p(\boldsymbol{L}|\theta)$.

$$p(\theta|\boldsymbol{L}) \propto p(\theta)p(\boldsymbol{L}|\theta) \tag{4.1}$$

The prior reflects our knowledge of the distribution of the parameters in the absence of the observations L. We use a flat (or uniform) prior for all of our parameters as we do not have any prior information on the expected distribution. Since the interpolated DirtyGrid has uniform resolution in stellar age, star formation rate, and amount of dust, each value of these parameters have equal probability in our prior. The other parameters are discrete and we naturally assign equal probability to them under the flat prior.

4.4.1 1-component fitting

We use θ to denote the set of all 8 input parameters of the DIRTYGrid plus a scaling factor α, represented as a single symbol in the following equations for readability. Assuming that the observational errors follow a Gaussian distribution, the likelihood function is

$$p(\boldsymbol{L}|\theta) \propto \exp(-\chi^2/2) \tag{4.2}$$

$$\chi^2 = \sum_i \frac{(L_{obs,i} - \alpha L_{model,i})^2}{\sigma_i^2} \tag{4.3}$$

where i denotes the ith band and the sum is performed over all observed photometric bands for the galaxy being fit. The number of bands vary from 14 to 20 in this study. Assuming that σ is independent of α, we can obtain the maximum likelihood estimate of α, that we call α_0, by setting the derivative of χ^2 with respect to α to zero.

$$\alpha_0 = (\sum_i \frac{L_{obs,i} L_{model,i}}{\sigma_i^2})/(\sum_i \frac{L_{model,i}^2}{\sigma_i^2}). \tag{4.4}$$

Due to incomplete knowledge of dust and stellar properties and simplified geometries, our models are approximate in nature and we expect them to deviate from the true SEDs for any input parameters. To account for unknown systematic errors in the model and known interpolation errors in our model grid, we add a model uncertainty of 10% of the α-scaled model luminosity to the observation uncertainty, σ_{obs},

in quadrature.

$$\sigma_{model} = 0.1\alpha L_{model} \tag{4.5}$$

$$\sigma^2 = \sigma^2_{obs} + \sigma^2_{model} \tag{4.6}$$

Draine et al. (2007) and Noll et al. (2009b) took a similar approach in their SED fitting of SINGS galaxies and assigned 10% and 5% of the model luminosity to the model uncertainty, respectively.

With the introduction of an α dependence into σ, the maximum likelihood estimate of α no longer has a simple closed form. As a result, we employ an iterative approach to find α_0. Motivated by the fact that good fits require the model SED to be very similar to the observed SED, we initially set $\sigma_{model} = 0.1L_{obs}$ and use Equation 4.4 and Equation 4.6 to derive an approximate value of α_0. With this value, we calculate an approximate value of the model uncertainty σ_{model} using Equation 4.5 and derive an updated estimate on α_0. We iterate until α_0 no longer changes, at which point the equations become self-consistent and α_0 is the maximum likelihood estimate of α. We find that this procedure typically requires only two iterations to converge to within 1% of the true value.

It is useful to note that while Equation 4.6 follows naturally from the assumption that the model uncertainty and the observation uncertainty are independent, the hierarchical Bayesian approach

$$p(\theta|\boldsymbol{L}_{obs}) \propto p(\theta)p(\boldsymbol{L}_{model}|\theta)p(\boldsymbol{L}_{obs}|\boldsymbol{L}_{model}) \tag{4.7}$$

with the same assumptions of Gaussian distribution uncertainties for the two likelihood functions reduces to Equation 4.6 after marginalizing over the "nuisance" parameter $\boldsymbol{L}_{model}$.

The reduced chi-square, as defined by $\chi^2_{\rm red} = \chi^2/d$ where d is the degrees of freedom, is commonly used to assess the goodness of fit and to facilitate model comparison. For models that are linear in terms of its parameters, $d = N - k$, where N is the number of measurements (number of bands for SED fitting), and k is the number of free parameters in the model. A $\chi^2_{\rm red} > 1$ indicates a poor model fit, while a $\chi^2_{\rm red} < 1$ indicates an overfit or an underestimation of the errors. For non-linear models, the $d = N - k$ degrees of freedom determination is mathematically incorrect (Andrae et al., 2010). We use it to obtain an approximate estimate of reduced chi-square due to its widespread use and convenience, but we warn against over-interpreting these values. We further explore the goodness of fit by examining the residuals.

Out of the eight parameters in the DirtyGrid, global and local geometry both describe the spatial relationship between stars and dust. Given that we only have a total of $2 \times 3 = 6$ combination of geometries, we designate geometry as one "free parameter" for the purpose of calculating the reduced chi-square. Together with the scaling factor, we consider that we have eight free parameters and therefore the number of degrees of freedom of $d = N - 8$. The SEDs in our sample of galaxies have 14 to 20 bands, so the degrees of freedom range from 6 to 12.

We fit each of the galaxies in our sample with all ~6 million models in the inter-

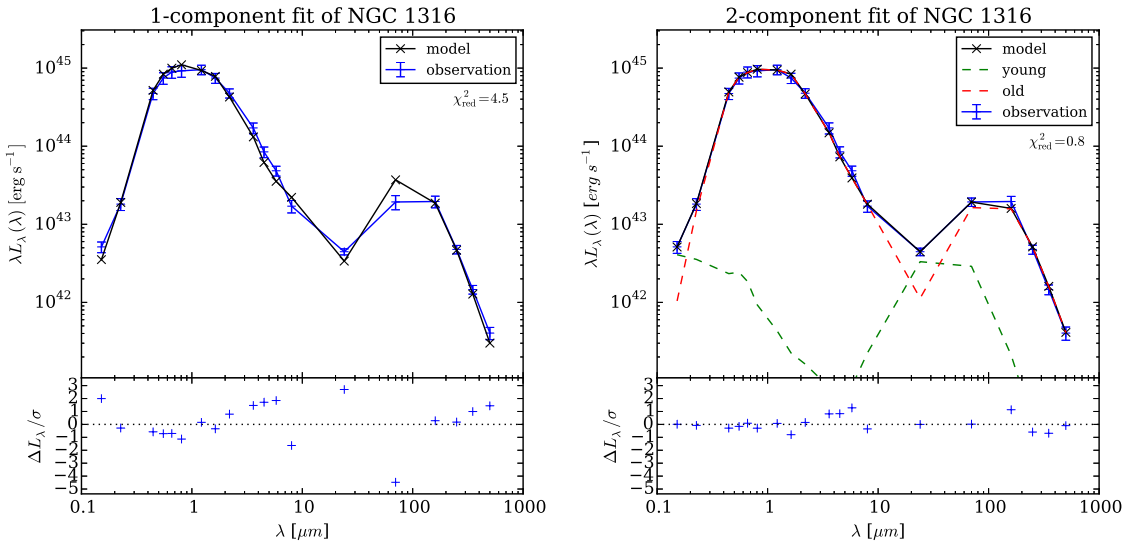

Figure 4.3: Broadband SEDs of the 1-component fit (left) and 2-component fit (right) of NGC 1316. Our best fit 1-component model (a 2.0×10^{12} solar masses starburst of 12 Gyrs age and $Z = 0.004$ metallicity in a 2.8 kpc clumpy shell of LMC type dust and $\tau_V = 0.22$) cannot adequately fit the galaxy. In this galaxy, the low UV to optical ratio requires a very old stellar population, and such a population cannot heat the dust to the temperature needed for the IR observation. The deviation is most visible in the MIPS70 band, where our model significant underestimates the broadband luminosity. In contrast, the 2-component model provides a good fit to the SED.

polated DirtyGrid and found that single models cannot adequately fit most of the galaxies. In terms of reduced chi-square, one galaxy has $\chi^2_{\rm red} \leq 1$ (NGC 3621), five galaxies have $1 < \chi^2_{\rm red} \leq 2$, and the remaining 38 galaxies have $\chi^2_{\rm red} \geq 2$. The median $\chi^2_{\rm red}$ is 4.5. As an example of our 1-component fit, Figure 4.3 shows NGC 1316, a galaxy that has the median $\chi^2_{\rm red}$ in our sample. While the best fit model traces the optical luminosities closely, the deviations are significant in the UV, mid-IR and especially MIPS70. Although there may be models that can separately fit the UV-optical and IR SEDs, the DirtyGrid requires that they are physically connected with dust physics, and in this case no models can satisfy the full UV to IR SEDs.

In Figure 4.4, we show the residuals for the whole sample of galaxies. Our 1-component model systematically underestimates the FUV and MIPS24 and overestimates MIPS70. The distribution of residuals is different from Noll et al. (2009a), whose models tend to overestimate the FUV, underestimate MIPS160, but have no systematic error at MIPS24. The systematic deviations confirm that our 1-component model does not provide adequate fits. This motivates the need for more complex models and these are explored in the next section.

4.4.2 2-component fitting

The result that a single model in the DirtyGrid, with a single description the properties on the stellar population and dust (e.g., such as optical depth) cannot adequately fit whole galaxies is not surprising. It is common for the bulge region of

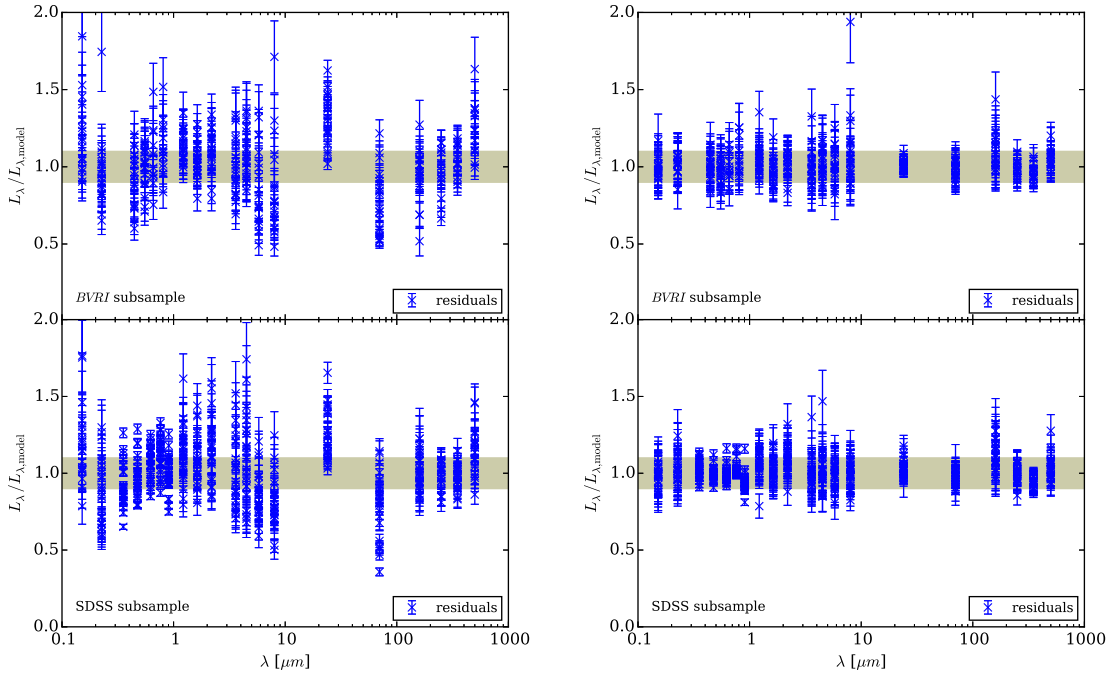

Figure 4.4: Residuals of the SDSS and *BVRI* sub-samples in 1-component fitting (left) and 2-component fitting (right). The shaded area represents the 10% model uncertainty, while each data point and its error bar shows the residual and the data uncertainty for one galaxy, respectively. In 1-component fitting, our models underestimate the FUV, MIPS24 and SPIRE500 luminosities and overestimate the MIPS70 luminosity, and this behavior is similar for both sub-samples. In the *BVRI* subsample, we have larger residuals compared to the SDSS subsample, due to the larger uncertainties in the BVRI data and therefore lower weights in the fits. On the other hands, the SDSS sub-sample has larger residuals in the JHK band than the *BVRI* sub-sample. Adding a second component not only reduces the residuals, but also eliminates the systematic bias. The outlier point in IRAC 8.0 μm belongs to NGC 4236, one of the few galaxies that has a poor fit even in 2-component fitting.

spiral galaxies to have significantly higher fraction of old stars, lower star formation activity, and lower optical depth then the disk region. The simplest model that may be able to capture both the disk and bulge region of a galaxy is a 2-component model that is a linear combination of two DirtyGrid models. Such a model requires two scaling factors and Equation 4.3 becomes

$$\chi^2 = \sum_i \frac{(\alpha L_{\mathrm{model1},i} + \beta L_{\mathrm{model2},i} - L_{\mathrm{obs},i})^2}{\sigma_i^2}. \tag{4.8}$$

If σ does not depend on the two scaling factors α and β, the maximum likelihood estimators of α and β are

$$\begin{pmatrix} \alpha \\ \beta \end{pmatrix} = \frac{1}{ab - c^2} \begin{pmatrix} bd - ce \\ -cd + ae \end{pmatrix} \tag{4.9}$$

where

$$a = \sum_i (\frac{L_{\mathrm{model1},i} \cdot L_{\mathrm{model1},i}}{\sigma_i^2})^2 \tag{4.10}$$

$$b = \sum_i (\frac{L_{\mathrm{model2},i} \cdot L_{\mathrm{model2},i}}{\sigma_i^2})^2 \tag{4.11}$$

$$c = \sum_i (\frac{L_{\mathrm{model1},i} \cdot L_{\mathrm{model2},i}}{\sigma_i^2})^2 \tag{4.12}$$

$$d = \sum_i (\frac{L_{\mathrm{model1},i} \cdot L_{\mathrm{obs},i}}{\sigma_i^2})^2 \tag{4.13}$$

$$e = \sum_i (\frac{L_{\mathrm{model2},i} \cdot L_{\mathrm{obs},i}}{\sigma_i^2})^2 \tag{4.14}$$

Similar to 1-component fitting, we assume a 10% uncertainty in the model fluxes (see Equation 4.6) and iteratively determine α and β. We require that the scaling factors be positive as negative scaling factors would be unphysical.

For the young component, we use a 100 Myr old stellar population with continuous star formation and either the Dusty or the Shell geometry. For the old component, we use an old stellar population (age $>$ 100 Myr) with instantaneous star formation and either the Dusty or the Cloudy geometry. We allow the stellar intensity and the scaling factor of both components to vary independently. We also allow the dust grain type and the stellar metallicity to vary, with the restrictions that the value for both components must be the same. Zoccali et al. (2003) found that the Milky Way bulge is dominated by stars of very similar age ($\gtrsim$ 10 Gyr), so a stellar population with instantaneous star formation for the old component is likely a good approximation. We have found that our SED fitting is not very sensitive to the stellar age of the young component, so we fix the young component to a reasonable age to make the 2-component fitting tractable. The choice of 100 Myr as the dividing age is due to two related reasons, (1) beyond this age, the stellar population no longer generates a significant amount of UV photons, which would be strongly absorbed by dust, and (2) the young population traced by many star formation rate indicators includes contributions from stars $\lesssim$ 100 Myr, and this definition of "young" allows a direct comparison of our fitting results with these indicators.

Using the 2-component model, we obtain satisfactory fits for most galaxies. Figure 4.3 shows the model fit of NGC 1316 with two components. The FUV and MIPS70 discrepancies seen in the 1-component fitting largely vanish. Figure 4.4 shows the residuals for the whole sample. Not only are the residuals smaller, but the systematic

offsets are also within uncertainties. The best fit parameters are given in Table 4.1. Parameters derived from the probability distributions are given in Table 4.2. The small values of reduced chi-square and the lack of systematic errors shows that our 2-component model is a good model for the SINGS galaxies.

In general, the young component dominates the UV and mid-IR (around 24 μm), and the old component dominates the optical, near-IR and sub-mm. The extent to which the far-IR is due to the young component varies between galaxies. However, for some galaxies there are acceptable fits that attribute the majority of the far-IR/sub-mm emission to either the young or the old component (but not both; i.e. a bi-modal behavior).

In order for the young component to fit the mid-IR, the radiation intensity and therefore the average dust temperature needs to be high. In the absence of diffuse dust at a distance from the Shell and Dusty geometries, the young component typically cannot simultaneously produce hot dust emission in the mid-IR and cool dust emission in the far-IR. When the majority of far-IR is attributed to the old component, it requires a high optical depth for the old component, higher than that of the young component. This contradicts the usual understanding in which old stellar populations are less embedded in the interstellar medium then the young populations. In the disc, the scale height of old stars is typically higher than young stars, and in the central region, the old star dominated bulge extends to larger distances from the mid-plane. The result that in some galaxies, most of the far-IR emission comes from the old

component stems from the fact that the two components are separate and the young stars do not heat diffuse dust in our simple 2-component model. We further explore the relative fraction of luminosity from the two components in § 4.5.4.

4.5 Analysis and discussion

4.5.1 Dust masses

We derived dust mass estimates for our sample galaxies from the DirtyGrid 2-component fits. In Figure 4.5, we compare our dust masses to those derived by Draine et al. (2007). We remove 3 galaxies from our sample that are poorly fit ($\chi^2_{\rm red} >= 2$). The remaining 41 galaxies all have good fits from Draine et al. (2007). NGC 1705 has a large uncertainty in the dust mass because a wide range of different parameters can produce acceptable fits. Other than the two data points with $\log(M_{\rm dust}/M_{\odot}) < 5$ in their paper, the dust masses generally agree to within 0.3 dex (a factor of 2). This shows that our 2-component fits give dust masses that are in agreement with previous IR only fits.

In their model, Draine et al. (2007) have a power law (PDR component) plus delta function (diffuse component) distribution of radiation intensity for dust heating. As our work and that of Draine et al. (2007) look at the same sample of galaxies with the same underlying dust grain model, the comparison between the two provides a good illustration of the impact of including dust radiative transfer effects on estimated

Table 4.1: Best fit model parameters. Star formation rate surface density $\sigma_{\rm SFR}$ is in units of $M_\odot {\rm yr}^{-1}{\rm kpc}^{-2}$, stellar mass surface density $\sigma_{\rm M}$ is in $M_\odot {\rm kpc}^{-2}$, and age is in Myr.

	Young component				Old component					Dust		
Galaxy	$\tau_{V,\rm ext}$	$\sigma_{\rm SFR}$	scale	geometry	age	$\tau_{V,\rm ext}$	σ_M	scale	geometry	type	Metallicity	$\chi^2_{\rm red}$
IC 2574	0.10	5.0E−03	9.7E−02	clumpy/dusty	680	1.21	1.0E+08	3.8E+00	clumpy/dusty	SMC	0.02	2.4
Mrk 33	0.56	8.9E−01	3.2E−03	homo./dusty	5600	10.00	3.2E+10	4.6E−01	homo./dusty	LMC	0.004	1.4
NGC 0024	0.18	5.0E−04	1.3E+00	homo./shell	6800	3.83	1.8E+08	4.1E+01	clumpy/cloudy	LMC	0.004	1.0
NGC 0925	0.18	2.8E−03	2.1E+00	clumpy/shell	1000	10.00	3.2E+08	3.1E+01	clumpy/cloudy	LMC	0.02	0.6
NGC 1097	1.78	1.6E−01	1.6E−01	clumpy/dusty	1200	4.64	1.0E+09	9.8E+01	clumpy/dusty	LMC	0.02	0.4
NGC 1291	0.32	5.0E−02	1.8E−02	homo./dusty	5600	0.32	1.0E+09	1.6E+02	homo./dusty	SMC	0.02	0.5
NGC 1316	0.26	1.6E+00	1.3E−03	homo./dusty	2600	0.18	3.2E+09	2.5E+02	clumpy/dusty	SMC	0.02	0.8
NGC 1482	4.64	1.6E−02	1.6E+00	homo./shell	150	10.00	5.7E+08	9.6E+00	homo./dusty	LMC	0.1	0.7
NGC 1512	0.26	1.6E−03	1.4E+00	homo./shell	2600	1.47	3.2E+08	6.9E+01	clumpy/dusty	LMC	0.02	0.3
NGC 1566	0.46	5.0E−02	4.3E−01	clumpy/dusty	830	2.61	1.8E+08	3.9E+02	homo./dusty	MW	0.02	0.2
NGC 1705	0.10	1.6E−03	2.7E−01	clumpy/dusty	680	2.15	5.7E+05	3.5E+02	homo./dusty	SMC	0.02	1.4
NGC 2798	5.62	8.9E−02	1.6E−01	clumpy/shell	3800	10.00	1.0E+10	5.0E+00	homo./dusty	LMC	0.004	0.8
NGC 2841	1.78	8.9E−05	5.3E+01	homo./dusty	8300	0.56	3.2E+09	4.1E+01	clumpy/cloudy	LMC	0.02	0.9
NGC 2915	0.10	2.8E−03	3.4E−02	clumpy/dusty	1200	0.26	5.7E+07	1.9E+00	homo./dusty	SMC	0.02	1.3
NGC 2976	0.38	2.8E−03	1.7E−01	homo./shell	1000	2.61	5.7E+08	2.9E+00	homo./dusty	LMC	0.02	0.3
NGC 3031	0.68	1.6E−04	2.5E+01	homo./dusty	3200	1.00	3.2E+08	2.2E+02	homo./cloudy	LMC	0.02	0.2
NGC 3184	1.21	8.9E−05	6.5E+01	clumpy/dusty	1200	1.00	3.2E+10	2.8E−01	homo./dusty	LMC	0.02	0.7
NGC 3190	10.00	5.0E−04	6.5E+00	homo./dusty	1000	1.78	3.2E+10	7.6E−01	homo./cloudy	LMC	0.1	0.6
NGC 3198	0.26	1.6E−02	1.8E−01	homo./shell	1000	5.62	1.8E+08	4.7E+01	homo./cloudy	MW	0.02	0.9
NGC 3351	0.56	2.8E−02	1.2E−01	clumpy/shell	2200	3.16	1.8E+09	1.9E+01	clumpy/dusty	LMC	0.02	0.5
NGC 3521	3.83	1.6E−04	9.0E+01	homo./dusty	1200	1.21	3.2E+10	1.2E+00	homo./dusty	MW	0.02	1.0
NGC 3621	0.83	1.6E−02	3.0E−01	clumpy/dusty	830	2.61	1.8E+08	5.9E+01	clumpy/dusty	MW	0.02	0.7
NGC 3627	0.83	8.9E−03	1.2E+00	homo./shell	1200	8.25	5.7E+08	7.1E+01	homo./cloudy	MW	0.02	0.9
NGC 3773	0.15	1.6E−02	4.9E−02	clumpy/shell	1000	4.64	1.8E+09	6.0E−01	clumpy/dusty	LMC	0.02	1.0
NGC 4236	0.12	5.0E−03	1.5E−01	homo./dusty	830	0.68	5.7E+07	1.7E+01	homo./dusty	SMC	0.02	3.8
NGC 4536	0.56	8.9E−02	2.7E−01	homo./shell	1000	4.64	5.7E+08	1.4E+02	clumpy/dusty	MW	0.02	0.6
NGC 4559	0.18	8.9E−03	7.2E−01	clumpy/shell	1500	8.25	3.2E+08	5.2E+01	clumpy/cloudy	MW	0.004	0.5
NGC 4569	0.56	1.6E−02	4.9E−01	homo./shell	1200	3.16	5.7E+08	1.5E+02	clumpy/cloudy	LMC	0.02	0.9
NGC 4579	0.38	8.9E−03	5.4E−01	homo./shell	2600	1.21	1.0E+09	1.9E+02	homo./dusty	LMC	0.02	0.8
NGC 4594	0.38	8.9E−03	1.9E−01	homo./shell	5600	0.32	1.0E+09	6.0E+02	clumpy/dusty	LMC	0.02	0.9
NGC 4625	0.56	5.0E−05	1.5E+01	clumpy/dusty	1200	2.15	3.2E+10	3.3E−02	homo./dusty	LMC	0.02	0.6
NGC 4631	0.38	2.8E−02	3.6E−01	homo./shell	460	8.25	5.7E+08	4.0E+01	clumpy/dusty	MW	0.02	0.9
NGC 4725	1.78	8.9E−05	1.9E+02	clumpy/dusty	5600	0.22	1.8E+09	1.5E+02	clumpy/dusty	LMC	0.02	1.1
NGC 4736	0.46	8.9E−03	3.7E−01	homo./shell	1200	1.21	5.7E+08	4.6E+01	homo./dusty	MW	0.02	0.4
NGC 4826	0.68	2.8E−03	6.8E−01	homo./shell	2600	3.16	3.2E+09	1.3E+01	clumpy/cloudy	LMC	0.02	0.5
NGC 5033	1.00	5.0E−03	1.8E+00	clumpy/shell	1200	3.16	1.0E+08	3.1E+02	clumpy/dusty	MW	0.02	0.4
NGC 5055	3.16	2.8E−04	6.9E+01	homo./dusty	3200	0.46	3.2E+10	2.2E+00	clumpy/cloudy	LMC	0.02	0.8
NGC 5194	1.00	8.9E−03	3.0E+00	homo./dusty	1000	5.62	3.2E+07	1.8E+03	homo./dusty	LMC	0.02	0.3
NGC 5195	4.64	1.6E+00	3.1E−04	clumpy/dusty	10000	1.21	1.0E+10	8.3E+00	clumpy/cloudy	MW	0.004	1.5
NGC 5474	0.10	5.0E−06	1.8E+02	homo./dusty	10000	4.64	1.8E+10	3.4E−01	clumpy/cloudy	LMC	0.0001	3.7
NGC 5713	0.46	1.6E+00	5.4E−03	homo./shell	1200	8.25	3.2E+09	1.7E+01	homo./dusty	LMC	0.004	0.9
NGC 5866	0.68	1.6E−03	2.2E−01	homo./shell	2600	2.61	3.2E+09	1.6E+01	clumpy/cloudy	LMC	0.02	0.6
NGC 7331	1.78	5.0E−03	5.0E+00	clumpy/shell	1200	3.16	5.7E+08	1.9E+02	homo./dusty	LMC	0.02	0.4
NGC 7552	3.83	8.9E−01	3.8E−02	homo./dusty	830	10.00	3.2E+09	2.4E+01	homo./dusty	LMC	0.02	0.4

Table 4.2: Properties derived from the probability distributions. We omit the results for 3 galaxies with $\chi^2_{\rm red} > 2$. The central value is the 50th percentile and the uncertainty values are half of the difference between 84th and the 16th percentiles.

Galaxy	log(SFR) $M_\odot$/yr	log($M_{\rm star}$) $M_\odot$	log($M_{\rm dust}$) $M_\odot$	log($\tau_{\rm V,att}$) young	log($\tau_{\rm V,att}$) old
Mrk 33	-0.24 ± 0.04	10.08 ± 0.20	6.28 ± 0.13	0.09 ± 1.29	1.30 ± 1.01
NGC 0024	-0.88 ± 0.06	9.78 ± 0.23	6.98 ± 0.65	0.05 ± 1.30	0.20 ± 1.58
NGC 0925	0.03 ± 0.07	10.19 ± 0.29	7.74 ± 0.11	0.05 ± 1.32	0.35 ± 1.25
NGC 1097	0.68 ± 0.12	11.20 ± 0.24	8.25 ± 0.08	0.23 ± 1.57	0.64 ± 1.22
NGC 1291	-0.82 ± 0.09	11.14 ± 0.17	7.30 ± 0.08	0.04 ± 1.81	0.07 ± 1.12
NGC 1316	-0.29 ± 0.14	11.91 ± 0.04	7.31 ± 0.08	0.08 ± 1.89	0.03 ± 1.11
NGC 1482	0.77 ± 0.09	9.72 ± 0.17	7.60 ± 0.08	2.18 ± 1.60	1.16 ± 1.23
NGC 1512	-0.32 ± 0.11	10.32 ± 0.18	7.54 ± 0.11	0.09 ± 1.50	0.22 ± 1.65
NGC 1566	0.71 ± 0.12	10.94 ± 0.25	8.54 ± 0.38	0.11 ± 1.62	0.54 ± 1.24
NGC 1705	-1.09 ± 0.07	8.48 ± 0.36	7.68 ± 1.72	0.02 ± 1.20	0.14 ± 3.46
NGC 2798	0.50 ± 0.11	10.57 ± 0.27	7.30 ± 0.07	1.30 ± 1.13	1.29 ± 1.15
NGC 2841	-0.03 ± 0.05	11.00 ± 0.12	7.61 ± 0.09	0.34 ± 1.57	0.03 ± 2.12
NGC 2915	-2.58 ± 0.62	7.71 ± 0.32	5.31 ± 0.20	0.06 ± 6.92	0.04 ± 1.42
NGC 2976	-1.09 ± 0.17	9.30 ± 0.23	6.48 ± 0.09	0.15 ± 1.74	0.41 ± 1.32
NGC 3031	-0.13 ± 0.09	10.86 ± 0.08	7.83 ± 0.44	0.11 ± 1.57	0.10 ± 1.70
NGC 3184	0.10 ± 0.04	10.17 ± 0.15	7.40 ± 0.10	0.20 ± 1.32	0.03 ± 2.68
NGC 3190	-0.24 ± 0.35	10.36 ± 0.04	7.39 ± 0.11	1.25 ± 1.78	0.18 ± 2.65
NGC 3198	-0.27 ± 0.08	9.93 ± 0.17	7.47 ± 0.08	0.10 ± 1.60	0.41 ± 1.15
NGC 3351	-0.22 ± 0.12	10.52 ± 0.20	7.36 ± 0.08	0.15 ± 1.61	0.43 ± 1.24
NGC 3521	0.58 ± 0.10	10.88 ± 0.22	7.92 ± 0.14	0.71 ± 1.18	0.04 ± 4.46
NGC 3621	0.21 ± 0.04	10.16 ± 0.25	7.49 ± 0.15	0.18 ± 1.30	0.05 ± 3.74
NGC 3627	0.37 ± 0.16	10.66 ± 0.12	7.76 ± 0.09	0.42 ± 1.65	0.44 ± 1.34
NGC 3773	-0.87 ± 0.06	9.28 ± 0.29	5.99 ± 0.09	0.03 ± 1.53	0.61 ± 1.28
NGC 4536	0.69 ± 0.15	10.91 ± 0.12	8.18 ± 0.07	0.25 ± 1.46	0.82 ± 1.14
NGC 4559	0.17 ± 0.09	10.28 ± 0.21	7.69 ± 0.08	0.06 ± 1.46	0.38 ± 1.40
NGC 4569	0.14 ± 0.14	10.96 ± 0.13	7.92 ± 0.09	0.23 ± 1.69	0.21 ± 1.14
NGC 4579	-0.09 ± 0.34	11.25 ± 0.09	7.89 ± 0.09	0.14 ± 2.89	0.20 ± 2.58
NGC 4594	-0.59 ± 0.32	11.80 ± 0.12	7.83 ± 0.09	0.12 ± 2.83	0.05 ± 1.45
NGC 4625	-0.76 ± 0.07	9.36 ± 0.19	6.56 ± 0.26	0.10 ± 1.30	0.09 ± 4.20
NGC 4631	0.09 ± 0.29	10.14 ± 0.18	7.85 ± 0.09	0.20 ± 2.58	0.91 ± 1.25
NGC 4725	0.51 ± 0.05	11.41 ± 0.15	8.15 ± 0.09	0.25 ± 1.36	0.03 ± 1.96
NGC 4736	-0.10 ± 0.18	10.59 ± 0.16	7.13 ± 0.08	0.24 ± 1.68	0.27 ± 1.56
NGC 4826	-0.67 ± 0.24	10.44 ± 0.19	6.86 ± 0.09	0.22 ± 2.45	0.25 ± 1.23
NGC 5033	0.40 ± 0.12	10.74 ± 0.26	8.60 ± 0.56	0.43 ± 1.42	0.48 ± 1.86
NGC 5055	0.59 ± 0.03	10.86 ± 0.11	7.90 ± 0.08	0.53 ± 1.09	0.04 ± 2.87
NGC 5194	0.72 ± 0.14	10.80 ± 0.21	8.91 ± 0.53	0.17 ± 1.65	0.71 ± 1.66
NGC 5195	-0.99 ± 0.14	10.86 ± 0.23	6.07 ± 0.28	0.35 ± 2.28	0.14 ± 1.28
NGC 5713	0.36 ± 0.14	10.91 ± 0.32	7.74 ± 0.07	0.29 ± 1.75	1.01 ± 1.12
NGC 5866	-1.55 ± 0.29	10.69 ± 0.05	6.84 ± 0.08	0.11 ± 3.41	0.20 ± 1.08
NGC 7331	0.96 ± 0.15	11.37 ± 0.19	8.33 ± 0.12	0.81 ± 1.22	0.13 ± 4.34
NGC 7552	0.86 ± 0.15	11.11 ± 0.31	8.04 ± 0.32	0.72 ± 1.38	1.17 ± 1.15

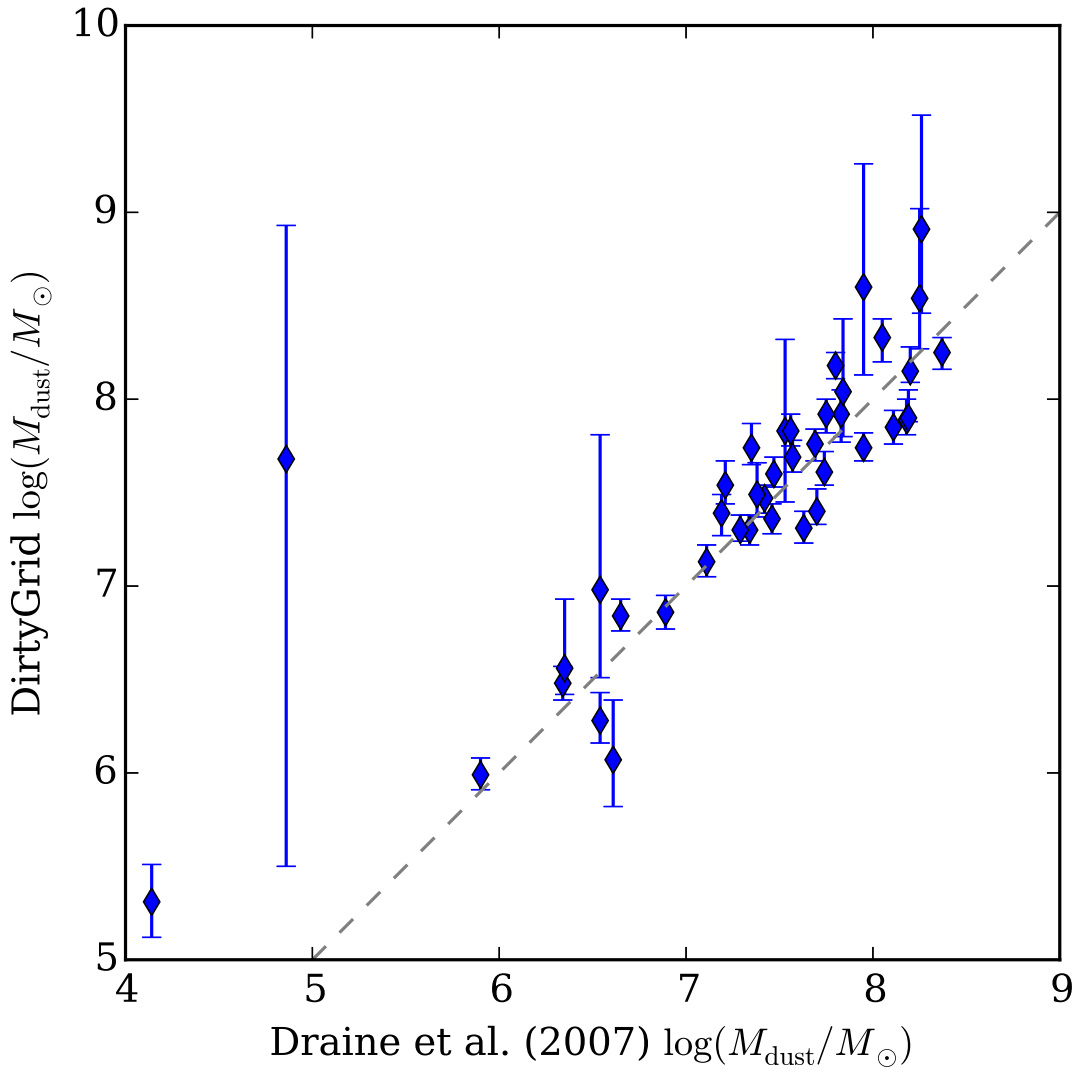

Figure 4.5: Dust mass estimates from DIRTYGrid 2-component SED fitting compared to the ones in Drain et al. (2007). The central value is the 50th percentile in the probability distribution, and the error bars show the 16th and 84th percentile values. The two outliers with x-values less than 5 are NGC 2915 (leftmost) and NGC 1705.

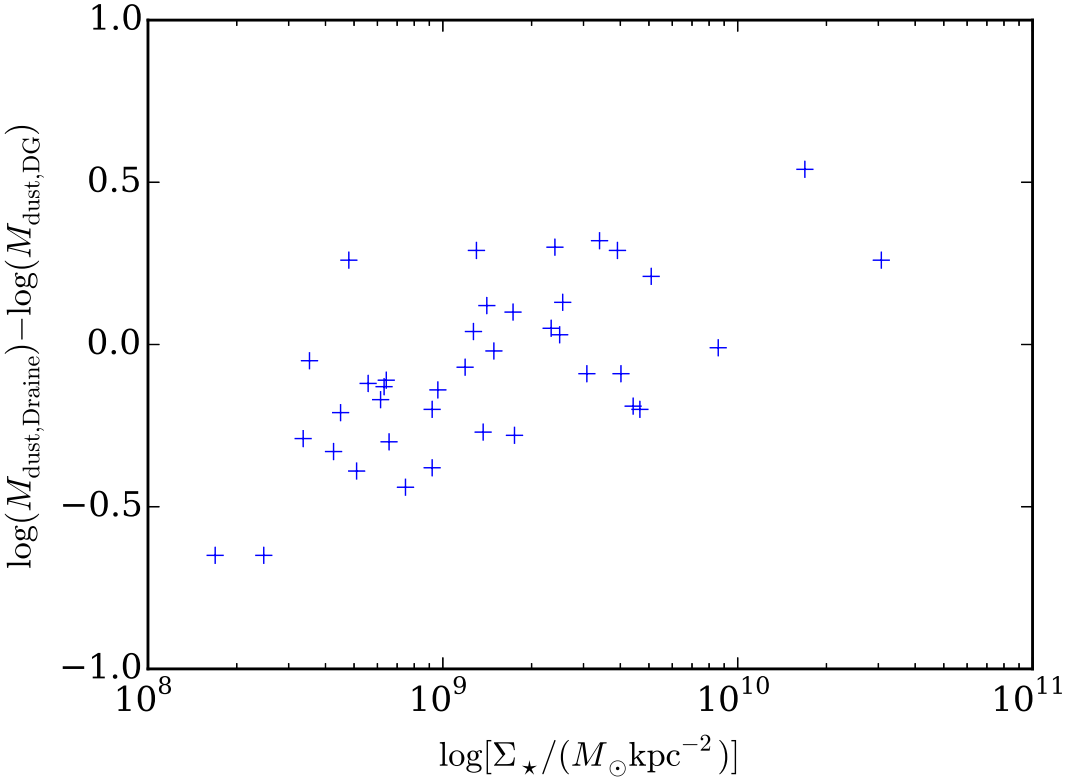

Figure 4.6: Dust mass residuals vs stellar mass surface density. While a correlation is evident in this plot, there is no clear correlation between dust mass residuals and total stellar mass.

dust masses. In the Draine et al. (2007) work, the wavelength dependence of the radiation field is taken from the solar neighborhood. In contrast, we allow the age and metallicity of the stellar population to vary (which changes the radiation hardness), and the use of radiative transfer in a 3D geometry results in dust at different locations in the model space being exposed to different radiation field intensities. The residual dust mass, defined as the surplus dust mass in their model compared to ours, correlates positively with the stellar mass surface density of the old component (Figure 4.6). The diffuse radiation intensity in their model determines a single dust temperature for the diffuse component, which is also the lowest dust temperature in their model. Given the range of radiation fields, it is likely that our old component has dust grains that are hotter and cooler than their diffuse dust temperature for the same galaxy, which is more realistic. This indicates that more accurate dust masses are likely derived using the full UV to IR SED and including radiative transfer effects.

4.5.2 Dust type

By marginalizing over all parameters other than dust grain type, we obtain a probability of the type of dust grains for each galaxy. We present the results in Table 4.3. We find that these normal star forming galaxies are best described by the LMC 2 type dust, which has 2175 Å bump and far-UV rise strengths intermediate between that of MW and SMC type dust. Disregarding the galaxies with poor fits ($\chi^2_{\rm red} > 2$), only 4 of the galaxies in our sample has significant probability ($> 1/3$)

Table 4.3: Posterior probability of each grain type. We omit the results for 3 galaxies with $\chi^2_{\rm red} > 2$.

Galaxy	MW	LMC	SMC
Mrk 33	0.00	1.00	0.00
NGC 0024	0.07	0.93	0.00
NGC 0925	0.25	0.75	0.00
NGC 1097	0.51	0.49	0.00
NGC 1291	0.17	0.38	0.45
NGC 1316	0.09	0.19	0.72
NGC 1482	0.10	0.90	0.00
NGC 1512	0.27	0.73	0.00
NGC 1566	0.50	0.50	0.00
NGC 1705	0.00	0.00	1.00
NGC 2798	0.12	0.88	0.00
NGC 2841	0.03	0.97	0.00
NGC 2915	0.00	0.00	1.00
NGC 2976	0.41	0.59	0.00
NGC 3031	0.14	0.86	0.00
NGC 3184	0.03	0.97	0.00
NGC 3190	0.17	0.83	0.00
NGC 3198	0.80	0.20	0.00
NGC 3351	0.36	0.64	0.00
NGC 3521	0.26	0.74	0.00
NGC 3621	0.09	0.91	0.00
NGC 3627	0.48	0.52	0.00
NGC 3773	0.28	0.72	0.00
NGC 4536	0.69	0.31	0.00
NGC 4559	0.45	0.55	0.00
NGC 4569	0.28	0.72	0.00
NGC 4579	0.19	0.81	0.00
NGC 4594	0.19	0.65	0.16
NGC 4625	0.12	0.88	0.00
NGC 4631	0.56	0.44	0.00
NGC 4725	0.04	0.96	0.00
NGC 4736	0.57	0.43	0.00
NGC 4826	0.32	0.68	0.00
NGC 5033	0.32	0.68	0.00
NGC 5055	0.04	0.96	0.00
NGC 5194	0.19	0.81	0.00
NGC 5195	0.49	0.51	0.00
NGC 5713	0.20	0.80	0.00
NGC 5866	0.16	0.83	0.01
NGC 7331	0.12	0.88	0.00
NGC 7552	0.08	0.92	0.00

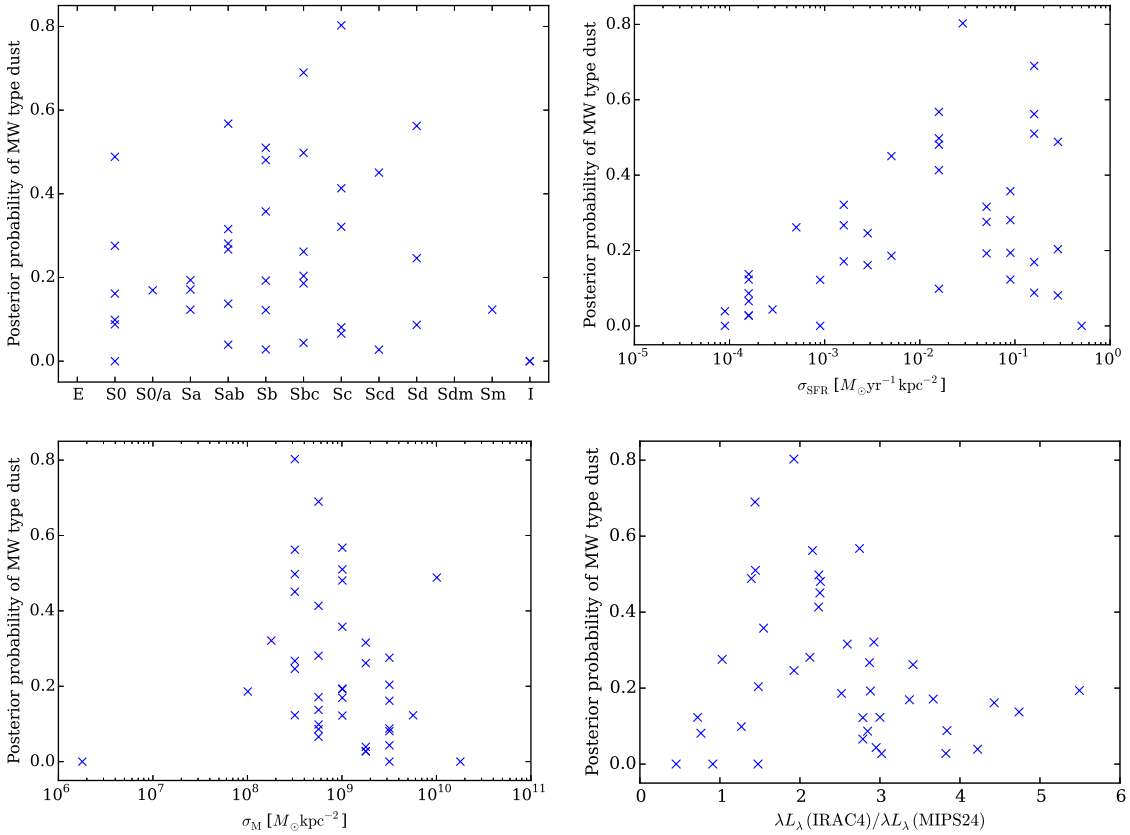

Figure 4.7: Posterior probability of MW type dust vs optical morphology (top left), star formation rate surface density ($\sigma_{\rm SFR}$) of the young component (top right), stellar mass surface density ($\sigma_{\rm M}$) of the old component (bottom left), and 8 μm to 24 μm luminosity ratio (bottom right).

in SMC type dust, two of which (NGC 1705 and 2915) have the probability of unity. This is different from starburst galaxies which are best described by the SMC type dust (Gordon et al., 1997).

We find that the dust grain type is correlated with both global environment and local conditions. We use the probability of MW dust grain, P(MW), as a rough, single-number quantifier of dust grain properties. For many galaxies, $1 - P({\rm MW}) = P({\rm LMC})$. Figure 4.7 shows P(MW) versus optical morphology, stellar surface densi-

ties, and IRAC4/MIPS24 color ratio.

Early type spiral galaxies (towards S0) have smooth spiral arms and prominent central bulges, while late type ones (towards Sm) have distinctive spiral arms and weak bulges. We find a weak increasing trend of P(MW) from S0 to around Sb-Sc, where it peaks. The number of galaxies in our sample beyond Sc type is small, but P(MW) appears to decrease towards the later types. This behavior is similar to Figure 5 in Dale et al. (2007), which shows that the IR to UV ratio peaks around Sb type. Although uncertain, the Milky Way galaxy is also classified as a Sb galaxy.

A stronger trend can be seen in the plots of P(MW) against star formation rate surface density ($\sigma_{\rm SFR}$) of the young component and stellar mass surface density ($\sigma_{\rm M}$) of the old component. P(MW) correlates positively with $\sigma_{\rm SFR}$ and negatively with $\sigma_{\rm M}$. Interestingly, while P(MW) correlates with these surface density quantities, it is not correlated with the total stellar mass. This suggests that P(MW) may be affected by the local radiation field intensity. In addition, we see that high P(MW) only occurs with an intermediate IRAC4/MIPS24 color ratio, which is a rough proxy for the fraction of stochastic small grains emission in relation to hot dust emission.

In their models, Draine et al. (2007) found that the IR SEDs of the SINGS galaxies are best described by the MW type dust. In contrast, we found that the UV to IR SEDs of the same galaxies are best described by the LMC type dust. One possible explanation is that we allow the shape of the UV radiation field to vary based on the stellar population, and this allows a harder UV radiation field than the solar

neighborhood radiation field they used. A harder radiation field can be more efficient in generating mid-IR stochastic dust emission, therefore it does not require the higher PAH mass fraction found in the MW type dust.

4.5.3 Attenuation curves

The attenuation curve describes the wavelength dependence of the combined effects of scattering and absorption in attenuating the stellar emissions. Witt & Gordon (2000) investigated the impact of varying the dust properties on the attenuation curve in galactic environments. In general, the absolute magnitude of attenuation depends on the amount of dust, dust grain properties, and geometry (relative positions of dust and stars). It is customary to normalize the attenuation curve by the opacity at V band, however, the resultant attenuation curve still strongly depends on the amount of dust. Keeping everything else constant, increasing the amount of dust flattens the attenuation curve. SMC type dust has the steepest far-UV rise, following by LMC and MW types. The Shell geometry gives the steepest attenuation curve, following by Dusty and Cloudy. Homogeneous dust also give a steeper attenuation curve then clumpy dust.

The flattening of the attenuation curve due to additional dust can be understood in the following thought experiment. Consider having a star in the center of a sphere such that (1) the left hemisphere of the sphere is vacuum, (2) the right hemisphere is filled with uniform dust, and (3) the optical depth from the center through the

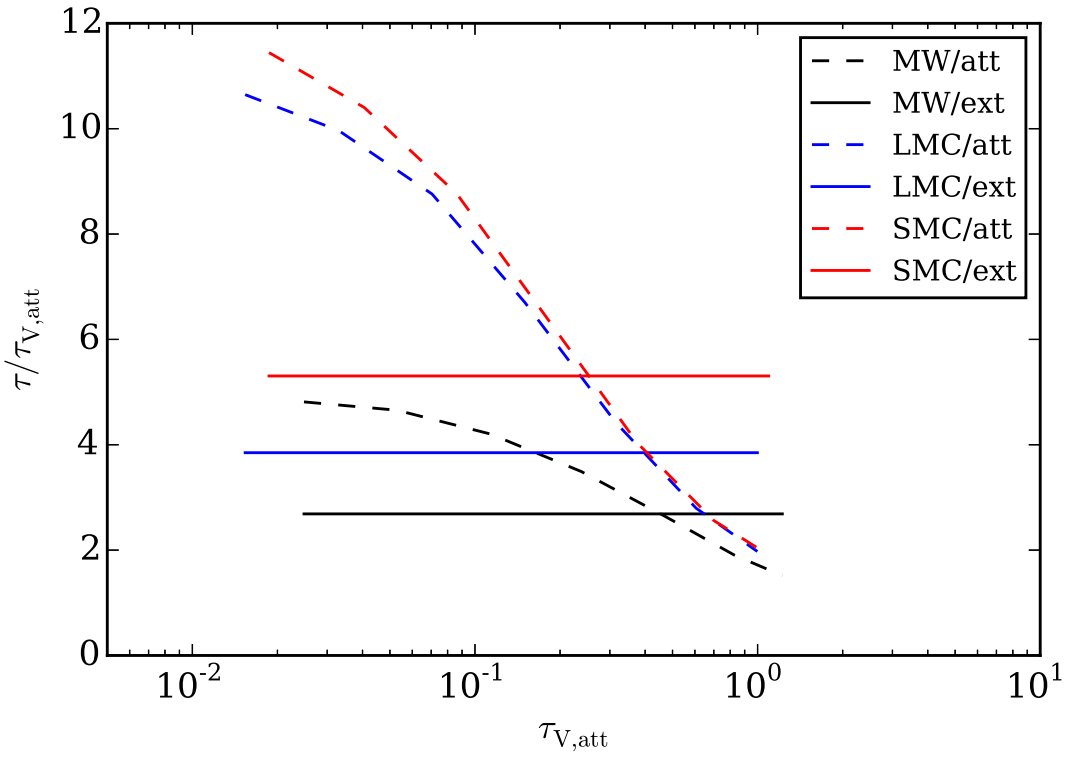

Figure 4.8: $\tau_{\rm FUV}/\tau_{\rm V,att}$ vs $\tau_{\rm V,att}$ for the dusty geometry with clumpy dust (att) or pure extinction without radiative transfer effects (ext). The line color indicates the dust type while the line style distinguishes between the att and ext cases. The CCM relation with $R_V = 3.1$ curve (not shown) is approximately the same as the horizontal "MW/ext" line. In general, as the amount of dust increases, the attenuation in V band increases more rapidly than the attenuation in the UV, causing the ratio to decrease.

right hemisphere is unity at V band. For simplicity, consider a hypothetical dust grain population that has twice the cross section at FUV compared to V band and no scattering. The fraction of photons absorbed by dust is 1/4 at V band and 3/8 at FUV, such that the ratio of optical depths is $\log(1/4)/\log(3/8) = 1.63$. If we double the amount of dust, the fractions become 3/8 at V band and 7/16 at FUV, and the ratio decreases to 1.22. In essence, it is the existence of paths of differential optical depths that makes the growth of attenuation at FUV slower than at V band as we increase the amount of dust. The same logic applies to other UV wavelengths, not just FUV.

To demonstrate radiative transfer effects on dust attenuation in the DIRTYGrid geometries, we plot the $\tau_{\rm FUV,att}/\tau_{\rm V,att}$ ratios as functions of $\tau_{\rm V,att}$ in Figure 4.8 for the Dusty geometry with clumpy dust. As $\tau_{V,att}$ increases from 0.1 to 1.0, $\tau_{\rm FUV,att}/\tau_{\rm V,att}$ decreases from 10 to 2. The convergence of the ratios at high $\tau_{\rm V,att}$ values indicates that the shape of the attenuation curve does not depend on the dust type in the optically thick regime. In that regime, the attenuation curve is relatively flat in the UV. Qualitatively, the same trends hold for all geometries with clumpy dust and for the Cloudy and Dusty geometries with homogeneous dust. They do not hold for the Shell geometry with homogeneous dust, because in such geometry all photons experience similar optical depths and the dispersion only comes from scattering.

Traditionally, the determination of attenuation curves of whole galaxies required comparing the spectra of a dustier galaxy to a less dusty galaxy with the same un-

derlying unreddened spectra. Using this method on the IUE UV and optical spectra of 39 starburst galaxies, Calzetti et al. (1994) derived an average attenuation law for starburst galaxies. The curve is found to be flatter than the MW extinction law and lacks the 2175 Å dust feature. Gordon et al. (2000) presented the flux ratio method to determine Att(λ) from F(IR)/F(λ). However, the flux ratio method is only accurate if the UV through far-IR flux originates from a single stellar population, which can be a good approximation for starburst galaxies but not for normal star forming galaxies. Using SDSS optical spectra, GALEX UV photometry and UKIDSS NIR photometry of a large sample of low-redshift galaxies, Wild et al. (2011) matched galaxy pairs with similar gas-phase metallicity, specific SFR, axial ratio, and redshift to derive attenuation curves. They found the variations in the steepness of the attenuation curve correlates positively with stellar mass surface density. This correlation may share the same origin as the anti-correlation observed between $P(MW)$ and stellar mass surface density in Figure 4.7. With the two GALEX bands in the UV, they also found a discontinuity in the attenuation curve that suggests the existence of the 2175 Å dust feature.

Fitting the UV-IR SED with full radiative transfer models allow us to obtain the attenuation curves without UV spectra as the fitting effectively provides an accurate model of the unreddened galaxy SED. Figure 4.9 shows the average attenuation curve of our entire sample. We calculate the expected value of optical depth at each wavelength for both young and old components of each galaxy. Then we normalize

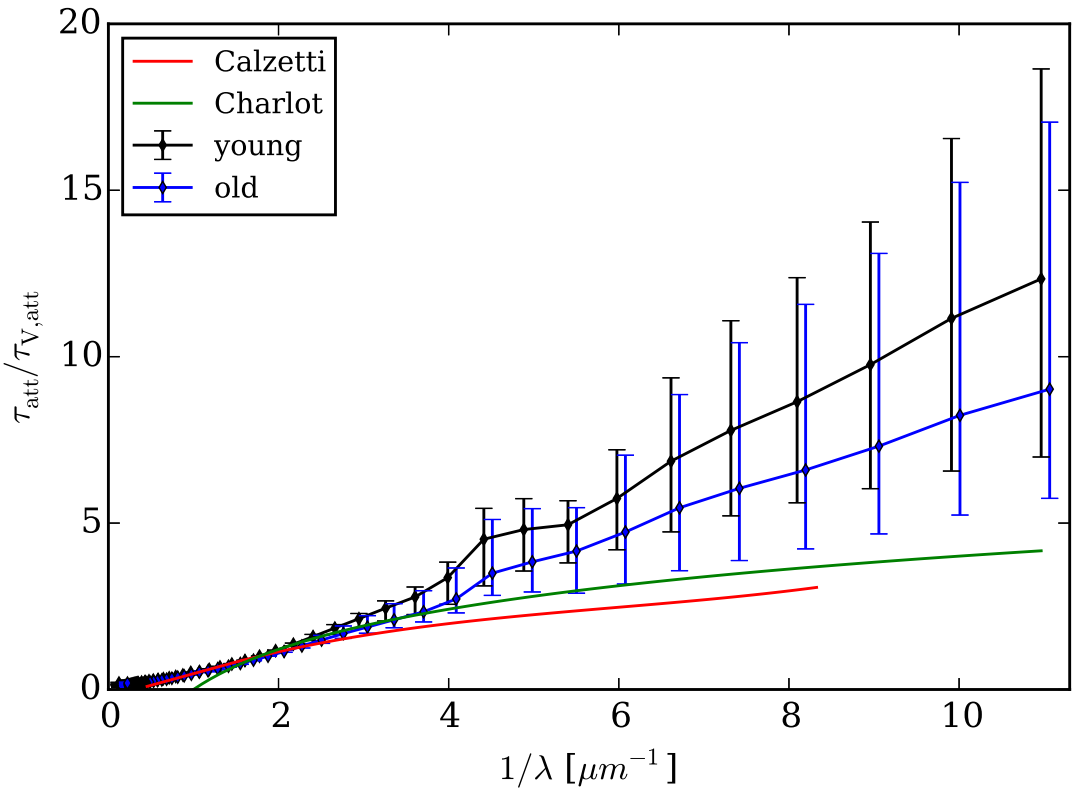

Figure 4.9: Average attenuation curves of our sample compared to the starburst attenuation law presented in Calzetti et al. (2000) and the power law attenuation model used by Charlot & Fall (2000). The values shown are the 16th, 50th and 84th percentile values.

the curve by the optical depth at V band. Finally we find the 16th, 50th and 84th percentile values of the sample at each wavelength. For completeness, we show both components, but at FUV and beyond ($1/\lambda \gtrsim 6$) the young component would dominate the luminosity and so the overall attenuation of the whole galaxies would equal that of the young component.

Our average attenuation curve is steeper than the aforementioned Calzetti starburst attenuation law. Possible contributing factors include a lower attenuation in normal star forming galaxies compared to starburst galaxies, different dust grain properties, and different geometries. Since newly formed stars are more embedded in dust, the high star formation rate in starburst galaxies suggests that the higher optical depth explanation is the most probable.

We found that the attenuation curve of the young component clearly shows the 2175 Å bump feature, while in the old component the bump is very weak. Theoretically, the shape of the attenuation curve depends on dust properties, star-dust geometries, and the optical depth. Based on the understanding that stellar populations become less embedded in dust as they age, we only allow the Cloudy and Dusty geometries for the old component and only the Dusty and Shell geometries for the young component. For the same amount and type of dust, the Cloudy geometry gives the shallowest attenuation curve with the weakest bump, followed by Dusty and then Shell. Assuming that the relative positions of dust and stars in elliptical galaxies are similar to the old component in normal star forming galaxies, we should expect to see

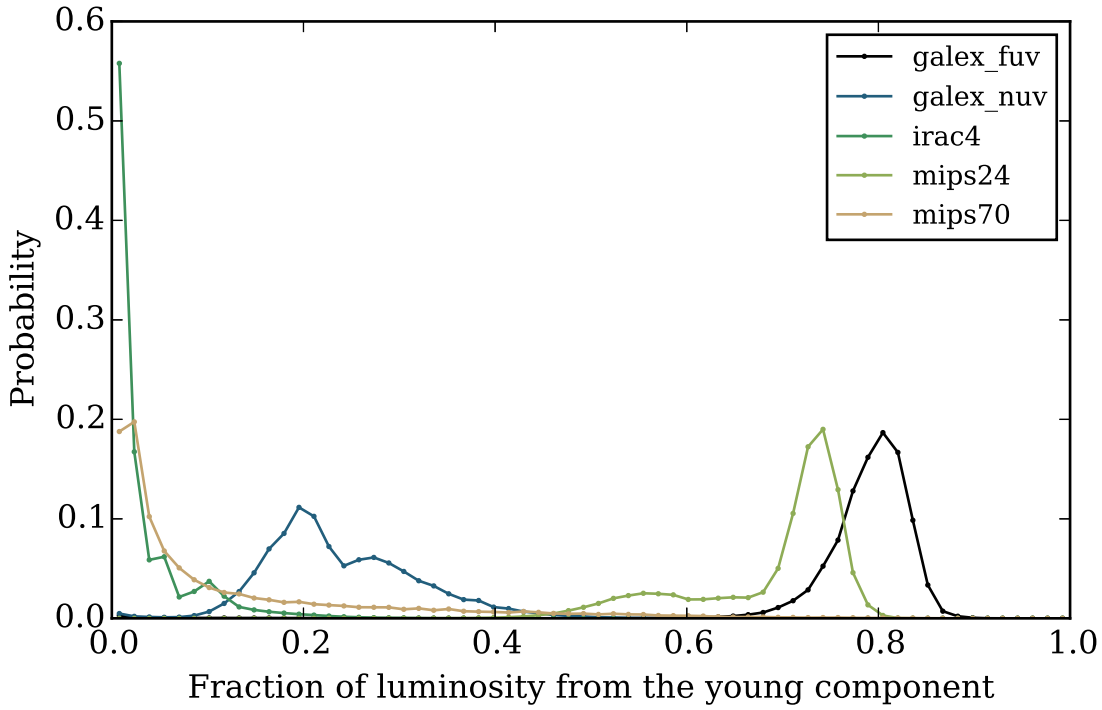

Figure 4.10: Fraction of luminosity from the young component ($F_{\rm young}$) for NGC 1316.

a weak bump in their attenuation curves. The low dust content of elliptical galaxies may make such study challenging but it would be important as it would provide confirmation for this result.

4.5.4 Fraction of luminosity from the young component

The two components have different contributions to the luminosities at different wavelengths. To quantitatively investigate the importance of the two components

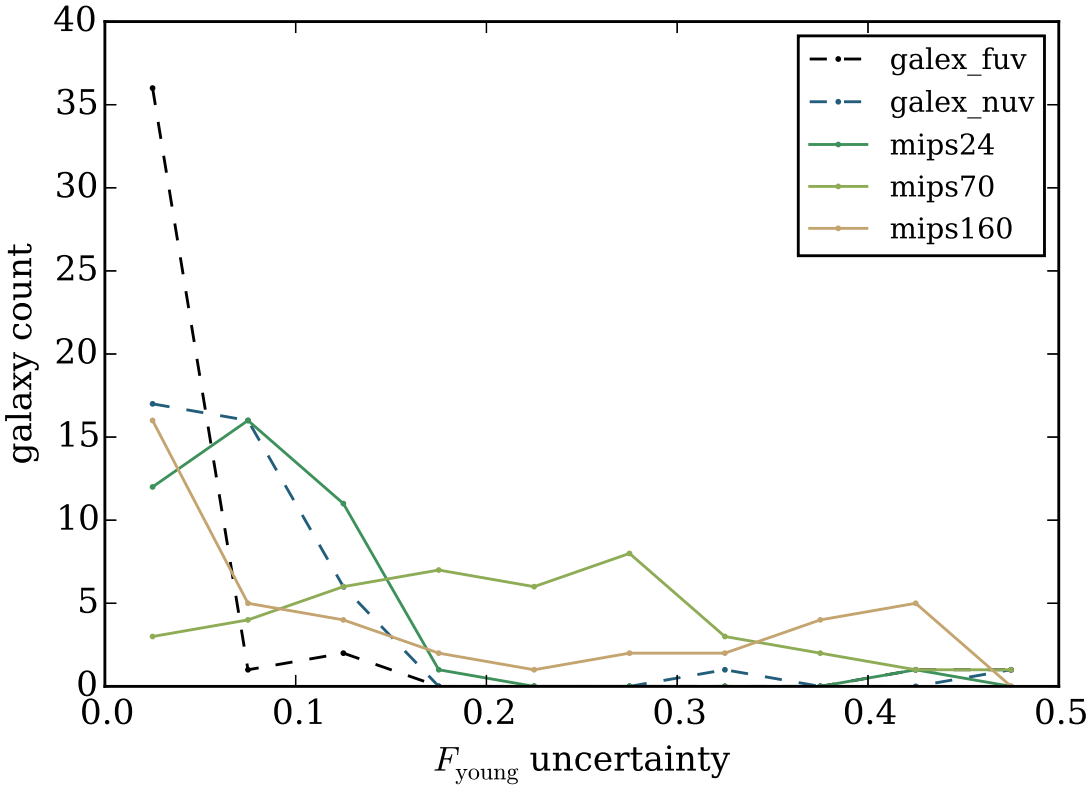

Figure 4.11: Histogram of uncertainties of $F_{\rm young}$ in the UV and far-IR bands. For each galaxy, the uncertainty in the probability distribution of $F_{\rm young}$ is defined as half of the difference between the 84th and 16th percentiles. Given that the full range of $F_{\rm young}$ is from 0 to 1, the large uncertainties in MIPS70 and MIPS160 of many galaxies indicate that we are unable to constrain $F_{\rm young}$ in these two bands.

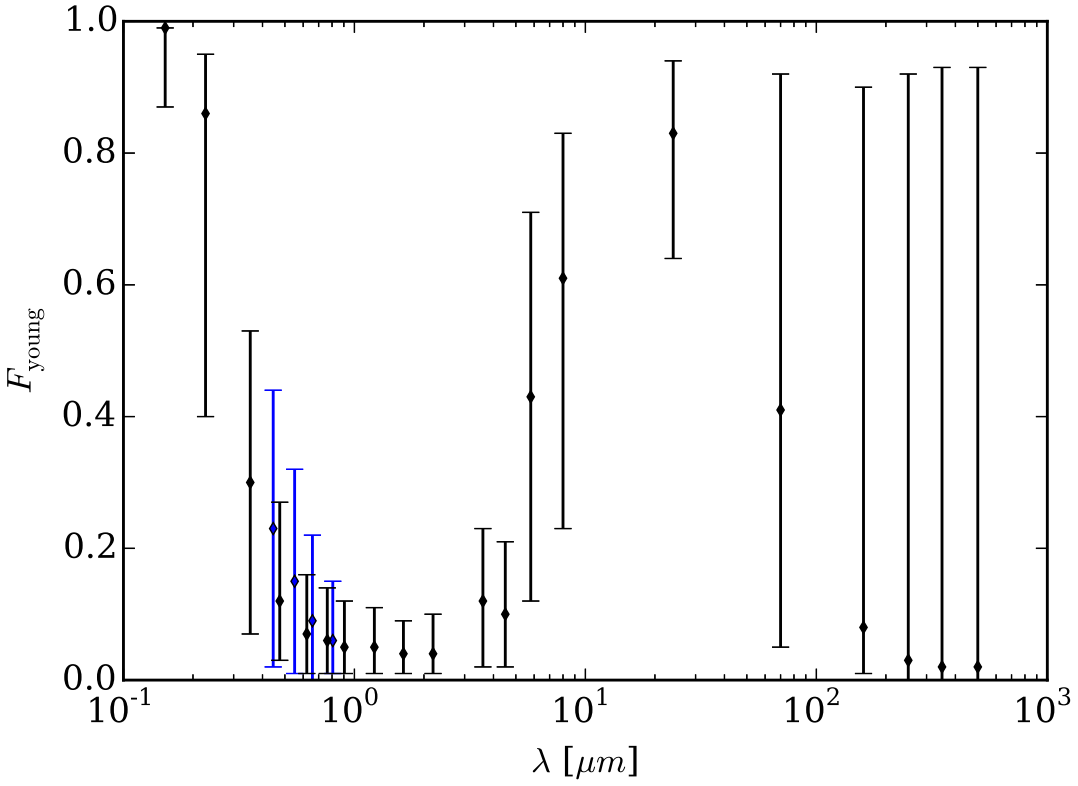

Figure 4.12: Ensemble properties of the fraction of luminosity from the young component ($F_{\rm young}$). The BVRI bands overlap with the SDSS optical bands, so we show the former in blue for clarity. The 16th, 50th and 84th percentiles are shown as the lower error bar, the central value and the upper error bar respectively. The error bars include both uncertainties from individual galaxies and deviation between galaxies.

as a function of wavelength, we calculate the fractional luminosity from the young component $F_{\rm young}$ at in each band. We construct the probability distribution of $F_{\rm young}$ for each band in each galaxy by weighting the 2-component model's $F_{\rm young}$ by the posterior probability. As an example, Figure 4.10 shows the probability distributions of $F_{\rm young}$ for 4 selected bands of NGC 1316. In GALEX FUV, approximately 80% of the luminosity is due to the young component. As we move to the NUV, the fraction drops rapidly to about 20%, but with a larger spread. The optical bands (not shown) are dominated by the old component. In the mid-IR, $F_{\rm young}$ increases towards longer wavelengths. At MIPS24, $F_{\rm young}$ reaches the peak of about 75%, and then it drops back to $< 10\%$ at MIPS70.

In addition to the central value, the uncertainty of $F_{\rm young}$ also changes significantly across bands. In Figure 4.11, we plot the distribution of the uncertainties of our sample of galaxies in 5 selected bands. The uncertainty is defined as half of the difference between the 16th and the 84th percentile values. The maximum value of uncertainty, 0.5, corresponds to the case in which our fitting cannot constrain $F_{\rm young}$ at all. $F_{\rm young}$ is very well constrained in GALEX FUV, and the uncertainty is typically less than 0.05. The uncertainty of $F_{\rm young}$ in MIPS24 is typically around 0.1, and is the lowest among far-IR bands. In contrast, MIPS70 and MIPS160 have widely varying $F_{\rm young}$ uncertainties between 0.0 and 0.5.

To study the ensemble properties of $F_{\rm young}$ in our sample of galaxies, we add the probability distributions of $F_{\rm young}$ across galaxies and normalize the resultant "average

probability distributions" by the number of galaxies. In Figure 4.12, we show the 16th, 50th and 84th percentile values of the average probability distributions at each band. In general, the optical and near-IR are dominated by the old component, while the UV and mid-IR (~24 μm) are dominated by the young component. The near-IR bands have small $F_{\rm young}$ and the lowest scatter across all bands, providing a good constraint on the stellar mass of the old component. The far-IR and sub-mm are much more uncertain, with the 16th to 84th percentile spanning $0\% < F_{\rm young} < 90\%$.

The origin of the stellar component responsible for heating the far-IR and sub-mm emission is more complex. The 50th percentile values of the $F_{\rm young}$ for $\lambda > 100$ μm are very small, but the uncertainty on this value extends almost to $F_{\rm young} = 1$. This indicates that in the majority of our galaxies the old component dominates the heating responsible for the far-IR emission. Yet a fraction of the reasonably fitting models have the young component dominating the heating. In addition, there are galaxies in our sample where the young component clearly dominates the far-IR heating. This result is different from what we found when we used a preliminary version of the DirtyGrid to study the ensemble behavior of the IR to IRAC4 (8 μm) flux ratios of the SINGS galaxies (Law et al., 2011). In that work, we found that young stellar populations (on the order of 100 million years old) dominate dust heating, and old stellar populations (13 billion years old) generally contribute less than 20% of the far-IR luminosity. This result is included in Chapter 2. This illustrates that the answer to which stellar population heats the far-IR dust emission changes depending on the

type of analysis. This is further illustrated by Bendo et al. (2015) who found that the transition wavelength between young star (traced by H-alpha) dominated-heating and old star (traced by IRAC1 3.6 μm) dominated-heating varies between 160 μm and 500 μm in their sample of nearby face-on spiral galaxies, and they were unable to explain the variation with galaxy properties. Thus, the question of which stellar population dominates the far-IR heating does not have a single answer, but likely depends on the detailed evolution of each galaxy.

4.5.5 Star formation rate

Determining the star formation rate in a galaxy is often done using simple prescriptions based on the flux in a single band or combination of two bands (Kennicutt, 1998). Star formation rate (SFR) for a period of time is defined as the sum of the stellar mass of stars that has a lifetime shorter than or equal to that period of time, divided by the length of that period of time. Typical SFR indicators trace the star formation over 100 Myr, with the exception that Hα traces star formation over 10 Myr. By fitting the full UV-IR SED with a young and an old component, our model allows us to decompose the of band integrated luminosity into star-forming and non-star-forming parts. Our choice of a 100 Myr age for the young component facilitates a direct comparison between SFR values recovered from our fitting and the ones provided by literature SFR indicators. The use of constant star formation models for the young component allows us to directly extract the SFR from our composite models.

Many literature SFR indicators use some combination of FUV, NUV, Hα, and IR luminosities (Kennicutt, 1998; Calzetti et al., 2007; Kennicutt et al., 2009; Hao et al., 2011). In normal star forming galaxies, the vast majority of FUV radiation originates from young stars. However, the FUV emission from a galaxy is only a tracer of the un-obscured star formation. In theory, the FUV+TIR SFR indicator can get around the problem of FUV flux lost due to dust attenuation by capturing the re-emitted flux in the infrared. Variations in the conversion factor from luminosities to a star formation rate can happen if: (1) variations in the age and metallicity of the young stellar population change the FUV flux per unit stellar mass; (2) a significant amount of dust emission occurs at a wavelength beyond what is used in the TIR indicator; (3) there is contamination in TIR by stellar radiation; and (4) there is contamination in FUV or TIR by an old stellar population.

For each 2-component model, we calculate the SFR by weighting the product of the SFR surface density and the model surface area by the posterior probability of the model to arrive at a 1D probability distribution of SFR values. In Figure 4.13, we plot our SFR versus the SFR obtained using various SFR recipes in the literature, including ones that uses FUV, NUV, Hα, MIPS24, and TIR. Our SFR values generally match well with others within a factor of 2. We summarize the comparison between our SFR values and the ones obtained from SFR indicator in Table 4.4. After removing two galaxies with extreme values (NGC 2915 and NGC 5866), we perform a least squares fit on the sample. The slope ranges from 0.84 to 0.98, suggesting

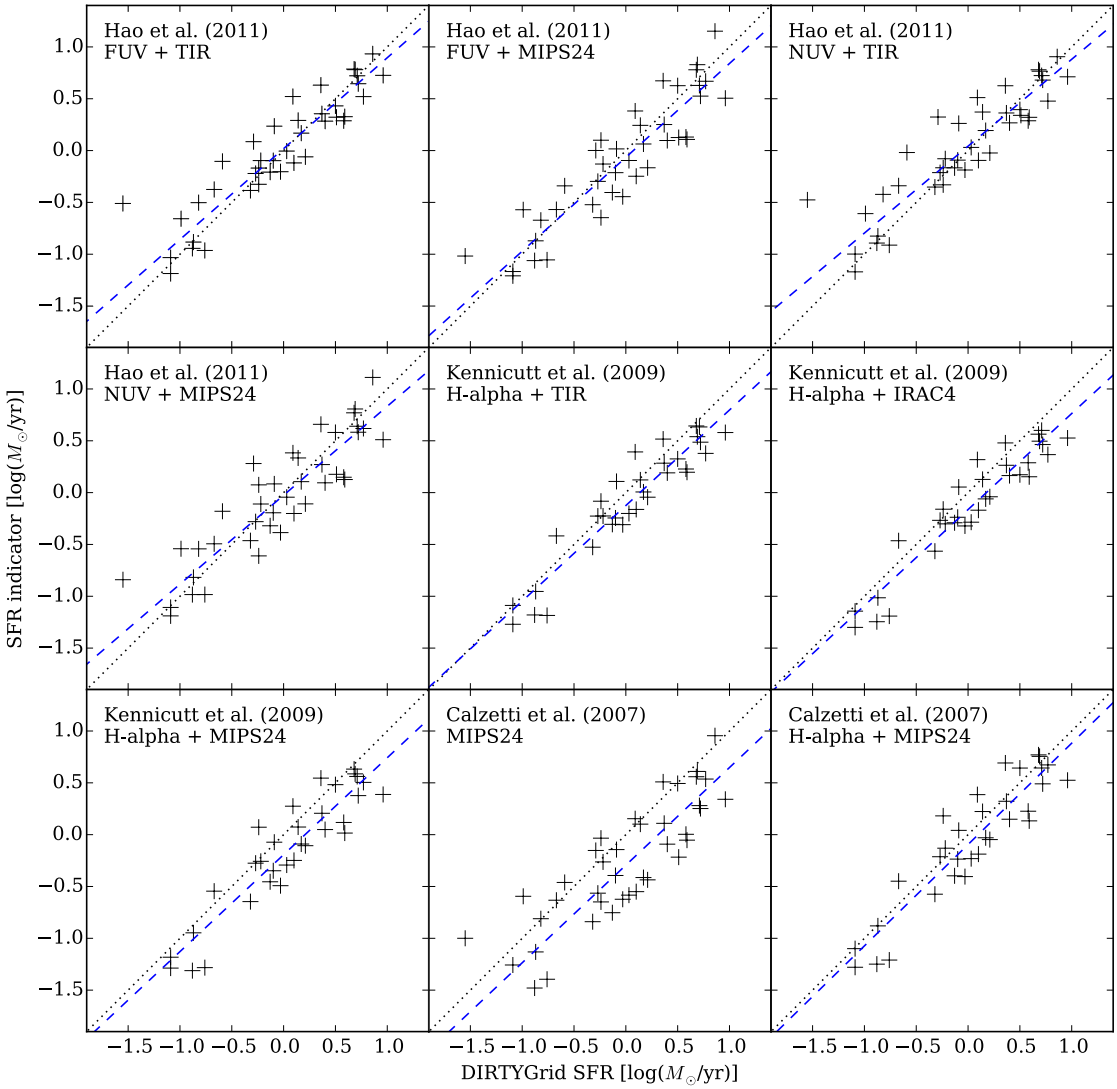

Figure 4.13: Comparison between common SFR indicators and SFR obtained from DirtyGrid SED fitting. The grey dotted line is where the two SFRs equal and the blue solid line is the linear least squares fit of our sample. NGC 2915 (x-value −2.58) and NGC 5866 (x-value −1.55) are excluded from the least squares fit because of their extremely low DirtyGrid SFR values.

Table 4.4: Summary of comparisons between common SFR indicators and DirtyGrid SFR. The last two columns show the slope and the root-mean-squared residual of the least squares fit to the sample, with values obtained from the SFR indicators as y-values and values obtained from our fitting as x-values.

SFR indicator	mean deviation	LSF slope	RMS residual
Hao et al. (2011) FUV + TIR	+0.06	+0.88	0.19
Hao et al. (2011) FUV + MIPS24	−0.03	+0.91	0.25
Hao et al. (2011) NUV + TIR	+0.09	+0.84	0.21
Hao et al. (2011) NUV + MIPS24	+0.01	+0.86	0.25
Kennicutt et al. (2009) Hα + TIR	−0.11	+0.92	0.19
Kennicutt et al. (2009) Hα + IRAC4	−0.14	+0.93	0.18
Kennicutt et al. (2009) Hα + MIPS24	−0.17	+0.94	0.22
Calzetti et al. (2007) MIPS24	−0.27	+0.94	0.32
Calzetti et al. (2007) Hα + MIPS24	−0.08	+0.98	0.24

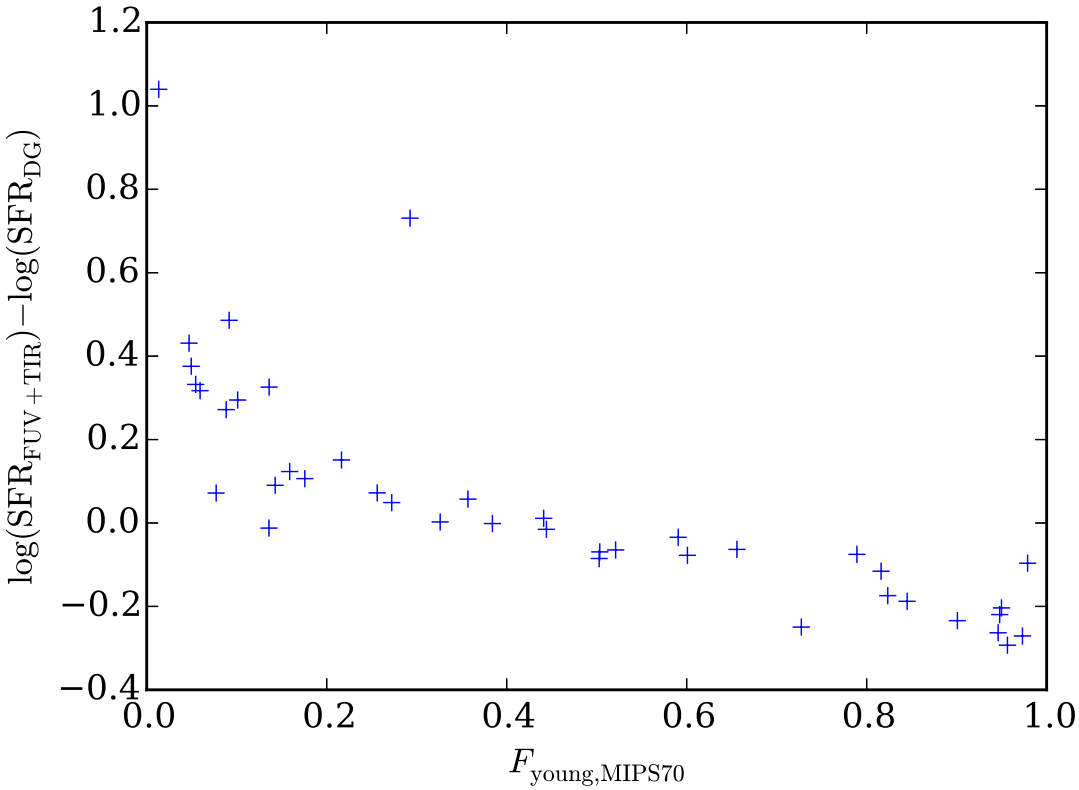

Figure 4.14: SFR residual vs fraction of MIPS70 luminosity from the young component. The SFR residual shown here is the base-10 logarithm of the difference between the SFR obtained from the Hao et al. (2011) FUV + TIR recipe and the DirtyGrid SFR. The residual correlates well with F_{young} in many IR bands, but the visual trend is the most prominent in IRAC4 and MIPS70.

that SFR indicators underestimate the true SFR for high SFR. A possible reason is that at extreme SFR, the dust in the galaxies may emit a significant fraction of the energy in the stochastically heated small grains. These emissions are at a shorter wavelength than the MIPS24 and TIR constituent bands (typically MIPS24, MIPS70 and MIPS160).

We find that the residuals between our SFRs and literature SFRs are strongly

correlated with the fraction of luminosity from the young population. In Figure 4.14, we plot the residual, defined as the literature SFR indicator values minus our SFR values, versus median $F_{\rm young}$ at MIPS70. A similar trend is observed in other IR bands, but it is the most striking in MIPS70 because of the wide range of $F_{\rm young}$ values in this band. Although our $F_{\rm young}$ values may suffer from large uncertainties, this clearly shows that the fraction of IR luminosity due to old stellar populations can have a large impact on the accuracy of SFR indicators.

4.6 Conclusion

By fitting the UV-IR SEDs of SINGS galaxies with our grid of radiative transfer models, we studied dust properties and SFR indicators in nearby normal star-forming galaxies.

We find that the single component model, which describes a single stellar population intermixed with dust, is not sufficient to fit the global UV-IR SEDs of normal star-forming galaxies. The minimum model that can adequately describe these SEDs requires two components, representing the young and the old stellar populations in these galaxies. Such composite models are able to fit the UV-IR SEDs of 41 out of 44 galaxies in our sample with reduced chi-squares that are less than 2. In addition, the flux residual ensemble statistics show no significant systematic bias in any of the photometric bands in the SEDs.

We find that the dust type that best describes this sample of galaxies is the LMC 2 type dust, characterized by a 2175 Å bump and a far-UV rise that is intermediate in strength between that of MW and SMC type dust. This is in contrast with the results of Draine et al. (2007), who fit the IR-only SEDs of the same galaxies with the same dust models but with a simpler radiation field (scaled from the solar neighborhood radiation field) and without radiative transfer. In their model the MW type dust fits best, and this may be due to the softer-than-actual radiation field requiring higher-than-actual PAH abundances. This difference illustrates the importance of physically coupling the UV-optical SED with the IR SED to capture the full information available. Despite the difference in dust types, we find that our dust masses agree with the ones obtained by Draine et al. (2007) within a factor of 2.

The attenuation curve of the young component in our fitting exhibits the 2175 Å extinction feature that is present in the LMC 2 type dust. The strength of the bump is, however, very weak in the old component. This is likely due to radiative transfer effects, in which a geometry with less embedded stars gives a flatter attenuation curve. The attenuation curves of both component are steeper than the Calzetti (1997) starburst attenuation curve. While this is theoretically expected due to the higher optical depth in starburst galaxies, it serves as a clear example that applying a single attenuation curve to galaxies with different dust properties can lead to large errors.

We find that the young stellar populations dominate the FUV and MIPS24 luminosities in these normal star-forming galaxies. This is not surprising for FUV, given

that old stellar populations emit negligible amounts of FUV regardless of the existence of dust. Our results for MIPS24 provide a theoretical understanding on why MIPS24 is a good IR SFR indicator, supplementing the empirical evidence in the literature (Calzetti et al., 2007). On the other hand, almost all of the luminosity in the near-IR bands comes from the old stellar populations, consistent with the commonly accepted idea that the stellar mass-to-light ratio is relatively constant in the near-IR (Bell & de Jong, 2001), allowing these bands to be good tracers of the total stellar mass.

The fraction of luminosity from the young component is much more uncertain in the far-IR. While far-IR "cirrus emissions" is traditionally associated with cool dust heated by old stars, it is possible that the cool dust is heated by UV photons leaking out from the birth clouds of the young stellar populations (Calzetti, 2013). Indeed, in Chapter 2 we find from the IR luminosity ratios that the far-IR is dominated by young stellar populations, if we assume that the extinction optical depth for both stellar population is unity. Full UV-IR SED fitting with the DirtyGrid favors a low fraction of far-IR luminosity from the young component ($F_{\rm young}$), although for many galaxies our model also allows fits with a high $F_{\rm young}$. We find that the answer to whether far-IR dust heating is due to young or old populations not only varies between galaxies, but also depends on the modeling assumptions. Future extensions to the DirtyGrid with more complex geometries including diffuse dust at a distance from the young stellar population may provide new insight into the variations of $F_{\rm young}$.

Finally, we find that SFR values obtained from our SED fitting generally agree with values obtained from SFR indicators within a factor of 2, and the residuals are strongly correlated with the fraction of luminosity from the young component in the IR bands. This suggests that contamination of IR flux from dust heated by old stellar populations can severely affect the accuracy of SFR indicators in normal star forming galaxies. In galaxies with more intense star formation, SFR indicators also tend to underestimate SFR, likely because significant stochastic emission from dust grains occurs at shorter wavelengths than the IR bands used by the SFR indicators. Capturing the effect of stochastic emission on SFR indicators is challenging because of possible contamination from the stellar continuum. We demonstrate that full UV-IR SED fitting avoids these problems by decomposing the contributions of young and old stellar populations, resulting in more accurate SFR estimates than SFR indicators.

Chapter 5

Conclusion

5.1 Summary

The principle results of this thesis are (1) the production of a large grid of dust radiative transfer models that represents a step forward in more accurate modeling of dust in stellar populations and galaxies, and (2) the scientific findings that result from using the grid of models to fit a sample of nearby, normal star-forming galaxies, including the identification of LMC type dust, detection of the 2175 Å extinction feature, and that commonly used star formation indicators suffer from contamination from old stars. We have already published the findings in Chapter 2 in the Astrophysical Journal (Law et al., 2011). We intend to make the grid of models publicly available simultaneously with the publication of Chapters 3 and 4 in the Astrophysical Journal.

In § 5.2, we summarize the work in constructing our grid of models, the DIRTYGrid, and its significance. In § 5.3, we highlight the scientific results from applying these models to normal star forming galaxies.

5.2 The DIRTYGrid

The bulk of the luminosity emitted by normal star forming galaxies comes from starlight and emission of dust heated by starlight where the stars and dust are mixed in a complex geometry. Since dust absorbs, scatters, and re-emits stellar radiation, calculating the spectral energy distribution of a galaxy from assumed dust and stellar properties is a radiative transfer problem. The anisotropic nature of dust scattering prevents analytical solutions to the radiation transfer equation, and scattering approximations such as isotropic scattering can introduce significant errors (Baes & Dejonghe, 2001). This implies that accurate modeling of dust radiative transfer requires a numerical solution. Due to the high dimensionality, it is common to use Monte Carlo techniques to solve radiative transfer.

In the literature, various authors have modeled individual galaxies with radiative transfer. For example, De Looze et al. (2012) modeled the Sloan Digital Sky Survey g-band (green) image of the edge-on spiral galaxy NGC 4565 using the radiative transfer model SKIRT (Baes et al., 2011) and the physical dust model presented by Draine & Li (2007).

Fitting the full UV-IR spectral energy distributions of a sample of galaxies, however, requires a much larger parameter space than fitting a single galaxy. This requires a large amount of computational power that was previously impractical or traditionally not accessible to galaxy researchers. As a result, various authors have developed semi-analytic models that are much less computationally intensive. da Cunha et al. (2008) and Noll et al. (2009a) independently modeled the UV-IR spectral energy distributions of SINGS galaxies (the same sample of nearby, normal star forming galaxies we study), using sophisticated stellar population models but simplified recipes for dust attenuation and emission. For dust attenuation, the former authors assumed that the attenuation curves have a power-law shape, and the latter authors used the Calzetti (1997) attenuation law calibrated for starburst galaxies, linearly extrapolated, with variable slope adjustment added. For dust emission, the former authors adopted mid-IR emission templates measured in the Milky Way plus multiple components of dust at different equilibrium temperatures (including very high temperature components intended to emulate stochastic emissions), while the latter authors used the Dale & Helou (2002) IR templates measured from normal star forming galaxies. Both authors connected the UV-optical dust attenuation with the IR dust emission by energy conversation.

To our knowledge, our work is the first effort to create a grid of radiative transfer models spanning the full range of known dust and stellar properties *and* predicting the full UV to IR spectral energy distribution of galaxies. Compared to previous studies,

the primary strength of our work is the improved modeling of dust. With radiative transfer, we are able to properly model the anisotropic scattering of dust and detailed relationship between the dust absorption and emission spectra. Our attenuation curves emerge from combined effects of dust properties (size distribution, composition, extinction cross section, and scattering phase function) and dust-star geometry. Our dust emissions depend on dust properties and the self-consistent radiative field that results from the radiative transfer. We include the variation of dust properties from measurements of resolved star pairs in the MW, LMC and SMC, which represent the full range of known dust properties.

In order to make the computation feasible, we optimize both the run time of individual models as well as the sampling of the parameter space. Using the invariant scaling relation between luminosity and spatial scale, we eliminate the spatial size of the model as a variable. For the range of dust opacity in normal star forming galaxies, the original DIRTY model samples the scattered flux much better than the absorbed energy. In DIRTYv2, we use the "continuous absorption" technique to shift the computational balance, improving the sampling of the absorbed energy at the expense of the sampling of the scattered flux. In building up the grid of models, we employ a two-stage non-uniform sampling strategy to eliminate the computation of models in parts of the parameter space where changes in the output can be predicted by interpolation within the target error tolerance. We also identified redundant calculations across models and eliminated them with a "radiative transfer library" that

contains intermediate Monte Carlo weights.

The computation of the final grid of model was performed on various supercomputers and consumed approximately 5 million CPU hours. The spectral energy distributions will be released to the public and they open up a number of interesting scientific possibilities. While we have used the models to study the global spectral energy distributions of normal star forming galaxies, we (and other researchers) can also use them to study other galaxies such as starburst galaxies, dwarf galaxies, and high redshift galaxies. Alternatively, they can be used to study spatially resolved spectral energy distributions of galaxies. Use of these models represents a step forward in proper handling of dust physics in galaxies. Furthermore, these models provide a training set for empirical relations, for creating new calibrations, estimating the uncertainties, and identifying the source of error, under a wide range of dust and stellar properties.

5.3 Science conclusions

5.3.1 Galaxies as two components

We use the DirtyGrid to fit the spectral energy distributions of nearby, normal star-forming galaxies in the SINGS sample, to study dust properties and star formation rate indicators. We select the SINGS sample because (1) these galaxies span a wide range of galaxy properties such as morphological types and luminosities, and

they do not contain strong active galactic nuclei which are beyond the scope of this thesis, and (2) consistent aperture matched photometry, which is needed to assemble the UV-IR multi-wavelength spectral energy distributions, is available in the literature. Each model in the DirtyGrid represents a single dusty stellar population, and we find that single models cannot adequately fit these galaxies. The median reduced chi-square value is 4.5, and the residuals show systematic bias that is most severe in the far-UV and 24 μm mid-IR luminosities.

The model with the minimum additional complexity that produces good fit to these galaxies requires two components. We construct such "two-component" model as a linearly combination of a model with a young stellar population and a model with an old stellar population. We draw the dividing line between young and old at 100 Myr, because beyond this age stars generate a negligible amount of radiation in UV, where dust extinction is most efficient. We allow the stellar age, stellar mass, amount of dust, and geometry of both components to vary independently, but we impose the restriction that other parameters are fixed between the two components to avoid over-fitting.

In reality, a galaxy is a complex collection of different stellar populations mixed with dust, potentially with radiation leaking from one stellar population heating the dust in a different population (Popescu et al., 2005). The result that the two-component model is the simplest model that works is instructive to future studies. It can either mean that (1) a galaxy can be adequately and correctly characterized by

simply a young and an old component, or that (2) while the global spectral energy distribution fits well, it is an incorrect characterization and may result in biased estimated parameters. Distinguishing between the two cases will require additional research, such as fitting the spectral energy distributions of spatially resolved pieces of galaxies.

5.3.2 Dust type and dust mass

The properties of interstellar dust grains such as size distribution and chemical composition vary between different environments. A major source of information on dust grains is the extinction curve, which describes the wavelength dependence of dust extinction. The dust properties are most extensively studied in the Milky Way (MW), Large Magellanic Cloud (LMC), and Small Magellanic Cloud (SMC) where we can easily resolve individual stars. The full range of known dust properties in terms of extinction curve variations is covered by the MW, LMC 2 and SMC Bar type dust, which have a decreasing strength of the 2175 Å extinction feature and an increasing far-UV rise in that order. Determination of total dust mass is also important because it provides constraints on the process of star formation and the chemical evolution and environment conditions of the interstellar medium. It is common in the literature to fit the IR spectrum with one or more components of modified blackbody functions, each of which representing dust in equilibrium with the radiation field at a certain temperature, to determine the total dust mass.

Through radiative transfer modeling, Gordon et al. (1997) find that dust in starburst galaxies resembles SMC type dust. One of the most sophisticated studies on dust masses and dust type is the work of Draine et al. (2007), who used the solar neighborhood radiation field with a physical dust model to fit the IR spectral energy distribution of SINGS galaxies. The use of a physical dust model allows them to compute the IR spectral energy distribution from the physics of dust grains without assuming specific functional forms for the total dust emission. Fitting the full UV-IR spectral energy distribution with the DirtyGrid improve upon the work of Draine et al. (2007) by including radiative transfer effects and using a self-consistent radiation field that depends on the stellar populations and the dust-star geometry. A self-consistent radiation field is important because we expect the radiation field near young stars to be harder (carrying a higher fraction of energy in shorter wavelengths that are more efficiently absorbed by dust) than the one in the solar neighborhood.

We find that our recovered dust masses agree with the dust masses in Draine et al. (2007) within a factor of 2. The residuals, defined as the surplus in their dust masses compared to ours, correlate with the mass surface density of the old component. We find that the LMC 2 dust type, which has intermediate properties between MW and SMC (or starburst galaxies), best fits the normal star forming galaxies. This is different from the results in Draine et al. (2007) in which the MW type dust best fits the same sample of galaxies. This is likely because of the inclusion of harder radiation field in our models, which requires less polycyclic aromatic hydrocarbon

grains to produce the same mid-IR emissions, and the fact that LMC 2 type dust has a lower abundance for this type of grains. These differences show that using the UV-optical (in addition to IR) spectral energy distributions and radiative transfer can have a significant impact on the estimated dust masses and dust type.

5.3.3 Attenuation curve

An attenuation curve describes the wavelength dependence of dust attenuation in an unresolved mixture of stars and dust, and is more complicated than an extinction curve because of the inclusion of sources extinguished by differing amounts of dust and scattering into the beam towards us from different directions. Nonetheless, due to the limited resolution of observation instruments, only attenuation curves (but not extinction curves) are measurable in all but the nearest external galaxies. Attenuation curves are used in both semi-analytical modeling of galaxies and in removing the effect of dust from spectral energy distributions.

Calzetti et al. (1994) derived an average attenuation curve for starburst galaxies. This curve is shallower than the Milky Way extinction curve and lacks the 2175 Å bump. Wild et al. (2011) empirically determined the attenuation curves for a large sample of star-forming galaxies. While the former authors have spectroscopic data so that they can resolve the attenuation curve in a range of UV wavelengths, the latter authors only have broadband spectral energy distribution that contains two data points in the UV, and as a result their attenuation curves only have two points

in the UV. It is difficult to decisively detect a curve feature with just two points, but they found a slope change in the UV that is consistent with a dust bump at 2175 Å.

With radiative transfer modeling, we are able to determine the resolved UV-optical attenuation curves from spectral energy distribution fitting. We find a weak 2175 Å bump in the average attenuation curve of our sample of normal star-forming galaxies and the feature is more prominent in the young component. The attenuation curve is steeper than the Calzetti starburst attenuation curve, and this is likely because of the radiative transfer effects at a lower optical depth in the normal star forming galaxies (compared to starburst galaxies). As such, when modeling or correcting for the effect of dust in galaxies with an attenuation curve, it is important to use one that is representative of the sample of galaxies being studied.

5.3.4 Fraction of luminosity from the young component

The young and the old components contribute differently to different parts of the spectral energy distribution. We find that in the far-UV, the direct starlight from young stellar populations dominates. In the optical and near-IR, the emission is primarily from the starlight from old stellar populations. At ~ 24 μm in the mid-IR, the young component once again makes the biggest contribution to the luminosity, this time with dust emission instead of starlight. In the two transitions (near-UV

and mid-IR ~ 8 μm) between the three regimes, there are variations in the relative contributions of young and old components in our sample.

These agree well with the usual understanding in normal star forming galaxies. However, whether the emissions at $\gtrsim 70$ μm are powered by dust heated by young or old stars is more uncertain. Emissions from ~ 100 μm correspond to cool dust emissions at about 30 K, and results in the literature regarding the relative contributions vary. By analyzing the spatial distribution of the ratios of far-IR surface brightness ratios in spiral galaxy M81, Bendo et al. (2010b) found that the 160–500 μm emission traces dust heated by old stellar populations, whereas 70 μm emission includes dust heated by young stellar populations and the active galactic nucleus. By comparing the IR luminosities of observations with radiative transfer models, Law et al. (2011) (also included in Chapter 2) found that young stellar populations dominate dust heating in star-forming galaxies, and old stellar populations generally contribute less than 20% of the far-IR luminosity at $\lambda \lesssim 160$ μm. More recently, Bendo et al. (2015) found that the transition wavelength between young stars dominated heating and old stars dominated heating varies between 160 μm and 500 μm in their sample of nearby face-on spiral galaxies.

From the two-component spectral energy distribution fitting of the SINGS galaxies, we find a large uncertainty in the average fraction of luminosity from the young component, partly due to variations between galaxies in our sample, and partly because the data of some galaxies allow different decompositions of the spectral energy

distributions that results in vastly different results in the far-IR. This supports the view that the question to the origin of dust heating that causes far-IR emissions may not have a single answer, but rather depends on the detailed evolution of each galaxy.

5.3.5 Star formation rate indicators

Star formation is an important component of galaxy formation and evolution. The rate at which star formation occurs can be estimated from broadband or emission line luminosities that trace emissions from young stars. Literature star formation rate indicators are typically based on far-UV, near-UV, Hα, or total IR (Kennicutt & Evans, 2012). Far-UV luminosity directly traces young stars ($\lesssim$ 100 Myr) because old stars generate a negligible amount of far-UV radiation. However, far-UV is significantly attenuation by dust, and the variations of the amount of dust present in different objects implies that star formation rate based on far-UV alone is subject to large uncertainties. Ionizing radiation from young stars ($\lesssim$ 10 Myr) powers hydrogen recombination emission lines such as Hα, which is in the optical wavelength range and therefore also affected by dust. Since dust re-emits the absorbed energy in the IR, it is common to add an IR term to star formation rate indicators to correct for the effects of dust.

By construction, our results with the two-component model give us the star formation rate in the last 100 Myr, similar to the age range measured by most literature star formation rate indicators. We find that our star formation rates agree with

literature star formation rate indicators within a factor of 2. The difference is correlated with the fraction of luminosity of the young component in the IR bands. This demonstrates that in normal star forming galaxies, IR luminosities from old stellar populations can cause variations in the ratio between luminosities and true star formation rate. Since the ratios in the literature star formation rate indicators are constant, these variations are a source of error. We also find that literature star formation rate indicators tend to underestimate the star formation rate at the high end. This is likely because at a high star formation rate, stochastic emission from small dust grain is significant but the wavelengths of these emissions are shorter than the IR bands they used. Including shorter wavelength IR bands in star formation rate indicators would be problematic because of contamination from direct starlight of old stars. The modeling of full UV-IR spectral energy distributions (instead of using just one or two bands) by decomposing the spectral energy distributions into a young and an old component allows us to avoid these problems by removing the contamination from the old component on a galaxy-by-galaxy basis.

5.4 Future directions

We build the DirtyGrid with a focus on dust properties. To make the computation practical, we have optimized the grid with a lower resolution in quantities that are of less interest to us. With additional computational resources, there are multiple

areas in which we can improve the resolution of the grid. For example, it is common in the literature to model the star formation history of a galaxy with an exponentially decaying function in time. The two-component model we used essentially corresponds to having a large burst of star formation in the distant past (on the order of Gyr) plus a continuous stream of star formation in the last 100 Myr. While both of these are simplified models, it would be interesting to see how differences in assumed star formation history can affect the estimated dust properties. It will also be useful to allow more variations in the global geometries. While the Shell, Dusty, and Cloudy geometries capture a wide range of dust attenuation efficiencies, none of these explicitly provide a low density, "diffuse dust" component at a large distance from the stellar populations. Adding such component may help investigate the extent to which UV photons leaking from the birth cloud of young stars can heat diffuse dust and therefore provide significant emission in far-IR.

The next step to improve our understanding on dust properties in galaxies is to study the spatially resolved spectral energy distributions. This thesis has exclusively used globally integrated spectral energy distributions, which mix the contributions from dust and stellar populations in different parts of galaxies. It is known that, for example, the bulge of spiral galaxies are dominated by old stellar populations with very little interstellar medium, while the disks are where on-going star formation activity mainly occurs. Fitting the spatially resolved spectral energy distributions will allow us to better separate the different populations and in theory may provide

more accurate results. It will also allow us to study the spatial variations of dust properties, and to validate (or identify the limitations in) the use of a two-component models to fit globally integrated spectral energy distributions.

Bibliography

Allamandola, L. J., Tielens, A. G. G. M., & Barker, J. R. 1985, ApJ, 290, L25

Andrae, R., Schulze-Hartung, T., & Melchior, P. 2010, ArXiv e-prints, arXiv:1012.3754

Armus, L., Mazzarella, J. M., Evans, A. S., et al. 2009, PASP, 121, 559

Baes, M., & Dejonghe, H. 2001, MNRAS, 326, 733

Baes, M., Verstappen, J., De Looze, I., et al. 2011, ApJS, 196, 22

Baes, M., Davies, J. I., Dejonghe, H., et al. 2003, MNRAS, 343, 1081

Bell, E. F. 2002, ApJ, 577, 150

Bell, E. F., & de Jong, R. S. 2001, ApJ, 550, 212

Bendo, G. J., Wilson, C. D., Pohlen, M., et al. 2010a, A&A, 518, L65+

—. 2010b, A&A, 518, L65

Bendo, G. J., Baes, M., Bianchi, S., et al. 2015, MNRAS, 448, 135

BIBLIOGRAPHY

Bertelli, G., Bressan, A., Chiosi, C., Fagotto, F., & Nasi, E. 1994, A&AS, 106, 275

Bigiel, F., Leroy, A., Walter, F., et al. 2008, AJ, 136, 2846

Bless, R. C., & Savage, B. D. 1970, in IAU Symposium, Vol. 36, Ultraviolet Stellar Spectra and Related Ground-Based Observations, ed. R. Muller, L. Houziaux, & H. E. Butler, 28

Boselli, A., Ciesla, L., Buat, V., et al. 2010, A&A, 518, L61+

Bruzual, G., & Charlot, S. 2003, MNRAS, 344, 1000

Burkert, A., & Alves, J. 2009, ApJ, 695, 1308

Calzetti, D. 1997, AJ, 113, 162

—. 2001, PASP, 113, 1449

—. 2013, Star Formation Rate Indicators, ed. J. Falcón-Barroso & J. H. Knapen, 419

Calzetti, D., Armus, L., Bohlin, R. C., et al. 2000, ApJ, 533, 682

Calzetti, D., Kinney, A. L., & Storchi-Bergmann, T. 1994, ApJ, 429, 582

Calzetti, D., Kennicutt, Jr., R. C., Bianchi, L., et al. 2005, ApJ, 633, 871

Calzetti, D., Kennicutt, R. C., Engelbracht, C. W., et al. 2007, ApJ, 666, 870

Calzetti, D., Wu, S., Hong, S., et al. 2010, ApJ, 714, 1256

Camps, P., Misselt, K., Bianchi, S., et al. 2015, ArXiv e-prints, arXiv:1506.05304

BIBLIOGRAPHY

Cardelli, J. A., Clayton, G. C., & Mathis, J. S. 1989, ApJ, 345, 245

Charlot, S., & Bruzual, A. G. 1991, ApJ, 367, 126

Charlot, S., & Fall, S. M. 2000, ApJ, 539, 718

Conroy, C., Gunn, J. E., & White, M. 2009, ApJ, 699, 486

Conti, A., Connolly, A. J., Hopkins, A. M., et al. 2003, AJ, 126, 2330

da Cunha, E., Charlot, S., & Elbaz, D. 2008, MNRAS, 388, 1595

Dale, D. A., & Helou, G. 2002, ApJ, 576, 159

Dale, D. A., Smith, J. D. T., Armus, L., et al. 2006, ApJ, 646, 161

Dale, D. A., Gil de Paz, A., Gordon, K. D., et al. 2007, ApJ, 655, 863

Dale, D. A., Cohen, S. A., Johnson, L. C., et al. 2009, ApJ, 703, 517

Dale, D. A., Aniano, G., Engelbracht, C. W., et al. 2012, ApJ, 745, 95

De Looze, I., Baes, M., Bendo, G. J., et al. 2012, MNRAS, 427, 2797

De Looze, I., Fritz, J., Baes, M., et al. 2014, A&A, 571, A69

Desert, F.-X., Boulanger, F., & Puget, J. L. 1990, A&A, 237, 215

Disney, M., Davies, J., & Phillipps, S. 1989, MNRAS, 239, 939

Draine, B. T. 2003, ARA&A, 41, 241

BIBLIOGRAPHY

Draine, B. T. 2009, in EAS Publications Series, Vol. 35, EAS Publications Series, ed. F. Boulanger, C. Joblin, A. Jones, & S. Madden, 245–268

—. 2011, Physics of the Interstellar and Intergalactic Medium

Draine, B. T., & Li, A. 2001, ApJ, 551, 807

—. 2007, ApJ, 657, 810

Draine, B. T., Dale, D. A., Bendo, G., et al. 2007, ApJ, 663, 866

Duley, W. W. 1973, Ap&SS, 23, 43

Duley, W. W., & Seahra, S. 1998, ApJ, 507, 874

Duval, F., Schaerer, D., Östlin, G., & Laursen, P. 2014, A&A, 562, A52

Elíasdóttir, Á., Fynbo, J. P. U., Hjorth, J., et al. 2009, ApJ, 697, 1725

Engelbracht, C. W., Gordon, K. D., Rieke, G. H., et al. 2005, ApJ, 628, L29

Engelbracht, C. W., Rieke, G. H., Gordon, K. D., et al. 2008, ApJ, 678, 804

Engelbracht, C. W., Blaylock, M., Su, K. Y. L., et al. 2007, PASP, 119, 994

Erb, D. K., Shapley, A. E., Pettini, M., et al. 2006, ApJ, 644, 813

Fioc, M., & Rocca-Volmerange, B. 1997, A&A, 326, 950

—. 1999, ArXiv Astrophysics e-prints, astro-ph/9912179

BIBLIOGRAPHY

Fitzpatrick, E. L. 1999, PASP, 111, 63

Gordon, K. D., Calzetti, D., & Witt, A. N. 1997, ApJ, 487, 625

Gordon, K. D., & Clayton, G. C. 1998, ApJ, 500, 816

Gordon, K. D., Clayton, G. C., Misselt, K. A., Landolt, A. U., & Wolff, M. J. 2003, ApJ, 594, 279

Gordon, K. D., Clayton, G. C., Witt, A. N., & Misselt, K. A. 2000, ApJ, 533, 236

Gordon, K. D., Engelbracht, C. W., Rieke, G. H., et al. 2008, ApJ, 682, 336

Gordon, K. D., Hanson, M. M., Clayton, G. C., Rieke, G. H., & Misselt, K. A. 1999, ApJ, 519, 165

Gordon, K. D., Misselt, K. A., Witt, A. N., & Clayton, G. C. 2001, ApJ, 551, 269

Gordon, K. D., Engelbracht, C. W., Fadda, D., et al. 2007, PASP, 119, 1019

Groenewegen, M. A. T., & de Jong, T. 1993, A&A, 267, 410

Guhathakurta, P., & Draine, B. T. 1989, ApJ, 345, 230

Gunn, J. E., Siegmund, W. A., Mannery, E. J., et al. 2006, AJ, 131, 2332

Hao, C.-N., Kennicutt, R. C., Johnson, B. D., et al. 2011, ApJ, 741, 124

BIBLIOGRAPHY

Helou, G. 1994, in Astronomical Society of the Pacific Conference Series, Vol. 58, The First Symposium on the Infrared Cirrus and Diffuse Interstellar Clouds, ed. R. M. Cutri & W. B. Latter, 223–+

Henyey, L. G., & Greenstein, J. L. 1941, ApJ, 93, 70

Holwerda, B. W., Keel, W. C., & Bolton, A. 2007, AJ, 134, 2385

Hora, J. L., Carey, S., Surace, J., et al. 2008, PASP, 120, 1233

Ivezic, Z., & Elitzur, M. 1997, MNRAS, 287, 799

Kennicutt, R. C., & Evans, N. J. 2012, ARA&A, 50, 531

Kennicutt, R. C., Hao, C., Calzetti, D., et al. 2009, ApJ, 703, 1672

Kennicutt, Jr., R. C. 1998, ARA&A, 36, 189

Kennicutt, Jr., R. C., Armus, L., Bendo, G., et al. 2003, PASP, 115, 928

Kong, X., Charlot, S., Brinchmann, J., & Fall, S. M. 2004, MNRAS, 349, 769

Kroupa, P. 2001, MNRAS, 322, 231

Law, K.-H., Gordon, K. D., & Misselt, K. A. 2011, ApJ, 738, 124

Leger, A., & Puget, J. L. 1984, A&A, 137, L5

Leitherer, C., Schaerer, D., Goldader, J. D., et al. 1999, ApJS, 123, 3

Leroy, A. K., Walter, F., Brinks, E., et al. 2008a, AJ, 136, 2782

—. 2008b, AJ, 136, 2782

Li, A., & Draine, B. T. 2001, ApJ, 554, 778

Lis, D. C., Serabyn, E., Keene, J., et al. 1998, ApJ, 509, 299

Lonsdale Persson, C. J., & Helou, G. 1987, ApJ, 314, 513

Maraston, C. 2005, MNRAS, 362, 799

Marble, A. R., Engelbracht, C. W., van Zee, L., et al. 2010, ApJ, 715, 506

Martin, D. C., Fanson, J., Schiminovich, D., et al. 2005, ApJ, 619, L1

Mathis, J. S., Rumpl, W., & Nordsieck, K. H. 1977, ApJ, 217, 425

McCarthy, D. W., Howell, R., & Low, F. J. 1980a, ApJ, 235, L27

McCarthy, J. F., Forrest, W. J., Briotta, Jr., D. A., & Houck, J. R. 1980b, ApJ, 242, 965

Meaburn, J. 1980, MNRAS, 192, 365

Meurer, G. R., Heckman, T. M., & Calzetti, D. 1999, ApJ, 521, 64

Meurer, G. R., Heckman, T. M., Leitherer, C., et al. 1995, AJ, 110, 2665

Misselt, K. A., Clayton, G. C., & Gordon, K. D. 1999, ApJ, 515, 128

Misselt, K. A., Gordon, K. D., Clayton, G. C., & Wolff, M. J. 2001, ApJ, 551, 277

BIBLIOGRAPHY

Moustakas, J., Kennicutt, Jr., R. C., Tremonti, C. A., et al. 2010, ApJS, 190, 233

Muñoz-Mateos, J. C., Boissier, S., Gil de Paz, A., et al. 2011, ApJ, 731, 10

Muñoz-Mateos, J. C., Gil de Paz, A., Zamorano, J., et al. 2009a, ApJ, 703, 1569

Muñoz-Mateos, J. C., Gil de Paz, A., Boissier, S., et al. 2009b, ApJ, 701, 1965

Noll, S., Burgarella, D., Giovannoli, E., et al. 2009a, A&A, 507, 1793

Noll, S., Pierini, D., Pannella, M., & Savaglio, S. 2007, A&A, 472, 455

Noll, S., Pierini, D., Cimatti, A., et al. 2009b, A&A, 499, 69

Pflamm-Altenburg, J., & Kroupa, P. 2009, ApJ, 706, 516

Pilbratt, G. L., Riedinger, J. R., Passvogel, T., et al. 2010, A&A, 518, L1

Popescu, C. C., Misiriotis, A., Kylafis, N. D., Tuffs, R. J., & Fischera, J. 2000, A&A, 362, 138

Popescu, C. C., Tuffs, R. J., Madore, B. F., et al. 2005, ApJ, 619, L75

Salim, S., Rich, R. M., Charlot, S., et al. 2007, ApJS, 173, 267

Salpeter, E. E. 1955, ApJ, 121, 161

Sauvage, M., & Thuan, T. X. 1992, ApJ, 396, L69

Schlegel, D. J., Finkbeiner, D. P., & Davis, M. 1998, ApJ, 500, 525

BIBLIOGRAPHY

Searle, L., Sargent, W. L. W., & Bagnuolo, W. G. 1973, ApJ, 179, 427

Sellgren, K. 1984, ApJ, 277, 623

Silva, L., Granato, G. L., Bressan, A., & Danese, L. 1998, ApJ, 509, 103

Skrutskie, M. F., Cutri, R. M., Stiening, R., et al. 2006, AJ, 131, 1163

Stansberry, J. A., Gordon, K. D., Bhattacharya, B., et al. 2007, PASP, 119, 1038

Stecher, T. P., & Donn, B. 1965, ApJ, 142, 1681

Steinacker, J., Baes, M., & Gordon, K. D. 2013, ARA&A, 51, 63

Tinsley, B. M. 1968, ApJ, 151, 547

Trumpler, R. J. 1930, PASP, 42, 214

Vijh, U. P., Witt, A. N., & Gordon, K. D. 2003, ApJ, 587, 533

Walcher, J., Groves, B., Budavári, T., & Dale, D. 2011, Ap&SS, 331, 1

Weingartner, J. C., & Draine, B. T. 2001, ApJ, 548, 296

Werner, M. W., Roellig, T. L., Low, F. J., et al. 2004, ApJS, 154, 1

Wild, V., Charlot, S., Brinchmann, J., et al. 2011, MNRAS, 417, 1760

Willner, S. P. 1976, ApJ, 206, 728

Witt, A. N., & Gordon, K. D. 1996, ApJ, 463, 681

—. 2000, ApJ, 528, 799

Witt, A. N., Thronson, Jr., H. A., & Capuano, Jr., J. M. 1992a, ApJ, 393, 611

—. 1992b, ApJ, 393, 611

Xu, C., & Helou, G. 1996, ApJ, 456, 163

Zoccali, M., Renzini, A., Ortolani, S., et al. 2003, A&A, 399, 931

Vita

Ka-Hei Law received the B.Sc. degree in Physics from the Chinese University of Hong Kong in 2007, and enrolled in the Physics and Astronomy department Ph.D. program at Johns Hopkins University in 2007.